A Report on

AEROELASTIC ANALYSIS OF BRIDGE GIRDER SECTION USING COMPUTER MODELING

for

Mack Blackwell Transportation Center

By

Dr. R. Panneer Selvam and Suresh Govindaswamy

May 2001
University of Arkansas

ABSTRACT

This report describes the numerical simulation of wind flow around bridges using the Finite Element Method (FEM) and the principles of Computational Fluid Dynamics (CFD) and Computational Structural Dynamics (CSD). Since, the suspension bridges are prone to the aerodynamic instabilities caused by wind this becomes a prime criterion to be checked during the design. If the wind velocity exceeds the critical velocity for flutter that the bridge can withstand, then the bridge fails due to the phenomenon of flutter. Tacoma's narrows bridge failure in Washington, USA is a classical example of this failure. Larsen and Walther (1997) used the Discrete Vortex Method (DVM) similar to the wind tunnel procedures. In this work, the computations are carried out for both the fixed and the moving bridge conditions. A Large Eddy Simulation (LES) turbulence model is used and the rigid body grid movement technique is adopted. The critical velocity for flutter is calculated directly using the free oscillation procedure similar to the approaches reported by Selvam et. al (1998 and 2000). The influence of grid on critical velocity is also studied. The computed critical velocity for flutter is in good agreement with the wind tunnel measurements. The conditions of flutter and no flutter are demonstrated clearly using the response of the bridge in time.

TABLE OF CONTENTS

CHAPTER 1

INTRODUCTION

1.1 General Overview

The design of bridges, in particular long spanned ones, is challenging in the sense that there are many complicated issues to be considered. Amidst the loads to be considered, like dead load, live load, wind load, and earthquake load, the wind load becomes the prime concern for the design of the bridges. Traditionally, analysis of a bridge structure and the wind effects are studied using wind tunnel experiments. This usually takes 6-8 weeks and also it is very costly. With the explosive growth in the electronic and computer industry there has been a tremendous increase in the computing power and speed. Therefore, now the shift is towards computer modeling of the wind induced effects on a bridge structure by using the principles of Computational Structural Dynamics (CSD) and Computational Fluid Dynamics (CFD). This reduces cost and time considerably when compared to the traditional approach of wind tunnel experiments for design and analysis of bridges.

1.2 Significance of this research

The Tacoma Narrows Bridge at Washington, opened in 1940, is a well-known classical example of a bridge failure due to wind. This bridge had abnormally excessive deflections both during construction and service. A wind velocity as low as 42 mph ripped apart the bridge and tore it, buckling the stiffening girders at the mid-span (Bowers, 1940). This failure was due to the phenomenon of flutter. Flutter occurs if the

velocity of wind is higher than the critical velocity for a given bridge. This failure brought awareness to the designers around the world that wind can cause aerodynamic instability of bridges resulting in failure. Thus it becomes necessary and important to conduct sufficient aerodynamic studies of the bridge before construction so that the stability of the bridge against wind can be ensured.

1.3 Organization of the report

This report is organized in the form of chapters. The introduction chapter states the objective and necessity of the research problem and the current overview adopted by researchers across the globe in the Wind Engineering field. To understand the wind phenomenon and its effect of wind on structures, a clear knowledge of the wind forces and their behavior needs to be studied first. These issues are discussed in the second chapter. There is an abundant research being done on the aeroelastic studies in the field of computational wind engineering. The third chapter deals with a survey of the literature and current work being done on the study of bridge aerodynamics.

Once the literature study and review is through, the numerical modeling becomes the focus. The fourth chapter talks about the issues involved in the numerical modeling and the computational techniques used in solving the Navier-Stokes equations. The numerical modeling techniques like finite element, finite difference or finite volume methods are grid-based systems wherein the flow is solved computationally upon a discrete system of grid points. The issues involved in the generation of an efficient grid for a given problem is detailed in chapter five. The outcome of the research and the

results are presented in chapter six. Conclusions, comments and suggestions for improvement and future work are dealt with in the last chapter.

1.4 Objective

The objective of this report is to develop a computer model based on the principles of computational fluid dynamics and computational structural mechanics and the finite element method to study the aeroelastic stability of bridges. The Great Belt East Bridge (GBEB) is chosen because there has been a lot of wind tunnel experimental data available for validation and comparison of the computer model. The objective is achieved systematically through the following steps.

1. Build a computer model to simulate the bridge under fixed and moving conditions.
2. Develop a Fluid-Structure Interaction (FSI) model for the critical velocity computations.
3. Use the developed Computer model to study the effect of grid size and grid distribution and hence optimize.
4. Compare and validate the results against the wind tunnel experiments and models being built upon by other researchers across the world for the same GBEB section.

The computer simulation serves as a design tool to provide important design information faster than that possible by wind tunnel tests and thereby making it easier for many design trials in a shorter time. It also helps in the study of the influence of overall structural layout modifications and changes in cross-sectional shapes more easily. Thus a

faster design cycle reduces the design risk to a minimum and makes actual bridge designs more cost-efficient.

CHAPTER –2

WIND EFFECT ON STRUCTURES

2.1 Introduction

In the design of long span suspension bridges, notably suspended bridges, the wind action is of primary concern. With the failure of the Tacoma Narrows suspension bridge in 1940 in Washington, a deep general realization of the potential aeroelastic nature of the wind phenomena was firmly established the world over. Therefore to understand the response of long span suspension bridges under wind excitation, the basic wind phenomena needs to be clearly understood. Hence this chapter focuses on and reviews a number of topics connected with the effect of the wind on long-span suspension bridges.

The aerodynamic effect of wind on bridges are primarily vortex shedding, galloping, torsional-divergence, flutter and buffeting. They are discussed below.

2.2 Criteria for the design of a bridge

The criteria for the design of long spanned suspension bridges are concerned with the static and dynamic responses of the bridge under wind loading. A basic knowledge of the wind forces that are required to understand the issues involved in the design is explained in the following section.

The design of long span suspension bridges is often governed by aeroelastic instability. Aerodynamic design involves calculation of the critical velocity for the onset

of flutter. It is to be ensured that the wind velocity does not exceed the predicted critical velocity to avoid failure due to flutter.

Arrol and Chatterjee (1981) report that frequencies other than the fundamental one should be considered in design. They mention that the designers should remember that the position of maximum stress would not always be at mid-span, or a support, and the stress value will depend upon the mode shape. In a simply supported span the second mode maximum stress is at the quarter points and will have a value four times that of the fundamental mode maximum stress, occurring at mid span.

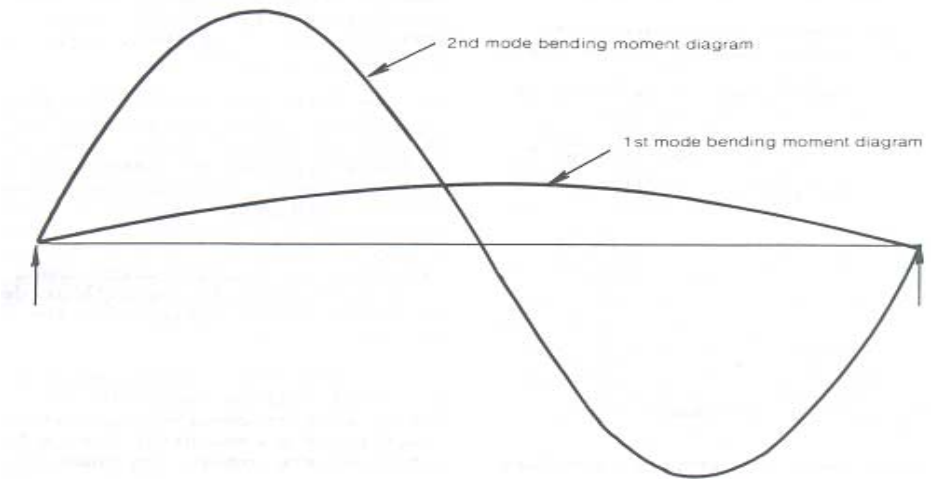

Figure 2.1 Relative bending moment diagrams due to 1st and 2nd modes of vibration.

(Picture from Arrol and Chatterjee, 1981)

There are static and dynamic concerns to be considered for a safer design of bridges as discussed by Simiu and Scanlan (1986) and Larsen (1992). They are described below.

2.2.1 Static behavior

Here the considerations are overturning, excessive lateral deflection, divergence, and lateral buckling (Selvam et. al., 1998). Usually the static phenomena are not critical for the design of bridges. The issues related to static behavior can be checked by the aerodynamic force components like drag force, lift force and pitching moment. The static issues are taken care of by the plot of the coefficients of drag, lift and moment against the angle of incidence of wind. This is explained in chapter four.

2.2.2 Dynamic behavior

From Newton's second law, the motion of mass is described by the differential equation

$$m\ddot{x} + c\dot{x} + kx = F(t)$$

Where $F(t)$ is the time dependent load acting on the mass, k is the stiffness coefficient and c is the coefficient of damping. This equation can be rewritten in the form

$$\ddot{x} + 2\zeta\omega\dot{x} + \omega^2 x = \frac{F(t)}{m}$$

Where $\omega = \sqrt{\frac{k}{m}}$ and $\zeta = \frac{c}{2m\omega}$. Here ω is the natural circular frequency and $2m\omega$ is the critical damping coefficient. Three cases arise based on ζ being less than, equal to, or greater than unity resulting in under-damped, critically damped and over-damped response respectively.

Dynamic behavior includes the responses due to vortex shedding excitation, self-excited oscillations and buffeting by wind turbulence (Selvam 1998). Sachs (1978) states that suspension bridges could oscillate in two natural modes, vertical and torsional. In the

vertical mode, all joints at any cross-section move the same distance in the vertical plane, while in the torsional mode every cross-section rotates about a longitudinal axis parallel to the roadway.

Unlike the static behavior, the dynamic behavior is critical and important to be considered during design.

2.3 Aerodynamic Instability

Aeroelasticity is the discipline concerned with the study of phenomena wherein the aerodynamic forces and structural motions interact significantly. When a structure is subjected to wind flow, it may vibrate or suddenly deflect in the airflow. This structural motion results in a change in the flow pattern around the structure. If the modification of wind pattern around the structure by aerodynamic forces is such that it increases rather than decreasing the vibration, thereby giving rise to succeeding deflections of oscillatory and/or divergent character, aeroelastic instability is said to occur (Simiu and Scanlan, 1986). The aeroelastic phenomena that are considered in wind engineering are vortex shedding, torsional divergence, galloping, flutter and buffeting.

2.4 Vortex Shedding

Simiu and Scanlan (1986) states that when a body is subjected to wind flow, the separation of flow occurs around the body. This produces force on the body, a pressure force on the windward side and a suction force on the leeward side. The pressure and suction forces result in the formation of vortices in the wake region causing structural deflections on the body. The shedding of vorticity balances the change of fluid

momentum along the entire body surface (Larsen and Walther, 1997). The shed vortices are convected downwind by local mean wind speed and viscous diffusion but will also interact to form large-scale coherent structures. The frequency in which the vortices are shed dictates the structural response. The structural member acts as if rigidly fixed, when the frequency of vortex shedding (also called wake frequency) is not close to the natural frequency of the member. On the other hand, when the vortex-induced and the natural-frequencies coincide, the resulting condition is called *lock-in*. During lock-in condition, the structural member oscillates with increased amplitude but rarely exceeding half of the across wind dimension of the body (Simiu and Scanlan, 1986). The lock-in condition is illustrated in Figure 2.2.

In the Figure 2.2, we see that the wake frequency remains locked to that of natural frequency for a range of wind velocities. As the velocity further increases, the wake frequency will again break away from the natural frequency. The extent of the shedding depends on the Reynolds number, which is defined as

$$R_E = \frac{\rho V D}{\mu}$$

Where

R_E ⟶ Reynolds number

ρ ⟶ density of the fluid

V ⟶ velocity of the fluid relative to the cylinder

D ⟶ diameter

μ ⟶ dynamic viscosity of the fluid

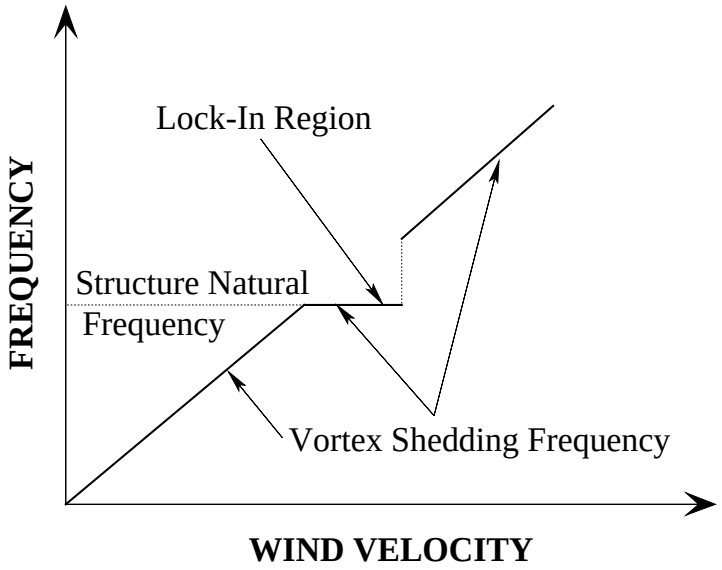

Figure 2.2 Qualitative trend of vortex shedding frequency with wind velocity during lock-in (Simiu and Scanlan, 1986)

Simiu and Scanlan (1986) explain and give an insight into the understanding of the nature and extent of the vortex shedding phenomenon for different ranges of Reynolds number for two different cross-sections, a plate and a cylinder as shown in Fig 2.3 and 2.4. They also report that, the vortex-shedding phenomena is describable in terms of a non-dimensional number S, which is defined as

$$S=\frac{N_S D}{U}$$

where

- S ⟶ Strouhal number
- N_s ⟶ frequency of full cycles of vortex shedding
- D ⟶ characteristic dimension of the body projected on a plane normal to the mean flow velocity
- U ⟶ velocity of the oncoming flow

The number S takes on different characteristic constant values depending upon the cross-sectional shape of the prism being enveloped by the flow.

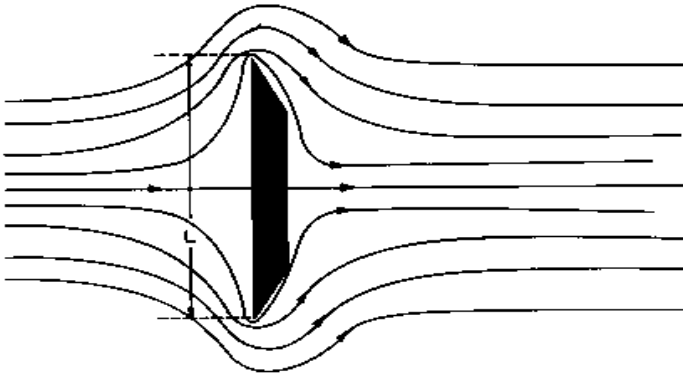

Figure2.3 (a) **R_e =0.3**

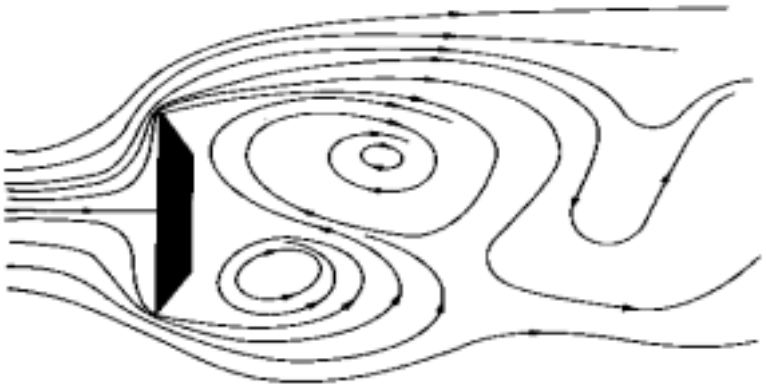

Figure 2.3 (b) **R_e = 10**

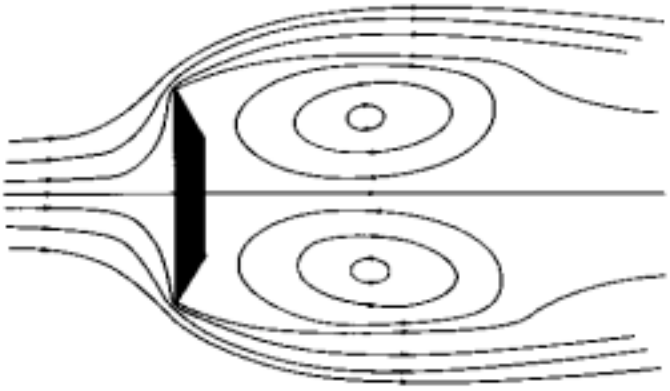

Figure 2.3 (c) **R_e = 250**

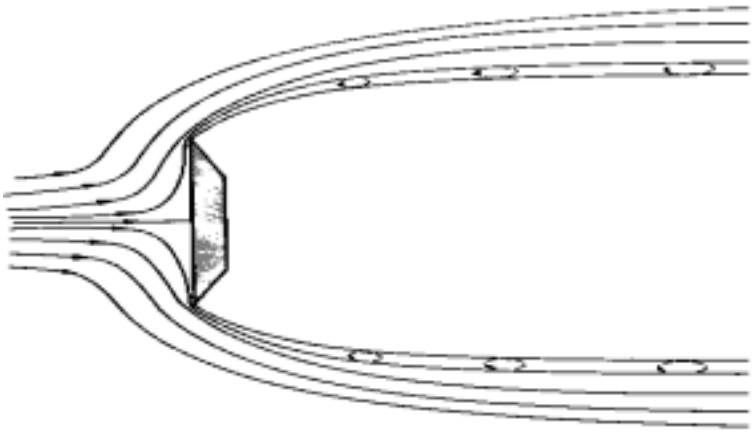

Figure 2.3 (d) **R_e >=1000**

Figure 2.3 (a)-(d) Flow past a sharp edged plate showing the vortex shedding

(Pictures taken from Simiu and Scanlan, 1986)

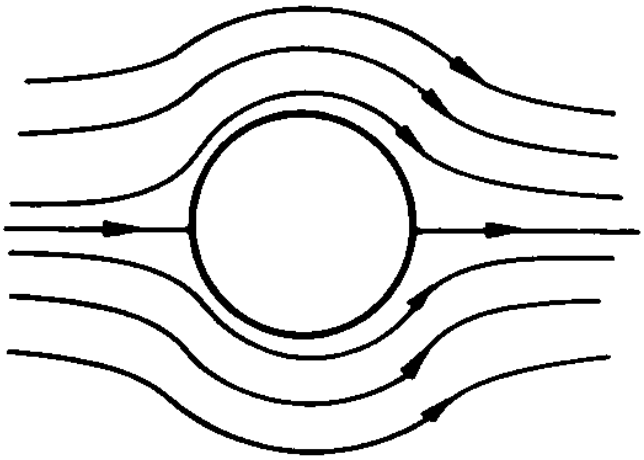

Figure 2.4 (a) $\mathbf{R_e \cong 1}$

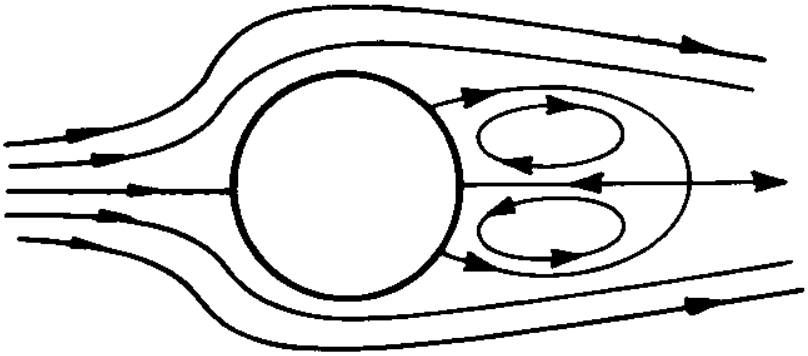

Figure 2.4 (b) $\mathbf{R_e \cong 20}$

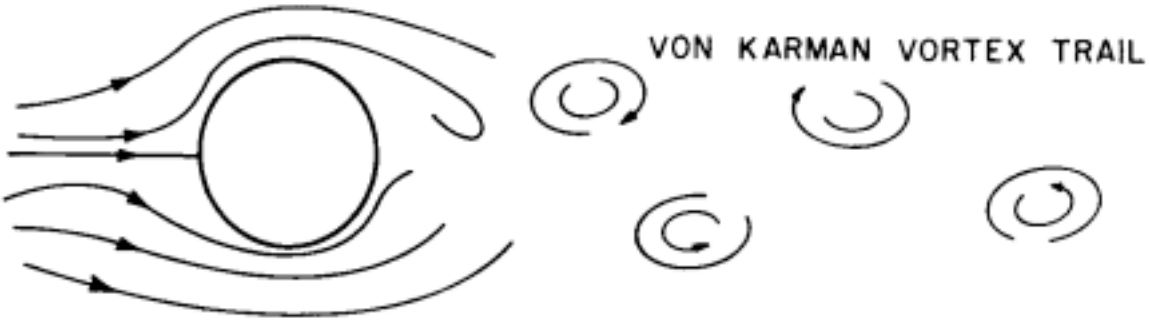

Figure 2.4 (c) $\mathbf{30 \leq R_e \leq 5000}$

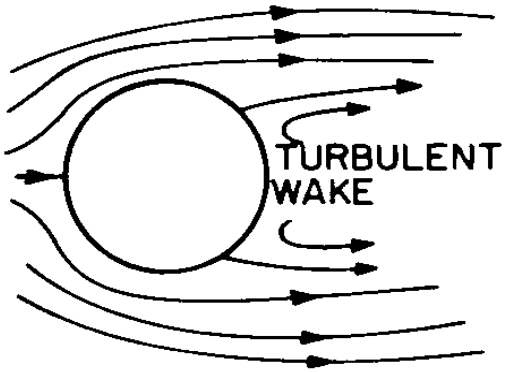

Figure 2.4 (d) **$5000 \leq R_e \leq 20000$**

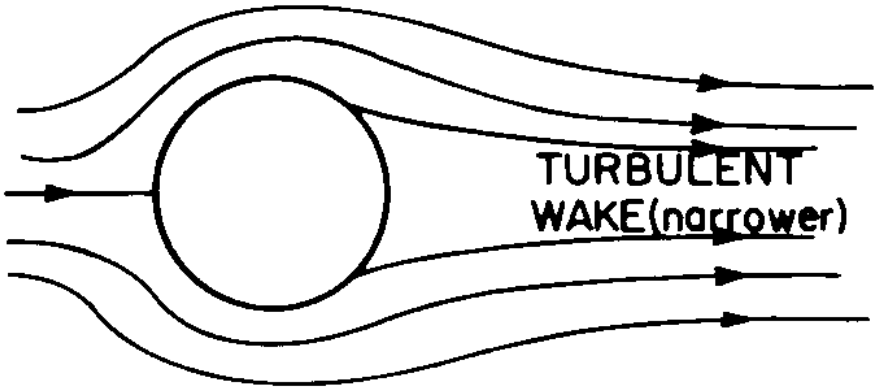

Fig 2.4 (e) **$R_e \geq 200000$**

Figure 2.4 (a)-(e) Flow past a Circular cylinder

(Pictures taken from Simiu and Scanlan, 1986)

From the figures, as illustrated by Simiu and Scanlan (1986), it is seen that for a very low Reynolds number, the flow remains the same, just circumventing the obstruction on its way. For higher Reynolds numbers, the flow starts to separate around the edges of the obstruction and vortices are generated in the immediate wake of the obstruction. Thereafter further increase in the Reynolds number causes the creation of cyclically

alternating vortices and they are carried over with the flow downstream. From there on, the inertial effects become dominant over the viscous effects and turbulence sets in, resulting in shear of the flow. So this reasonably illustrates the vorticity phenomenon starting from a smooth and low speed flow to a turbulent and high-speed flow.

2.5 Galloping

Simiu and Scanlan (1986) state that galloping is an instability typical of slender structures. This is a relatively low-frequency oscillatory phenomenon of elongated, bluff bodies acted upon by a wind stream. The natural structural frequency at which the bluff object responds is much lower than the frequency of vortex shedding. It is in this sense that galloping may be considered a low-frequency phenomenon. There are two types of galloping: Wake and Across-wind.

***Wake galloping*:** It is considered of two cylinders one windward, producing a wake, and one leeward, within that wake separated at a few diameters distance away from each other. In wake galloping the downstream cylinder is subjected to galloping oscillations induced by the turbulent wake of the upstream cylinder. Due to this, the upstream cylinder tends to rotate clockwise and the downstream cylinder, anti-clockwise thus inducing torsional oscillations.

***Across wind galloping*:** Across wind galloping in a bridge, is an instability that is initiated by a turbulent wind blowing transversely across the deck. Across-wind galloping causes a crosswise vibration in the bridge deck (Liu, 1991). As the section vibrates crosswise in a steady wind velocity U, the relative velocity changes, thereby changing the

angle of attack (α). Due to the change in α, an increase or decrease on the lift force of the cylinder occurs. If an increase of α causes an increase in the lift force in the opposite direction of motion, the situation is stable. But on the other hand if the vice versa occurs, i. e., an increase of α causes a decrease in lift force, then the situation is unstable and galloping occurs. Fig 2.6 gives an illustration of this process.

A classical example of this phenomenon is observed in ice covered power transmission lines. Galloping is reduced in these lines by decreasing the distance between spacing of the supports and increasing the tension of the lines.

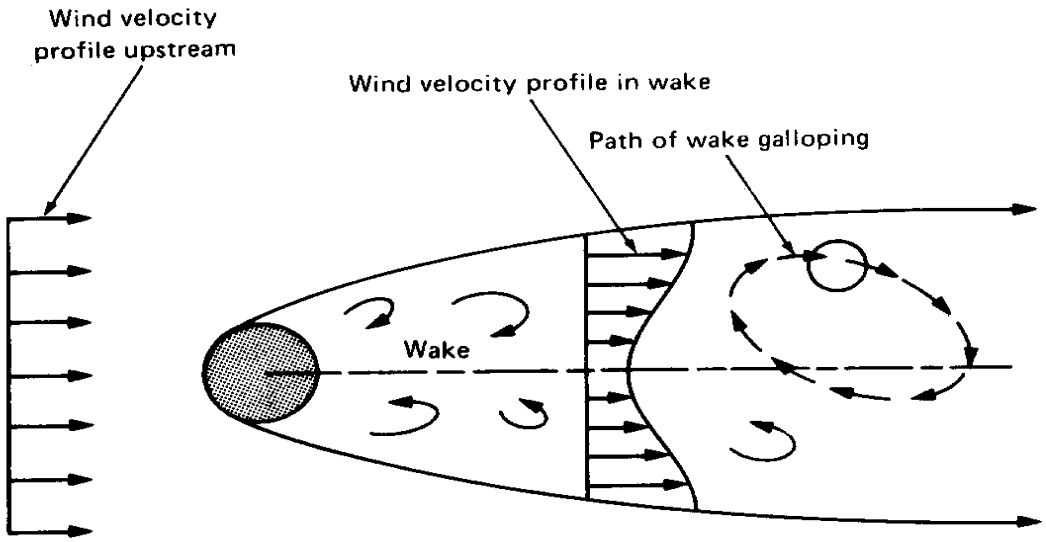

Figure 2.5 Wake galloping

Picture from Simiu and Scanlan (1986)

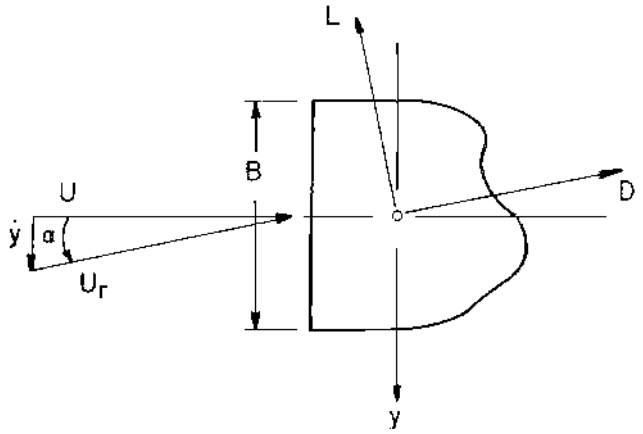

Figure 2.6 Across wind galloping: Wind and motion components, with resultant lift and drag, on a bluff cross section. (Picture from Simiu and Scanlan, 1986)

In the figure,

U ⟶ wind velocity

$U_{r,}$ ⟶ relative wind velocity with respect to moving body

$\dot{y}$ ⟶ velocity across-wind

B ⟶ dimension of the section

L ⟶ lift force

D ⟶ drag force

2.6 Torsional divergence

Torsional divergence is an instance of a static response of a structure. Torsional divergence was at first associated with aircraft wings due to their susceptibility to twisting off at excessive air speeds (Simiu and Scanlan, 1986). Liu, 1991, reports that when the wind flow occurs, drag, lift, and moment are produced on the structure. This moment induces a twist on the structure and causes the angle of incidence α to increase. The increase in α results in higher torsional moment as the wind velocity increases. If

the structure does not have sufficient torsional stiffness to resist this increasing moment, the structure becomes unstable and will be twisted to failure. Simiu and Scanlan, 1986, report that the phenomenon depends upon structural flexibility and the manner in which the aerodynamic moments develop with twist; it does not depend upon ultimate strength. They say that in most cases the critical divergence velocities are extremely high, well beyond the range of velocities normally considered in design.

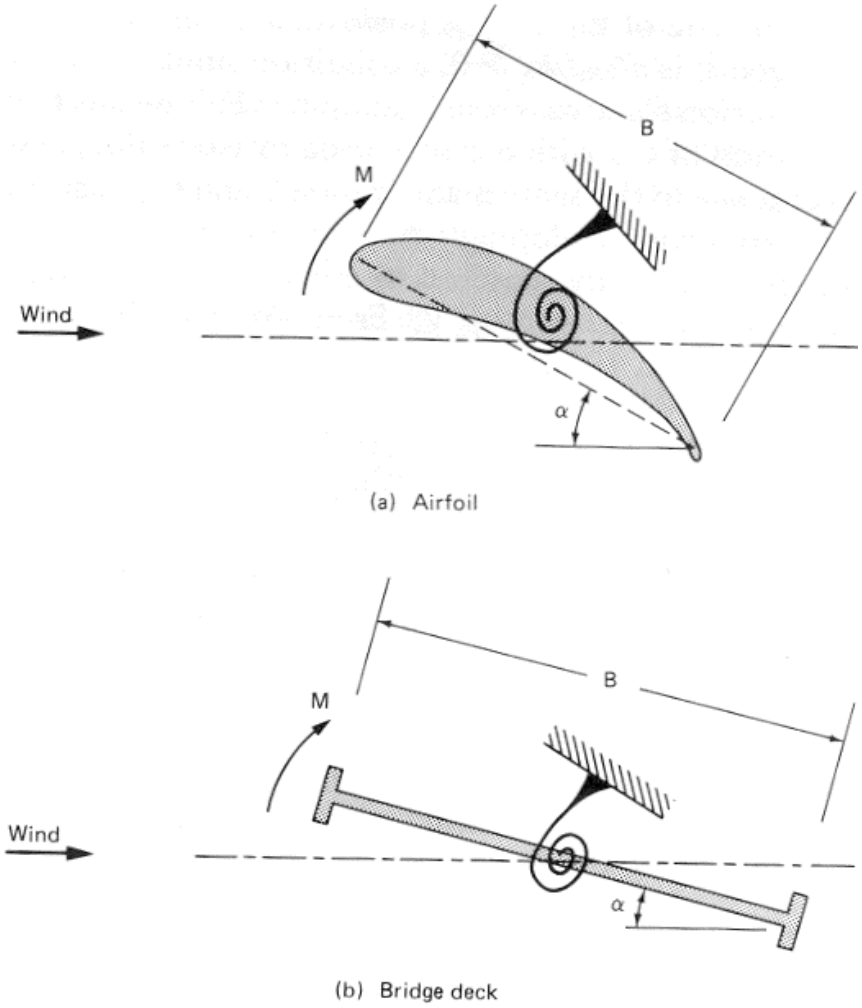

Figure 2.7 a. Torsional divergence of an airfoil

b. Torsional divergence of Bridge deck (Picture from Liu, 1991)

The aerodynamic moment per unit span is given by

$$M_\alpha = \frac{1}{2}\rho U^2 B^2 C_M(\alpha)$$

Where ρ is density, U is the mean wind velocity, B is the deck width, α is the angle of twist and C_M is the aerodynamic moment coefficient about the twisting axis.

At zero angle of attack the value of this moment is

$$M_\alpha(0) = \frac{1}{2}\rho U^2 B^2 C_{M0} \qquad \text{Where } C_{M0} = C_M(0)$$

For a small change in α away from $\alpha = 0$, M_α is approximated as given by

$$M_\alpha = \frac{1}{2}\rho U^2 B^2 \left[C_{M0} + \left(\frac{dC_M}{d\alpha} \right)_{\alpha=0} \alpha \right]$$

Now equating the aerodynamic moment to the structural resisting moment gives

$$\frac{1}{2}\rho U^2 B^2 \left[C_{M0} + \left(\frac{dC_M}{d\alpha} \right)_{\alpha=0} \alpha \right] = k_\alpha \alpha$$

Setting $\lambda = \frac{1}{2}\rho U^2 B^2$, in the above equation, we get

$$\left(k_\alpha - \lambda C'_{M0}\right)\alpha = \lambda C_{M0}$$

$$\Rightarrow \qquad \alpha = \frac{\lambda C_{M0}}{k_\alpha - \lambda C'_{M0}}$$

Divergence occurs when α approaches infinity

i.e., when $\lambda = \frac{k_\alpha}{C'_{M0}}$

Thus the critical divergence velocity is given as

$$U_C = \sqrt{\frac{2k_\alpha}{\rho B^2 C'_{M0}}}$$

2.7 Flutter

The phenomenon of flutter is a very serious concern in the design of bridges. The failure of the Tacoma's narrows bridge was due to the flutter. In the later part of this chapter, a review of the Tacoma's Narrows bridge failure is reported to give a better insight into the flutter-induced instability that resulted in failure. The term flutter has been variously used to describe different types of wind-induced behavior. Flutter can be defined as a condition of negative aerodynamic damping wherein the deflection in the structure grows to enormous levels till failure once started. It is also known as classical flutter. The other types of flutter reported by Simiu and Scanlan (1986) are stall flutter and panel flutter.

Stall flutter is a single-degree-of-freedom oscillation of airfoils in torsion due to the nonlinear characteristics of the lift (Simiu and Scanlan, 1986). The stall flutter phenomenon can also occur with structures having broad surfaces depending on the angle of approaching wind. The torsional oscillation of a traffic stop sign about its post is an example of this phenomenon.

Panel flutter is a sustained oscillation of panels typically the sides of large rockets, caused by the high-speed passage of air along the panel. The most prominent cases have been in supersonic flow regimes and so have not appeared in the wind engineering context. Flag flutter is closely related to panel flutter.

The motion that is caused by the wind flow will either be damped out or will grow indefinitely until failure. The theoretical dividing line between these two states is the critical flutter condition and the wind speed at this condition is called critical wind speed.

2.8 Methods adopted to study critical velocity for flutter

The methods available for studying the aeroleastic instability are the free oscillation method and the forced oscillation method.

2.8.1 Free Oscillation Procedure

This method was used in this work for the study of flutter stability analysis of the structure during motion. In this method the structure is elastically suspended and is given an initial perturbation in terms of heave or pitch and the structure is left to oscillate freely. The lift, drag and moment generated due to the applied displacement is then measured and thus a time history data is generated. The governing equations of motion for translation and rotation are

$$m\ddot{h} + c_h y\dot{h} + k_h h = L \qquad 2.1$$

$$I\ddot{\alpha} + c_\alpha \dot{\alpha} + k_\alpha \alpha = M \qquad 2.2$$

Here m, I, h, α, L and M represents mass, moment of Inertia, heave, pitch, lift and moment respectively. c and k represents damping and stiffness coefficients with the subscripts h and α meaning heave and rotation respectively.

The equations 2.1 and 2.2 can be rewritten as

$$\ddot{h}^* + \left(\frac{\omega_h}{\omega_\alpha}\right)^2 \left(\frac{1}{u^*}\right)^2 h^* = \frac{C_l}{2R_m} \qquad \text{Where } R_m = \frac{m}{\rho B^2} \qquad 2.3$$

$$\ddot{\alpha}^* + \left(\frac{1}{u^*}\right)^2 \alpha^* = \frac{C_m}{2R_I} \qquad \text{Where } R_I = \frac{I_\alpha}{\rho B^4} \qquad 2.4$$

The derivation of 2.3 and 2.4 will be explained in section 4.5 of chapter 4. Thus with the knowledge of the lift and moment forces from CFD calculations, for each instant of time the equations 2.3 and 2.4 are solved incorporating the fluid structure interaction to get the heave and pitch displacements. The pitch angle is then plotted against time. When the pitch angle dies down gradually with the passage of time, it means that the critical flutter velocity is not reached. When the pitch angle keeps growing it means that the critical flutter velocity is reached. Based on these plots the critical flutter velocity is calculated. This process is discussed in detail in chapter 4.

2.8.2 Forced Oscillation Procedure

In this method, the structure is forced in a torsional or heave sinusoidal motion relative to the flow with a prescribed frequency and amplitude (Hansen et. al., 1999). The lift and moment generated due to this applied force is measured and used for the calculation of the aerodynamic derivatives. The calculated aerodynamic derivatives are then used for the computation of the critical velocity for flutter. This process is described below.

The lift and moment loads exerted on an oscillating bridge section with 2 degrees of freedom namely the vertical or heave motion (h) and rotational or pitch motion (α) are given by the following equations (Simiu and Scanlan, 1986).

$$L = \frac{1}{2}\rho U^2 (2B)\left[KH_1^* \frac{\dot{h}}{U} + KH_2^* \frac{B\dot{\alpha}}{U} + K^2 H_3^* \alpha + K^2 H_4^* \frac{h}{B} \right] \quad 2.5$$

$$M = \frac{1}{2}\rho U^2 (2B^2)\left[KA_1^* \frac{\dot{h}}{U} + KA_2^* \frac{B\dot{\alpha}}{U} + K^2 A_3^* \alpha + K^2 A_4^* \frac{h}{B} \right] \quad 2.6$$

Where

$K = \frac{B\omega}{U}$, is the reduced non-dimensional frequency

H_i^* and A_i^* (i =1,2,3,4) ⟶ Aerodynamic derivatives

U ⟶ wind velocity

B ⟶ chord deck width of the bridge

For the pure heave motion, the equations 2.5 and 2.6 become

$$L = \frac{1}{2}\rho U^2 (2B)\left[KH_1^* \frac{\dot{h}}{U} + K^2 H_4^* \frac{h}{B} \right] \quad 2.7$$

$$M = \frac{1}{2}\rho U^2 (2B^2)\left[KA_1^* \frac{\dot{h}}{U} + K^2 A_4^* \frac{h}{B} \right] \quad 2.8$$

For n_S samples, ($L_i, M_i, h_i, \dot{h}$), i =1,2,… n_S, the equations 2.7 and 2.8 constitute two sets of over determined equations, which can be solved in the least squares sense as reported by Walther (1994) as follows.

The least square formulation for solving the equations 2.7 and 2.8 is

$S_H^T S_H x_H = S_H^T q_L$, $\qquad S_A^T S_A x_A = S_A^T q_M$

where $x_H = (H_1^*, H_4^*)$, $x_A = (A_1^*, A_4^*)$ and S_H and S_A are (n_S x 2) matrices

$$S_H = \begin{bmatrix} \rho UBK\dot{h}_1 & \rho U^2K^2h_1 \\ \rho UBK\dot{h}_2 & \rho U^2K^2h_2 \\ . & . \\ . & . \\ \rho UBK\dot{h}_{n_S} & \rho U^2K^2h_{n_S} \end{bmatrix},$$

and $S_A = BS_H$. The right hand side vectors, q_L and q_M are the lift and moment vectors

$$q_L = \left[L_1, L_2, ..., L_{n_S}\right]^T \text{ and } \qquad q_M = \left[M_1, M_2, ..., M_{n_S}\right]^T$$

In a similar fashion, for pure pitch motion, equations 2.5 and 2.6 becomes

$$L = \frac{1}{2}\rho U^2(2B)\left[KH_2^*\frac{B\dot{\alpha}}{U} + K^2H_3^*\alpha\right] \qquad 2.9$$

$$M = \frac{1}{2}\rho U^2(2B^2)\left[KA_2^*\frac{B\dot{\alpha}}{U} + K^2A_3^*\alpha\right] \qquad 2.10$$

and the matrices S_H and S_A are

$$S_H = \begin{bmatrix} \rho UB^2K\dot{\alpha}_1 & \rho U^2BK^2\alpha_1 \\ \rho UB^2K\dot{\alpha}_2 & \rho U^2BK^2\alpha_2 \\ . & . \\ . & . \\ \rho UB^2K\dot{\alpha}_{n_S} & \rho U^2BK^2\alpha_{n_S} \end{bmatrix}$$

and again as before $S_A = BS_H$

Thus the equations 2.7 through 2.10 are solved using the least square principle to obtain the eight aerodynamic derivatives. The aerodynamic coefficients as defined by Larsen and Walther (1996) are as follows.

H_2^*, H_3^* and A_2^*, A_3^* are obtained from time dependent lift and moment coefficients by a pure torsional oscillatory motion described by $\alpha(t) = \alpha \sin(\omega t)$.

$$H_2^* = \frac{-C_L \sin(\phi)}{2\alpha(2\pi)^2}\left(\frac{U}{fB}\right)^2 \quad , \quad H_3^* = \frac{C_L \cos(\phi)}{2\alpha(2\pi)^2}\left(\frac{U}{fB}\right)^2$$

$$A_2^* = \frac{-C_M \sin(\phi)}{2\alpha(2\pi)^2}\left(\frac{U}{fB}\right)^2 \quad , \quad A_3^* = \frac{C_M \cos(\phi)}{2\alpha(2\pi)^2}\left(\frac{U}{fB}\right)^2$$

Oscillatory one degree of freedom excitation in a pure vertical motion described by $h(t) = h \sin(\omega t)$, yields the flutter derivatives H_1^*, H_4^* and A_1^*, A_4^*

$$H_1^* = \frac{-C_L \sin(\phi)}{2(2\pi)^2}\frac{B}{h}\left(\frac{U}{fB}\right)^2 \quad , \quad H_4^* = \frac{C_L \cos(\phi)}{2(2\pi)^2}\frac{B}{h}\left(\frac{U}{fB}\right)^2$$

$$A_1^* = \frac{-C_M \sin(\phi)}{2(2\pi)^2}\frac{B}{h}\left(\frac{U}{fB}\right)^2 \quad , \quad H_1^* = \frac{C_M \cos(\phi)}{2(2\pi)^2}\frac{B}{h}\left(\frac{U}{fB}\right)^2$$

Here, ϕ is the phase shift of the aerodynamic forces with respect to the imposed motion of pure heave or oscillation.

Once the aerodynamic derivatives are computed, they are plugged into the equations of motion for heave and rotation (2.1 and 2.2) as shown below.

$$m\ddot{h} + c_h \dot{h} + k_h h = \frac{1}{2}\rho U^2 (2B)\left[KH_1^*\frac{\dot{h}}{U} + KH_2^*\frac{B\dot{\alpha}}{U} + K^2 H_3^* \alpha + K^2 H_4^*\frac{h}{B}\right] \quad 2.11$$

$$I\ddot{\alpha} + c_\alpha \dot{\alpha} + k_\alpha \alpha = \frac{1}{2}\rho U^2 (2B^2)\left[KA_1^* \frac{\dot{h}}{U} + KA_2^* \frac{B\dot{\alpha}}{U} + K^2 A_3^* \alpha + K^2 A_4^* \frac{h}{B} \right] \quad 2.12$$

Rewriting the above heave equation (2.11), we get

$$\ddot{h} + \frac{c_h \dot{h}}{m} + \frac{k_h h}{m} = \frac{\rho U^2 B}{m}\left[KH_1^* \frac{\dot{h}}{U} + KH_2^* \frac{B\dot{\alpha}}{U} + K^2 H_3^* \alpha + K^2 H_4^* \frac{h}{B} \right]$$

Substituting angular frequency in heave, ω_h and damping ratio in heave, ζ_h

$$\omega_h^2 = \frac{k_h}{m} \qquad\qquad \zeta_h = \frac{c_h}{2m\omega_h}$$

we get,

$$\ddot{h} + 2\zeta_h \omega_h \dot{h} + \omega^2 h = \frac{\rho U^2 B}{m}\left[KH_1^* \frac{\dot{h}}{U} + KH_2^* \frac{B\dot{\alpha}}{U} + K^2 H_3^* \alpha + K^2 H_4^* \frac{h}{B} \right] \quad 2.13$$

In a similar fashion, the equation for rotational motion follows as

$$\ddot{\alpha} + 2\zeta_\alpha \omega_\alpha \dot{\alpha} + \omega_\alpha^2 \alpha = \frac{\rho U^2 B^2}{I}\left[KA_1^* \frac{\dot{h}}{U} + KA_2^* \frac{B\dot{\alpha}}{U} + K^2 A_3^* \alpha + K^2 A_4^* \frac{h}{B} \right] \quad 2.14$$

These two differential equations (2.13 & 2.14) are now based on the observation, that h and α are harmonic in time with a common frequency at the critical wind speed for the onset of flutter. The representation of heave and pitch in the complex notation is used in solving the flutter deterministic equations 2.13 and 2.14. The critical velocity for flutter is then calculated by plotting curves corresponding to the roots of the real and imaginary parts of the flutter determinant equation against the non-dimensional wind velocity as illustrated by Walther, 1994 and Larsen, 1995. The intersection point $\left[\left(\frac{U}{\omega B} \right)_c, X_c \right]$ between the real and imaginary root curves defines the critical wind speed for flutter as

$$U_c = \left(\frac{U}{\omega B} \right)_c X_c \omega_h B$$

where U_c is the critical flutter velocity and X_c is the ordinate of the point of intersection in the plot.

2.9 Critical wind speeds for Flutter

When the critical wind speed for flutter is exceeded, the structure will become unstable and experience excessive deflections. Hence it is an important factor to be considered in design. Arrol and Chatterjee (1981) mention the following guidelines.

Vortex shedding: With respect to vortex shedding, if the critical wind speed for resonance in vertical and torsional modes (vertical modes only for trusses) is greater than the reference wind speed, the static and fatigue stress effects need to be checked from amplitude calculations appropriate to the mode shape.

Turbulence Response: If the natural frequency in first mode for vertical or torsional deflection is greater than 1 Hz, a dynamic analysis for stress effects need to be carried out to account for it.

Classical and Stall flutter: For prevention of this type of instability, the critical wind speed is to be greater than 1.3 times reference speed. The designer must ensure one of the following. The critical wind speed exceeds the practical limiting value for the given site or the resulting amplitudes are of allowable levels. Criteria for acceptability may include considerations of fatigue or of user reaction as well as of ultimate strength.

2.10 Buffeting

Buffeting is defined as the unsteady loading of a structure by velocity fluctuations in the incoming flow and not self-induced (Simiu and Scanlan, 1986). Buffeting vibration is the vibration produced by turbulence. There are two types of buffeting. One type is caused by turbulence in the airflow, and the other type is caused by disturbances generated by an upwind neighboring structure or obstacle. The first type of buffeting can produce significant vertical and torsional motions of a bridge even at low speeds. This buffeting induced motion results in a gradual transition to large amplitude torsional oscillations, which could lead to the failure of a bridge. If the velocity fluctuations are clearly associated with the turbulence shed in the wake of an upstream body, the unsteady loading is referred to as wake buffeting. Wake buffeting is common in urban areas with many tall structures.

2.11 Tacoma Narrows Bridge Failure

The Tacoma Narrows Bridge failure in 1940, at Washington, USA is a classical example of the aerodynamic instability failure. Wind wrecked the 2800-ft. main span of the bridge on Nov 7, 1940. A wind of 42 mph was responsible for the accident, though higher winds had been experienced previously without damage (Bowers 1940). He reports that this wind caused a vertical wave motion that developed a lag or phase difference between opposite sides of the bridge giving the deck a cumulative rocking or side-to-side rolling motion. Failure appeared to begin at mid-span with buckling of the stiffening girders. The suspenders snapped and their ends jerked high in the air above the main cables, while sections of the floor system several hundred feet in length fell out

successively breaking up the roadway toward the towers. Almost the entire suspended structure between the towers was ripped away and fell into the waters below, but the 1100-ft. side spans remained intact. Cables and towers survived and held up the weight of the side spans, though the latter sagged about 30-ft. as the towers went back sharply by the unbalanced pull of the side-span cables. Bowers reports that about five weeks before the failure, on the chance that an aerodynamic failure might be found, a 1:20 model of the deck was built and was tested in the wind tunnel. The tests showed the model to be aerodynamically unstable in certain winds and this condition was concluded to be the source of the oscillations of the bridge itself. The wind tunnel test was followed by studies towards remedial measures aimed at modifications that would improve the characteristics of the bridge. A contract for the installation of the deflector vanes was under negotiation when the collapse occurred.

The following pictures, Figures 2.8 –2.13 give an understanding of the instabilities the bridge suffered and also shows the mode of collapse during failure.

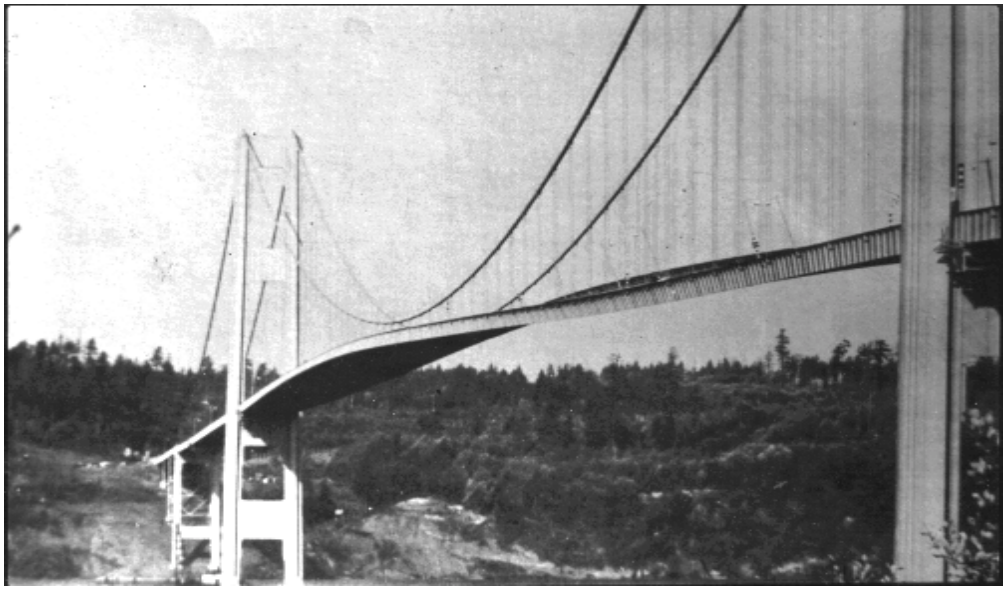

Figure 2.8: This photograph shows the twisting motion of the center span just prior to failure.

Figure 2.9: The nature and severity of the torsional movement is revealed in this picture taken from the Tacoma end of the suspension span. When the twisting motion was at the maximum, elevation of the sidewalk at the right was 28 feet (8.5m) higher than the sidewalk at the left.

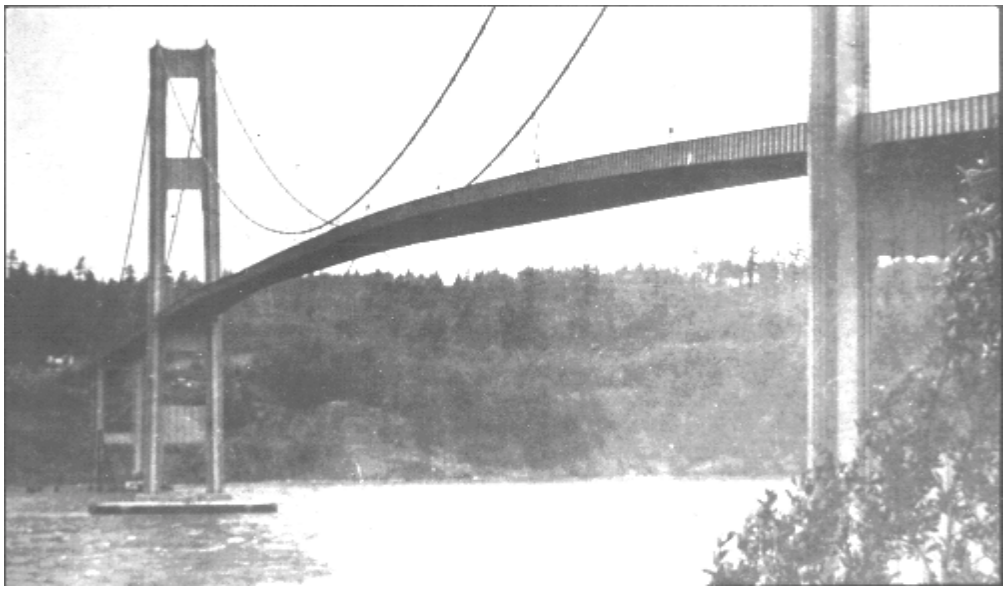

Figure 2.10: This photograph actually caught the first failure shortly before 11 o'clock as the first concrete dropped out of the roadway. Also note bulges in the stiffening girder near the far tower and also in the immediate foreground.

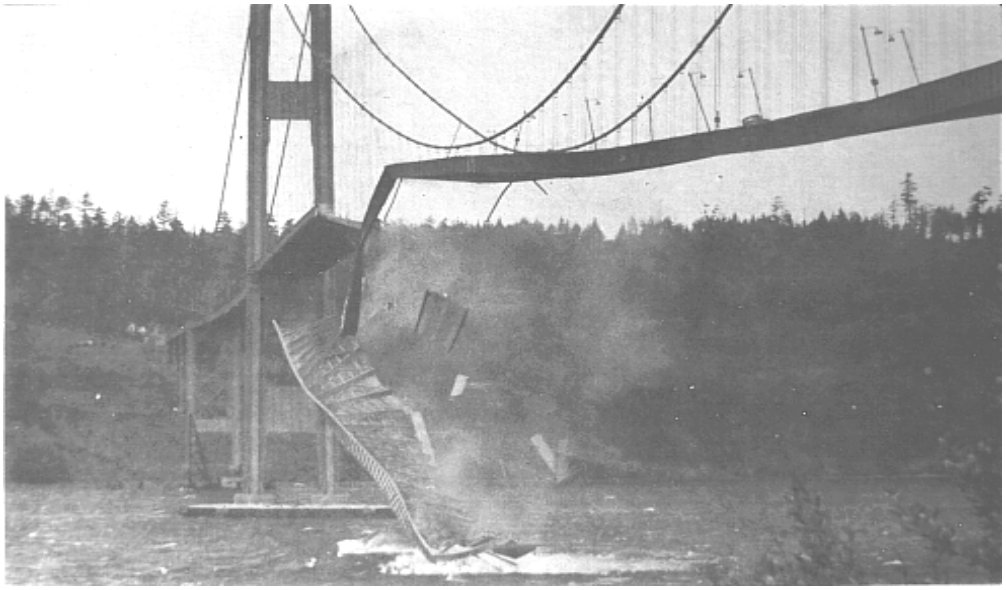

Figure 2.11: A few minutes after the first piece of concrete fell, this 600 foot section broke out of the suspension span, turning upside down as it crashed in Puget Sound. Note how the floor assembly and the solid girders have been twisted and warped. The square object in mid air (near the center of the photograph) is a 25-foot (7.6m) section of concrete pavement. Notice the car in the top right corner.

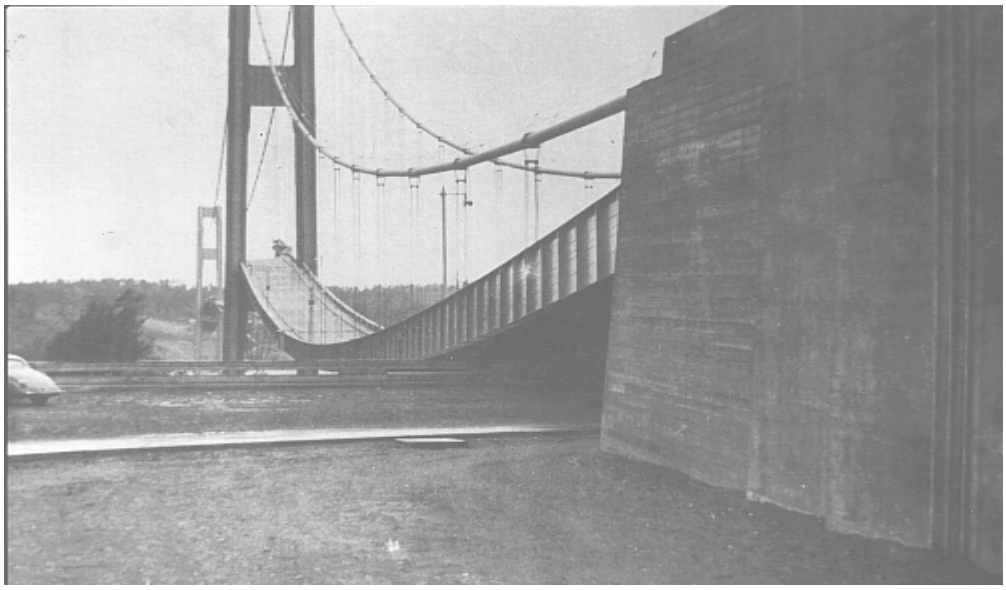

Figure 2.12: This photograph shows the sag in the east span after the failure. With the center span gone there was nothing to counter balance the weight of the side spans. The sag was 45 feet (13.7m). Also the immense size of the anchorage is illustrated.

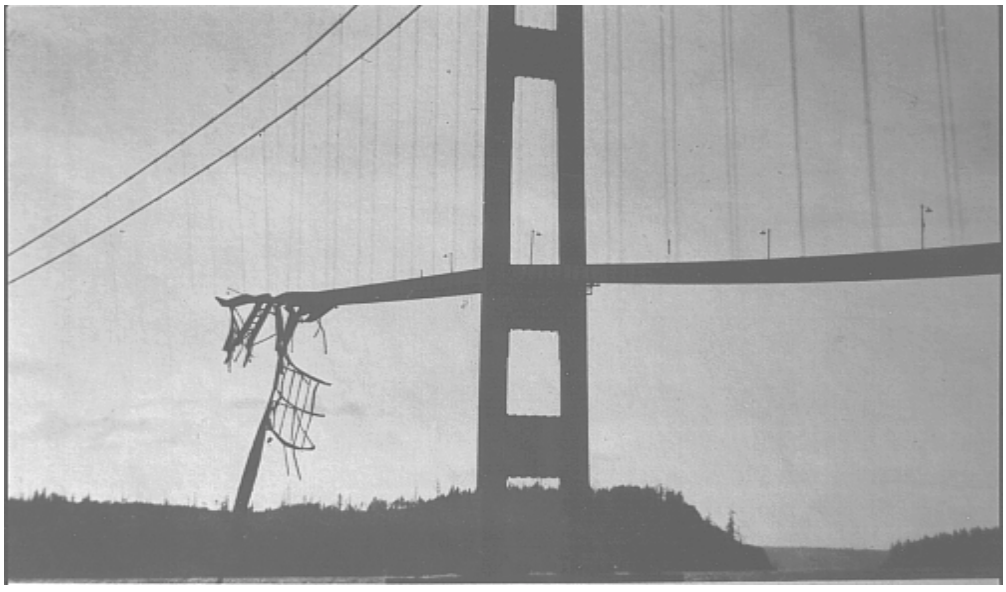

Figure 2.13: This picture was taken shortly after the failure. Note the nature of the twists in the dangling remainder of the south stiffening girder and the tangled remains of the north stiffening girder.

CHAPTER 3

LITERATURE REVIEW

3.1 Introduction

In this chapter, a brief survey of the literature and work done by various researchers with regard to the modeling of flow around bridges is investigated and reported. The different numerical procedures and turbulence models that are used in the computational wind engineering are reviewed. The problems and issues in the fluid structure interaction modeling is also discussed in this chapter. Many researchers have worked on the Great Belt East Bridge section because there is extensive wind tunnel results against which their computer models could be validated.

3.2 Techniques for modeling the wind flow

The methodology to be used in the modeling of flow involves solving the structure and fluid equations simultaneously incorporating the fluid structure interaction. The solution is based upon a grid that is generated in the domain of the fluid flow around the structure. The generation of the grid is very important and critical in order to get the correct results. The grid generation involves several issues that need to be addressed. Hence those details are discussed in a separate chapter. The different types of methods that are adopted to solve the governing equations are the Finite Element Method (FEM), Finite Difference Method (FDM) or the Discrete Vortex Method (DVM). The turbulence in the flow is to be modeled using a turbulence model. The widely used turbulence

models are the Reynolds averaged Navier-Stokes (RANS), Large Eddy Simulation (LES) and Vortex Method (VM).

3.2.1 Computational Methods

When compared with FEM, the FDM takes less computational time and storage space for the same number of grid points. These are some of the advantages of FDM over FEM. But at the same time FDM is geometrically restrictive whereas FEM is good for complex geometrical shapes and is flexible to impose any type of boundary conditions. Also, the accuracy of the FEM is much higher than that of FDM. (Hughes, 1993). FEM can approximate the convection term in the Navier-Stokes equations with more accuracy than FDM (Selvam, 1998).

The FEM and FDM approximates the unknowns into a set of simultaneous equations of the type AX=B. These equations can be solved by many procedures like Gauss-elimination, Gauss-Seidel and Preconditioned conjugate gradient (PCG) methods. Though the solving of pressure equation takes 80% of the time, the usage of Preconditioned conjugate gradient (PCG) solver makes the iterations faster and speeds up the convergence (Selvam, 1994). Larsen and Walther (1996a) have demonstrated reasonably good success with DVM, but it takes a lot of time and storage space for the 3D model. In this work, the FEM was used for a grid size of 14805 points and the 2D model was able to predict the vortex shedding vividly and the flutter velocity predicted was in good agreement with wind tunnel results.

3.2.2 Turbulence Models

In computational wind engineering, the phenomenon of turbulence can be modeled by Reynolds Averaged Navier-Stokes equations (RANS), Direct Numerical Simulation (DNS), and Large Eddy Simulation (LES) as reported by Selvam (1995 and 1998). The relative merits and demerits of these three methods are discussed below.

3.2.2.1 Reynolds Averaged Navier-Stokes equations (RANS)

The RANS model is widely used in computational wind engineering to model turbulent flow. This model uses time - independent equations and solves for Reynolds averaged stresses, which represent the effect of turbulence on the model. Based on the type of solving Reynolds stresses, the RANS model represents different methods. These methods are Eddy Viscosity Models (EVM), Reynolds Stress Models (RSM), and the Algebraic Stress Models (ASM). Different EVM models are available including zero-equation models, one-equation models and two-equation models. The most commonly used form is the $k-\varepsilon$ model, which is used by Selvam (1990 and 1992) to compute wind-induced pressures around buildings. These models are further explained in Selvam (1992a) and compared in Selvam (1995). To solve for Reynolds stresses, the RSM model requires six partial differential equations with an additional equation for dissipation. Hence, the RSM model requires more computer time and storage. Comparing to RSM, the Reynolds stresses are calculated using algebraic equations rather than solving partial differential equations as in the ASM model. The ASM model consumes less computer time in comparison with the RSM model.

The $k-\varepsilon$ model is quite popular and can simulate a variety of flows. Its main practical limitation is the assumption of isotropic eddy viscosity. Another disadvantage of this method is that it cannot give time-dependent value like peak pressure.

3.2.2.2 The Direct Numerical Simulation (DNS)

In DNS, all eddies down to the dissipation scale must be simulated with accuracy. This drastically increases the number of grid points and so consumes much more computer time and storage. It is usually not economical to apply this method to wind engineering problems with available computer resources.

3.2.2.3 The Large Eddy Simulation (LES)

The LES model uses time dependent equations and has the advantage of generating a time dependent flow field. In the LES model, eddies which are larger than the grid size, are simulated. The smaller eddies, occurring below the limit of numerical resolution, are simulated using other methods, such as eddy viscosity model (Selvam, 1997). Eddies significantly larger than the grid size are calculated in detail so that their turbulent properties are modeled correctly. Selvam (1997) and Selvam and Peng (1997 and 1998) used this model to compute pressures on the Texas Tech University (TTU) building. The disadvantage of this model is that it consumes more computer time and storage than the RANS. Due to developments in computer techniques, it is possible to use LES for the prediction of wind problems. In this report, the LES turbulence model is used.

3.3 Fluid-Structure Interaction (FSI) Modeling

The FSI problem is intricate and complicated to solve because the structural equations are formulated in the Lagrangian co-ordinate system whereas the fluid equations are in the Eulerian co-ordinate system (Selvam and Govindaswamy, 2000). They also state that the FSI modeling needs the simultaneous solving of both the equations of structure and fluid. A moving grid at each time step for the fluid portion is necessary for the solution process. The different approaches in use at this time are Arbitrary Lagrangian-Eulerian (ALE) formulation (Nomura and Hughes, 1992, Selvam et al. 1998 and Tamura et al., 1995), co-rotational approach (Murakami and Mochida, 1995) and dynamic meshes (De Sampaio et al., 1993).

The co-rotational approach may be easier to implement by adding extra terms in the Navier-Stokes (NS) equations for movements in one direction. Therefore, it will be difficult to apply for general problems. In the dynamic mesh approach, for each time step a new mesh is formulated and hence needs a very sophisticated grid generator. In the ALE approach, grid can be moved as a whole in a rigid fashion with constant velocity for each node as reported by Tamura et. al. (1995) or with different velocity for each node in a flexible manner as reported by Selvam et. al. (1998) and Nomura and Hughes (1992). Moving the grid, as a whole is preferred for FSI problem since the structure has rigid body movement. If the structure is very flexible and each node on the structure is moving, then the latter grid moving procedure has to be used. In the ALE procedure, geometric conservation laws (GCL) are violated if the equations are solved as such (Thomas & Lombard, 1979 and Ferziger & Peric, 1999). In this work the GCL error is reduced by using the corrections similar to the one reported by Thomas & Lombard, 1979

and Ferziger & Peric, 1999. Moving the grid as a whole may be computationally easy to apply. In this work the bridge deck is assumed to be rigid and the rigid body moving technique is used in this research.

The critical flutter velocity can be calculated using free oscillation procedure or forced oscillation procedure as explained in chapter two. The free oscillation procedure was used by Frandsen & McRobie (1999), Enevoldsen et al. (1999), Nomura & Hughes (1992), Mendes & Branco (1995) and Selvam et al. (1998). Larsen and Walther (1997) and Enevoldsen et. al. (1999) used the forced oscillation procedure. In this work the free oscillation procedure is used and the critical flutter velocity is computed in a few computational runs.

CHAPTER 4

COMPUTER MODELING

4.1 Introduction

In this chapter, the underlying concepts related to the computer modeling of the flow around bridges are discussed. The issues related to solving the equations of structure and fluid numerically are explained with reference to the Fluid Structure Interaction. The solution procedures and the pertinent equations for the fluid and the structure are stated and enunciated. The relevant boundary and initial conditions and the advantages of the solution procedures adopted are also studied.

4.2 The Structure

The structure used in this work is the Great Belt East Bridge(GBEB) girder section. The GBEB is a 3 span box girder suspension bridge of span lengths 535m-1624m-535m, which carries a four-lane motorway across the international shipping route of the Great Belt, Denmark (Larsen et. al. 1999). The design of the bridge was initiated in 1989 and opened to traffic in 1998 after construction. Two different cross-sections were used for the approach and the suspension spans as shown in Figures 4.2 and 4.3. From Figure 4.1, it can be seen that the center of gravity for the suspension section is different from the shear center and lies above the shear center. This is worth noting in the sense that the section rotates about the shear center due to the moment, whereas the translational displacement occurs about the center of gravity. Since both are located along the line of symmetry, there is no coupling of the rotational and translational

displacements. Tacoma's Narrows bridge is also shown here as a comparison against the GBEB bridge section.

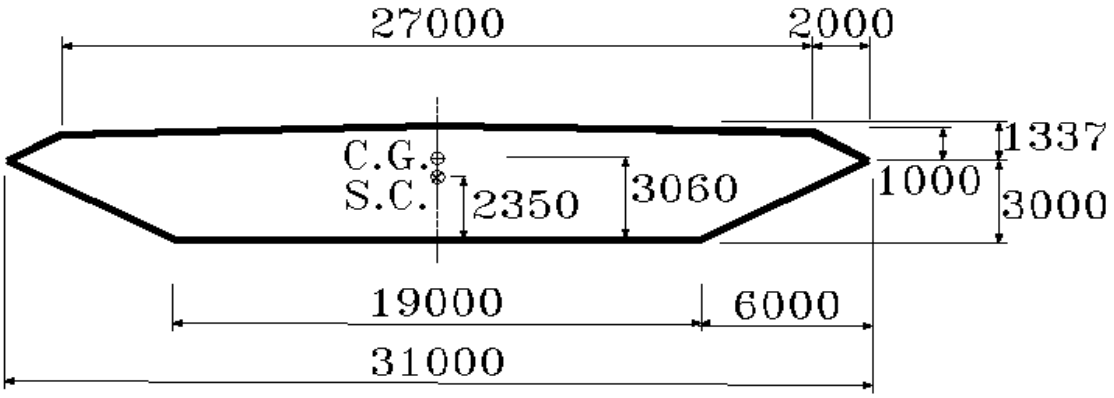

Figure 4.1 Cross-section of the Great Belt East Bridge (GBEB) suspension span. (All dimensions are in mm). Picture from Walther, 1994.

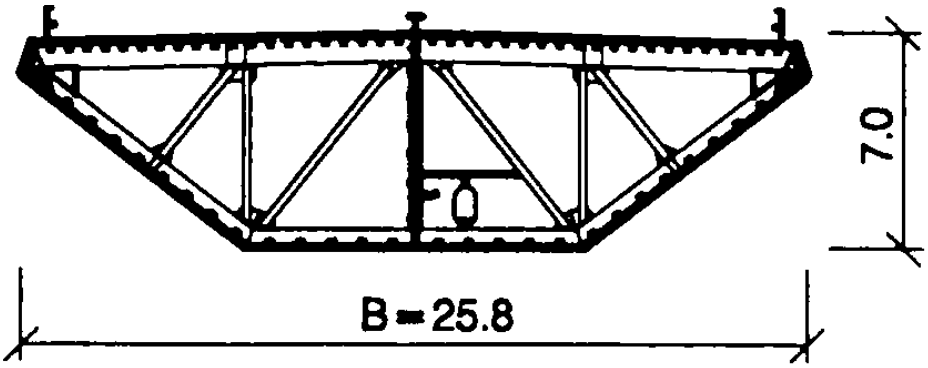

Figure 4.2 Great Belt East Bridge girder - Approach span

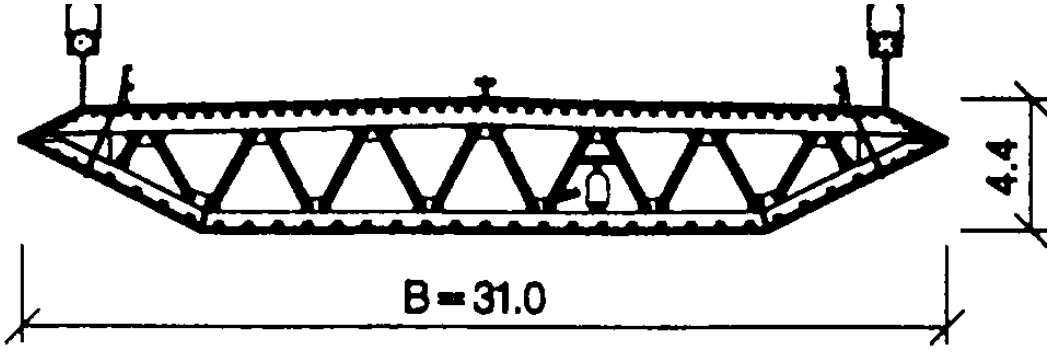

Figure 4.3 Great Belt East Bridge girder - Suspension span

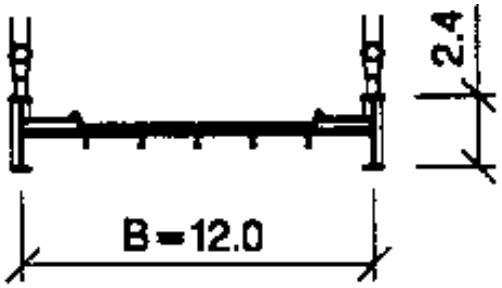

Figure 4.4 1st Tacoma Narrows Bridge

(The pictures of bridge cross-sections are from Larsen and Walther, 1996)

Structural property	Mass(Kg/m)	Inertia(Kgm^2/m)	f_h (Hz)	f_α (Hz)
GBEB Suspension	$22.7*10^3$	$2.47*10^6$	0.099	0.272
GBEB Approach	$16.0*10^3$	$1.05*10^6$	0.46	2.76
1st Tacoma Narrows	$1.3*10^3$	$28.19*10^3$	0.13	0.20

Table 4.1. Structural properties of bridge cross sections (Larsen 1996).

4.3 Flow Parameters

The flow is characterized by parameters like Reynolds number, Strouhal number, coefficient of drag force, lift force and moment. They are defined as follows.

$$R_e = \frac{VB}{\upsilon} \tag{4.1}$$

$$C_d = \frac{F_x}{0.5\rho V^2 BW}$$

$$C_l = \frac{F_y}{0.5\rho V^2 BW}$$

$$C_m = \frac{M}{0.5\rho V^2 B^2 W}$$

$$S_t = \frac{H}{TV}$$

Where

B, H, W ⟶ width, height, length in the z direction of the bridge respectively

F_x, F_y ⟶ drag and lift forces

V ⟶ reference velocity,

υ ⟶ kinematic viscosity,

M ⟶ moment

T ⟶ period of oscillation of the lift forces

ρ ⟶ density.

For 2D computation, W is considered to be one.

4.4 Governing Equations for Flow

In the modeling, the fluid is assumed to be viscous and incompressible and the Navier Stokes equations are used to study and describe the fluid flow around the bridge girder. The governing Navier Stokes equations in two and three-dimensions for an incompressible fluid using the Large Eddy Simulation (LES) model in general tensor notation, as reported by Selvam (2000) are as follows.

Continuity Equation: $U_{i,i} = 0$ 4.2

Momentum Equation: $U_{i,t} + (U_j - V_j)U_{i,j} = -(\frac{p}{\rho} + \frac{2k}{3}),_i + [(\upsilon + \upsilon_t)(U_{i.j} + U_{j,i})],_j$ 4.3

where

$\upsilon_t = (C_s h)^2 \sqrt{S_{ij}^{\ 2} / 2}$,

$S_{ij} = U_{i,j} + U_{j.i}$,

$h = \sqrt[3]{h_1 h_2 h_3}$ for 3D

$h = \sqrt{h_1 h_2}$ for 2D

$k = \left(\frac{\upsilon_t}{C_k h} \right)^2$

Empirical constants C_s=0.15 for 2D and 0.1 for 3D and C_k=0.094

Here

U_i ⟶ mean velocity

p ⟶ pressure

V_i ⟶ grid velocity

k ⟶ turbulent kinetic energy

υ_t ⟶ turbulent eddy viscosity

ρ ⟶ fluid density

h_1, h_2 and h_3 ⟶ control volume spacing in the x, y, z directions

For the computation of h, the area is used if it is a two-dimensional model or the volume is used if the model is three-dimensional. Here a comma represents differentiation, t represents time and i=1, 2 and 3 mean variables in the x, y and z directions. Selvam (2000,1998b) reports that to implement higher order approximation of the convection term the following expression is used in Equation 4.3 instead of $U_j U_{i,j}$

$$(U_j - V_j)U_{i,j} - \theta[(U_j - V_j)(U_k - V_k)U_{i,j}],_k / 2 \qquad 4.4$$

He states that depending upon the values of θ, different procedures can be implemented. For balance tensor diffusivity (BTD) scheme, $\theta = \delta t$ is used; where δt is the time step used in the integration. For streamline upwind procedure suggested, θ is considered as:

$$\theta = 1/\max\left(|U_1|/dx, |U_2|/dy, |U_3|/dz\right) \qquad 4.5$$

Here

dx, dy and dz ⟶ control volume length

U_1, U_2 and U_3 ⟶ velocities in the x, y and z directions

In this computation $\theta = \delta t$ is used. This has less numerical diffusion as compared to benchmark problems in Selvam (1998). For moving grid the maximum of the BTD or 0.3 times equation 4.5 is considered for better stability of the solution.

4.5 Governing Equations for Structure

When the wind flows over the structure, the structure is subjected to both translation (vertical) and rotational (twisting) motion. Figure 4.5 shows the GBEB section with both the vertical and rotating degrees of freedom. The differential equations describing both these types of motion are as follows. The equations are non-dimensionalised with respect to the dimension B and then solved in a non-dimensional form. The non-dimensionalised representation of time(t), vertical displacement(y), angular displacement(α) and velocity(V) are as shown below. The asterisk represents the non-dimensional value.

$$t^* = \frac{tV_\infty}{B} \quad ; \qquad y^* = \frac{y}{B} \quad ; \qquad \overset{*}{\alpha} = \alpha \quad ; \quad u^* = \frac{V_\infty}{\omega B}$$

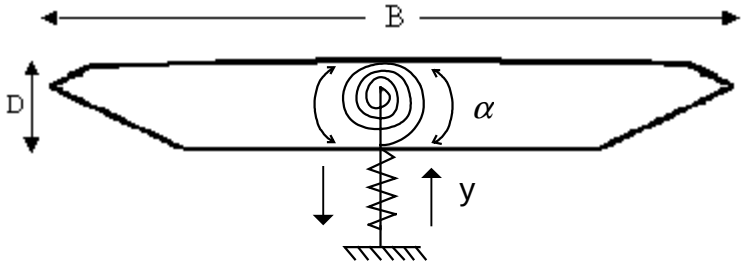

Fig 4.5 Structural model of the GBEB section.

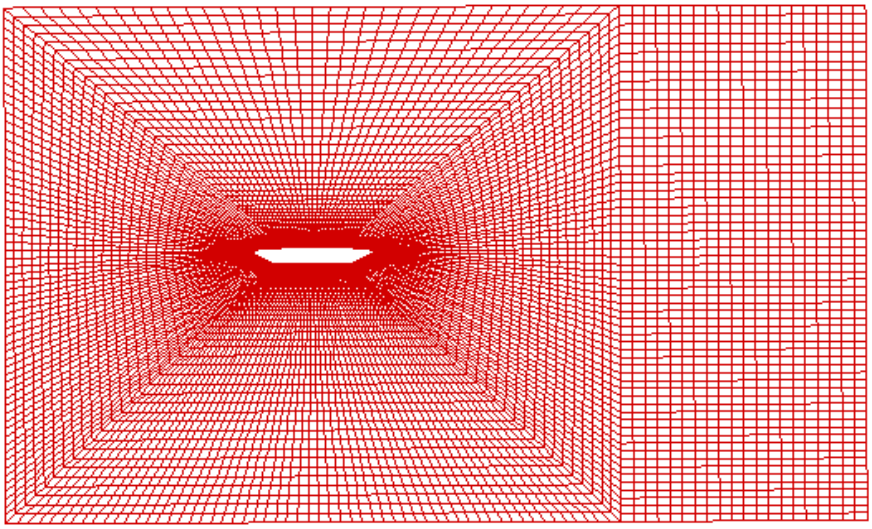

Fig 4.6 The FEM grid system of the suspension span of the GBEB section.

4.5.1 Translation motion

The differential equation for the translatory motion is given by

$$m\ddot{y} + K_h y = F_l(t) \qquad 4.6$$

where F_l ⟶ Lift force as described in section 4.3

K_h ⟶ vertical stiffness

y ⟶ vertical displacement

$\ddot{y}$ ⟶ vertical acceleration

$m \longrightarrow$ mass

Rewriting equation (4.6) gives

$$\ddot{y} + \omega_h{}^2 y = \frac{F_l(t)}{m} \qquad \text{where } \omega_h^2 \longrightarrow \frac{K_h}{m} \qquad 4.7$$

Non-dimensionalising each of the terms in the above equation, we get

$$\dot{y} = \frac{dy}{dt} = \frac{d(By^*)}{d\left(\frac{t^* B}{V_\infty}\right)} \qquad \text{where } y = By^* \text{ and } t = \frac{t^* B}{V_\infty}$$

The second derivative becomes

$$\ddot{y} = \frac{d^2 y}{dt^2} = \frac{d^2(By^*)}{d\left(\frac{t^* B}{V_\infty}\right)^2} = \frac{V_\infty{}^2}{B}\frac{d^2 y^*}{dt^{*2}}$$

Now substituting the non-dimensional terms $\ddot{y}$ and $\dot{y}$ and rewriting equation 4.7 in non-dimensional terms, we get

$$\frac{V_\infty{}^2}{B}\ddot{y}^* + \omega_h{}^2 B y^* = \frac{F_l(t)}{m} \qquad 4.8$$

Multiplying both sides of (4.8) by $\frac{B}{V_\infty{}^2}$ gives

$$\ddot{y}^* + \omega_h{}^2 \frac{B^2}{V_\infty{}^2} y^* = \frac{F_l(t)}{m}\frac{B}{V_\infty{}^2} \qquad 4.9$$

Now including the lift force, $F_l(t) = 0.5 C_l \rho V_\infty{}^2 B$ and non-dimensional form of velocity $V_\infty = u^* \omega_h B$ into 4.9, we get the final dynamic equation for translation in the non-dimensional form as follows.

$$\ddot{y}^* + \left(\frac{\omega_h}{\omega_\alpha}\right)^2 \left(\frac{1}{u^*}\right)^2 y^* = \frac{C_l}{2R_m} \quad \text{where } R_m = \frac{m}{\rho B^2} \tag{4.10}$$

4.5.2 Rotational Motion

The differential equation for rotational motion is given by

$$I_\alpha \ddot{\alpha} + K_\alpha \alpha = M_\alpha(t) \tag{4.11}$$

where I_α ⟶ Mass moment of inertia

α ⟶ Angular displacement

$\ddot{\alpha}$ ⟶ Angular acceleration

K_α ⟶ Rotational stiffness

$M_\alpha(t)$ ⟶ Force due to moment

Proceeding in the same manner as previously, rewriting equation (4.11) gives

$$\ddot{\alpha} + \omega_\alpha{}^2 \alpha = \frac{M_\alpha(t)}{I} \qquad \text{where } \omega_\alpha^2 \longrightarrow \frac{K_\alpha}{I_\alpha} \tag{4.12}$$

Non-dimensionalising each of the terms in the above equation, we get

$$\dot{\alpha} = \frac{d\alpha}{dt} = \frac{d(\alpha^*)}{d\left(\frac{t^* B}{V_\infty}\right)} \qquad \text{where } \alpha = \alpha^* \text{ and } t = \frac{t^* B}{V_\infty}$$

The second derivative becomes

$$\ddot{\alpha} = \frac{d^2\alpha}{dt^2} = \frac{d^2(B\alpha^*)}{d\left(\frac{t^* B}{V_\infty}\right)^2} = \frac{V_\infty{}^2}{B^2} \frac{d^2\alpha^*}{dt^{*2}}$$

Now substituting the non-dimensional terms $\ddot{\alpha}$, $\dot{\alpha}$ and rewriting equation 4.12 in non-dimensional terms, we get

$$\frac{V_\infty{}^2}{B^2}\ddot{\alpha}^2 + \omega_\alpha{}^2\alpha^* = \frac{M_\alpha(t)}{I_\alpha} \qquad 4.13$$

Multiplying both sides of (4.13) by $\frac{B^2}{V_\infty{}^2}$ gives

$$\ddot{\alpha}^* + \omega_\alpha{}^2\frac{B^2}{V_\infty{}^2}\alpha^* = \frac{M_\alpha(t)}{I_\alpha}\frac{B^2}{V_\infty{}^2} \qquad 4.14$$

Now including the lift force, $M_\alpha(t) = 0.5C_m\rho V_\infty{}^2 B^2$ and non-dimensional form of velocity $V_\infty = u^*\omega_\alpha B$ into 4.14, we get the final dynamic equation for rotation in the non-dimensional form as follows.

$$\ddot{\alpha}^* + \left(\frac{1}{u^*}\right)^2\alpha^* = \frac{C_m}{2R_I} \quad \text{where } R_I = \frac{I_\alpha}{\rho B^4} \qquad 4.15$$

The ratio of the frequency of heave and pitch oscillation is a factor called *whp* that is used in the computations.

The parameters R_I, R_m and *whp* are calculated from the physical properties of the GBEB bridge girder for an air density of ρ =1.228 kg/m^3 as given below.

$$R_I = \frac{I_\alpha}{\rho B^4} = 2.178$$

$$R_m = \frac{m}{\rho B^2} = 19.236$$

$$whp = \frac{\omega_h}{\omega_\alpha} = 0.364$$

4.6 Computational Grid

A structured body conforming grid was used for the GBEB bridge section in the simulation process. As mentioned in the grid generation chapter, several issues like variation of spacing, aspect ratio, alignment and size and shape of the elements, optimum number of elements is to be considered. Four different grids are generated keeping in mind the parameters like the total number of nodes, spacing close to the bridge deck and the concentration of density in flow separation regions. The finite element code was run using these four grids in order to assess the influence of the grid parameters on the results.

The grids A and B were generated by an in-house program developed by the author. In this program, each line segment of the bridge cross-section was divided into zones and the desired number of grid points in each of the zones was fed as an input in the data file. The spacing among the points in each zone is calculated by the series of geometric progression. At the intersection of the two line segments of the bridge cross-section, a smooth transition of the grid is ensured by merging the spacing of the previous zone into the start of a new zone. Within each zone the spacing is varied in an increasing or decreasing fashion according to the direction and nature of the flow occurring around that region of the cross-section. Controlling the common ratio in the geometric series of progression effects the desired rate of increase/decrease in the variation of spacing. Here, the common ratio is defined as the percentage increase or decrease from the previous value.

The other two grids, namely C and D, were developed using the software GRIDGEN (Version 9) developed by NASA Ames Research Center. This software is

sophisticated and has more options for the grid generation process. This offers the choice of several blending functions and grid point distribution functions. A lot of details are mentioned in the Gridgen user manual. It has solvers like elliptic PDE solver and algebraic solver that can be iteratively applied to the grid to smoothen it. With GRIDGEN, two highly refined grids, C and D with a spacing of 0.0033 and 0.00065 respectively was developed. The elliptic PDE solver was used to refine and smoothen the grid. The tanh grid point distribution function was used in spacing the grid points radially from the corner of the bridge section to the outer boundary of the fluid domain. The details of the grid types A, B, C and D are given in Table 5.2. The pictures of the grid used are shown in Figures 4.9 through 4.14.

Grid Type	Grid Points	Elements	Nodes	Spacing close to deck
A	216 x 57	13515	13280	0.002
B	216 x 63	14805	14570	0.001
C	302 x 65	20745	20424	0.0033
D	312 x 57	18807	18476	0.00065

Table 4.2 Specifications of the configuration of the various grid types used.

4.7 Boundary and Initial conditions

The computational domain and the boundary conditions used are illustrated in Fig 4.1 for the fixed grid as reported by Selvam and Govindaswamy (2000). They also state that the cylinder surface has no slip condition. The upstream boundary has uniform velocity of one in the x direction and zero in the y direction. At the outflow boundary the normal

gradient of the velocities are zero and the sides have slip boundaries. The computation is done for Re of 10^5.

Figure 4.7 shows the schematic representation of the domain chosen for the problem and the boundary conditions applied in the computations.

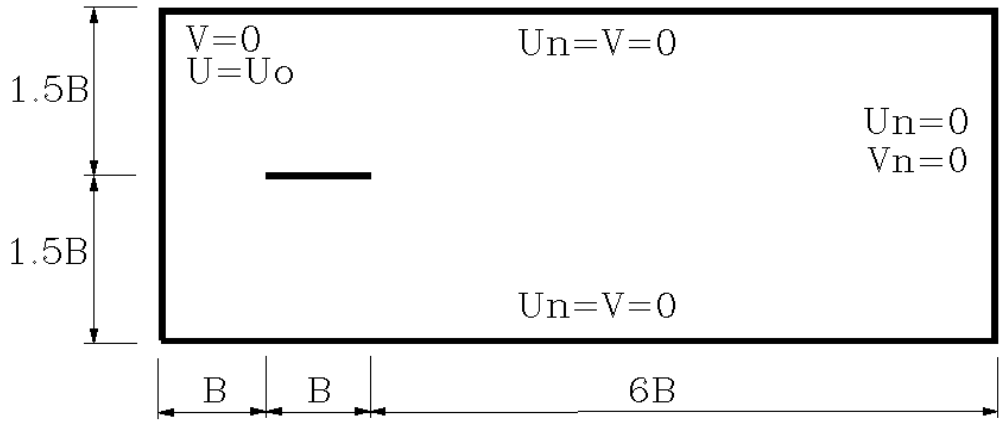

Fig 4.7 Solution domain and the Boundary conditions.

4.8 Finite Element Solution Procedure to solve the Fluid equations

The bridge section is subjected to the wind flow and the modeling is done as follows. The turbulence is modeled using Large Eddy Simulation (LES) and the governing equations are solved by Finite element method (FEM). The pressure on the bridge is computed by solving the Navier-Stokes equations and using this pressure the new position of the bridge is calculated by solving the structural mechanics equations. The flow is now solved over the new position of the structure and the grid is updated and the process is repeated for each time step. The time step size is calculated using a CFL (Courant-Frederick-Lewis) number less than one as reported by Selvam (1998). The Navier-Stokes equations are solved by Finite element procedure in a non-dimensional form. The

velocity and pressure are approximated using equal order interpolation. Eight noded brick element is used for 3D and four noded quadrilateral element is used for 2D.

The Navier-Stokes equations are solved using an implicit method suggested in Selvam (1998) in a four-step advancement scheme as follows:

Step 1: Solve for U_i from equation 5.3.

Step 2: Get new velocities as $U_i^* = U_i + \delta t(p,_i)$ where U_i is not specified

Step 3: Solve for pressure from $(p,_i),_i = U^*_{i,i} / \delta t$

Step 4: Correct the velocity for incompressibility: $U_i = U^*_i - \delta t(p,_i)$ where U_i is not specified

In step 1, the diffusion and higher order convection terms are considered implicitly to be in the current time and the first order convection terms are considered explicitly from the previous time step. Implicit treatment of the convective and diffusive terms eliminates the numerical stability restrictions. The pressure is considered in the right hand side of the equation. This set of equations leads to a symmetric matrix and the preconditioned conjugate gradient (PCG) procedure is used to solve. For simplicity here on $\frac{p}{\rho}$ is considered as p. Step 2 eliminates the checkerboard pressure field created when using equal order interpolation for velocity and pressure in the case of FEM.

The equations are stored in a compact form as discussed in Selvam (1998). To solve the velocities an under-relaxation factor of 0.7 is used. The iteration is done until the absolute sum of the residue of the equation reduces to $1x10^{-7}$ times the number of nodes for each time step. Usually the pressure and momentum equations take about 50 and 10 iterations for PCG solution respectively as reported by Selvam and Govindaswamy (2000).

4.9 Finite Element Scheme to solve the equations for Structure

Once the Navier-Stokes equations are solved, the pressure and velocity from the flow is obtained. This calculated pressure is applied as a force over the bridge section. The force along the x direction is the drag force (C_d), in y direction it is the lift force (C_l) and the force inducing a rotation is the moment (C_m). The results of the solution of fluid equations, in terms of the lift (C_d) and moment (C_m) coefficients along with the values of the non-dimensional velocity (U^*), R_I, R_m and whp are fed into the equations of motion for structure as given by (4.10) and (4.15). The resultant displacement in the form of heave (h) and pitch (α) is obtained by solving the non-dimensional form of the translatory and rotational equations of motion as given by 4.10 and 4.15 respectively. The bridge rotates about the shear center and moves vertically from the center of gravity. Since both these displacements occur along the line of symmetry, there is no coupling. The structural dynamics equations are solved in time explicitly using the central difference integration scheme. A constant time step size of 0.001 is used as against the variable time step size, used for the fixed computations. A time history of the data for these five variables, namely $C_d, C_l, C_m, h,$ and α are calculated and plotted.

4.10 Moving Grid

An arbitrary Lagrangian Eulerian (ALE) co-ordinate system is used for the description of both the structure and the fluid in the computational domain. Here the grid is moved according to the fluid structure interaction using the rigid body moving method. In this method, the grid is treated to be a rigid one during the flow and moved as a whole. The convective flux terms of the equations are modified in order to incorporate the

change in velocity of the moving elements. The correction is made by subtracting the velocity of the grid V_j from the velocity of the fluid U_j as shown by equation 4.4. The grid is treated as rigid and rotated as a whole about the shear center of the bridge section to match the corresponding structural deflections calculated during each time step. Thus the same grid is used for updating at each time in conformance with the flow.

The variables R_I, R_m, whp, U^*, and time step, as discussed in section 4.5 are given as input parameters in the moving bridge program and the response is plotted against time and the flutter velocity is calculated from these plots.

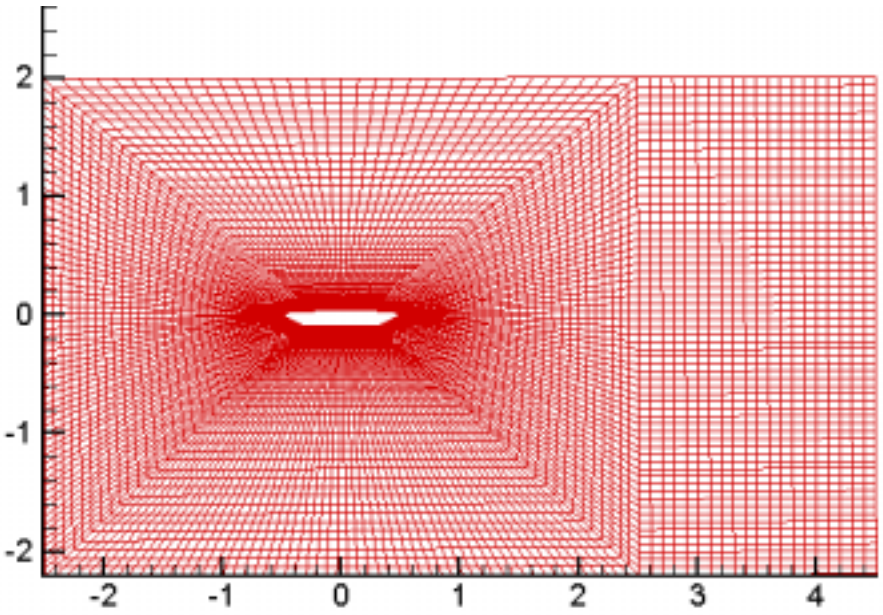

(a) Initial grid

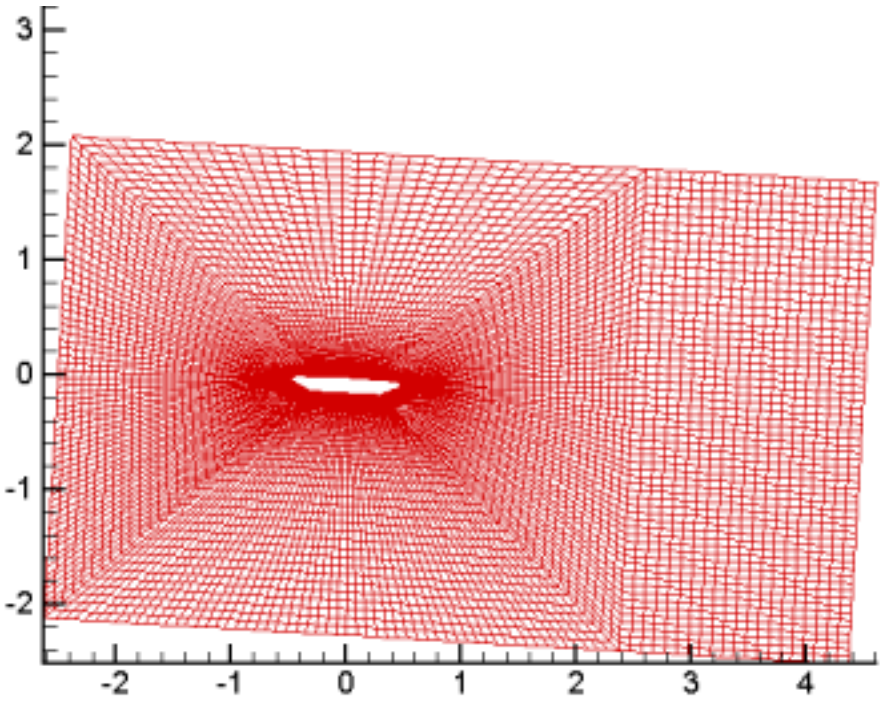

(b) Displaced grid

Fig 4.8 (a)-(b) Movement of grid using the rigid body method.

4.11 Critical Flutter Velocity computation for Bridges

The critical velocity for bridges is calculated using the free oscillation procedure. In the Free motion of the bridge, the aeroelastic stability is observed directly. Here the cross-section is elastically suspended in the flow and the stability of the cross-section is observed for various wind speeds. In this procedure the bridge cross-section is given an initial perturbation of 1.8° and the subsequent displacements on the structure in-terms of heave and pitch is observed. The pressure is computed for the given position of the bridge by solving the Navier-Stokes equations. The force along x direction represents drag, the y direction represents lift, and the force that causes rotation represents moment. This pressure force is then applied at the center of gravity and the moment force is applied at the shear

center and the non-dimensional structural dynamic equations are solved. The solution gives the heave and pitch displacements. The grid is now updated by applying these displacements in a rigid body fashion. The grid velocity to be applied is the difference in the position from one time step to the next divided by the time step size. This process is continued for several times steps. The grid velocity is then incorporated in the Navier stokes equations (equation 4.4) to account for the movement of grid. The plot of the bridge position in time for various approach wind speeds gives the detail of the aeroelastic stability. The model is run for various non-dimensional velocities ranging from 0.4 to 1.5 to study the stability of the bridge during motion. This initial perturbation dies down to zero and stabilizes as time progresses, if the velocity is less than the critical flutter velocity. As the models are run with increasing velocities, the flutter velocity is reached and the initial perturbation gradually increases in time till it reaches catastrophic levels before it fails. The critical flutter velocity may be calculated in a few computer runs from the time history plots of the motion-induced response from the structure. This is explained in detail in the chapter 6.

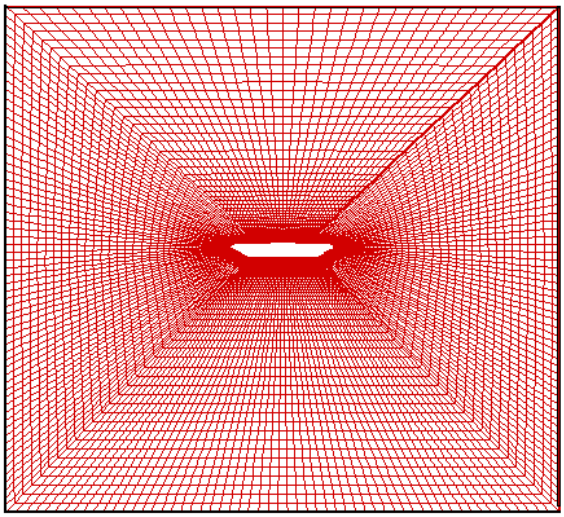

Fig 4.9 Grid-A

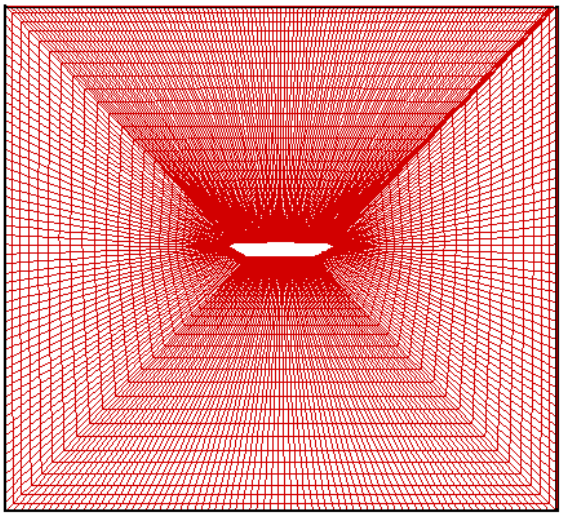

Fig 4.10 Grid-B

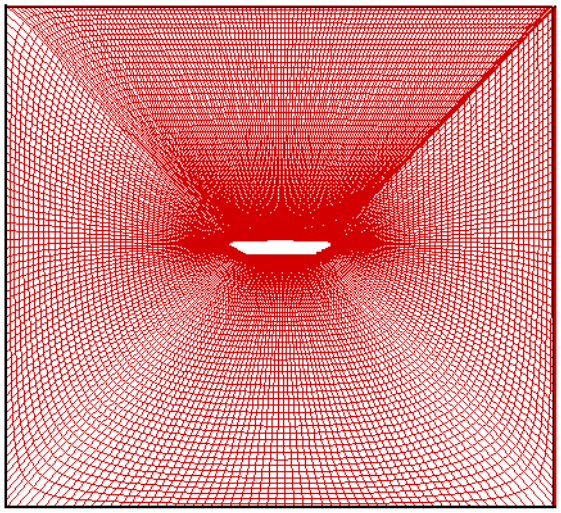

Fig 4.11 Grid-C

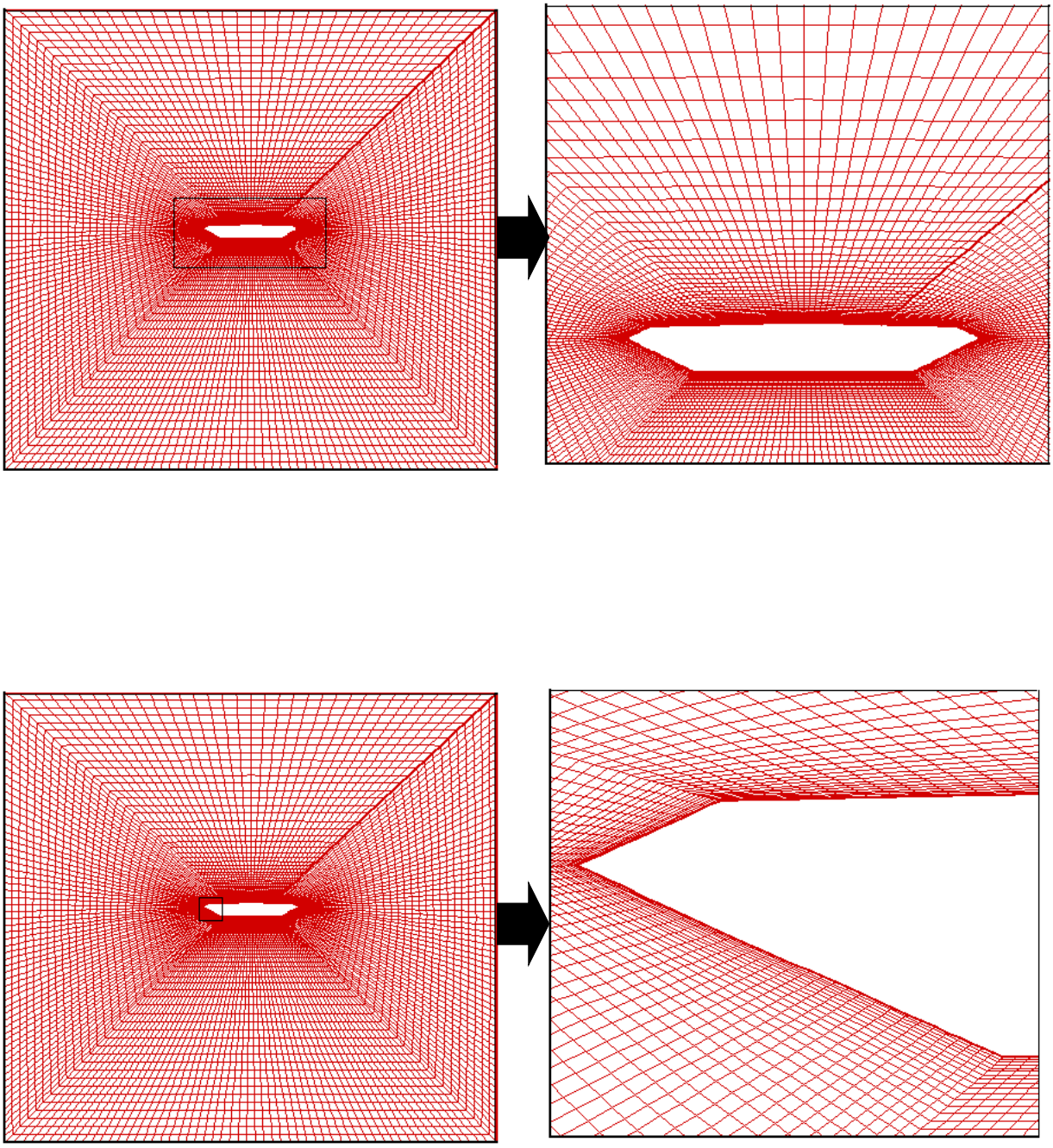

Fig 4.12 Close-up view of Grid-A

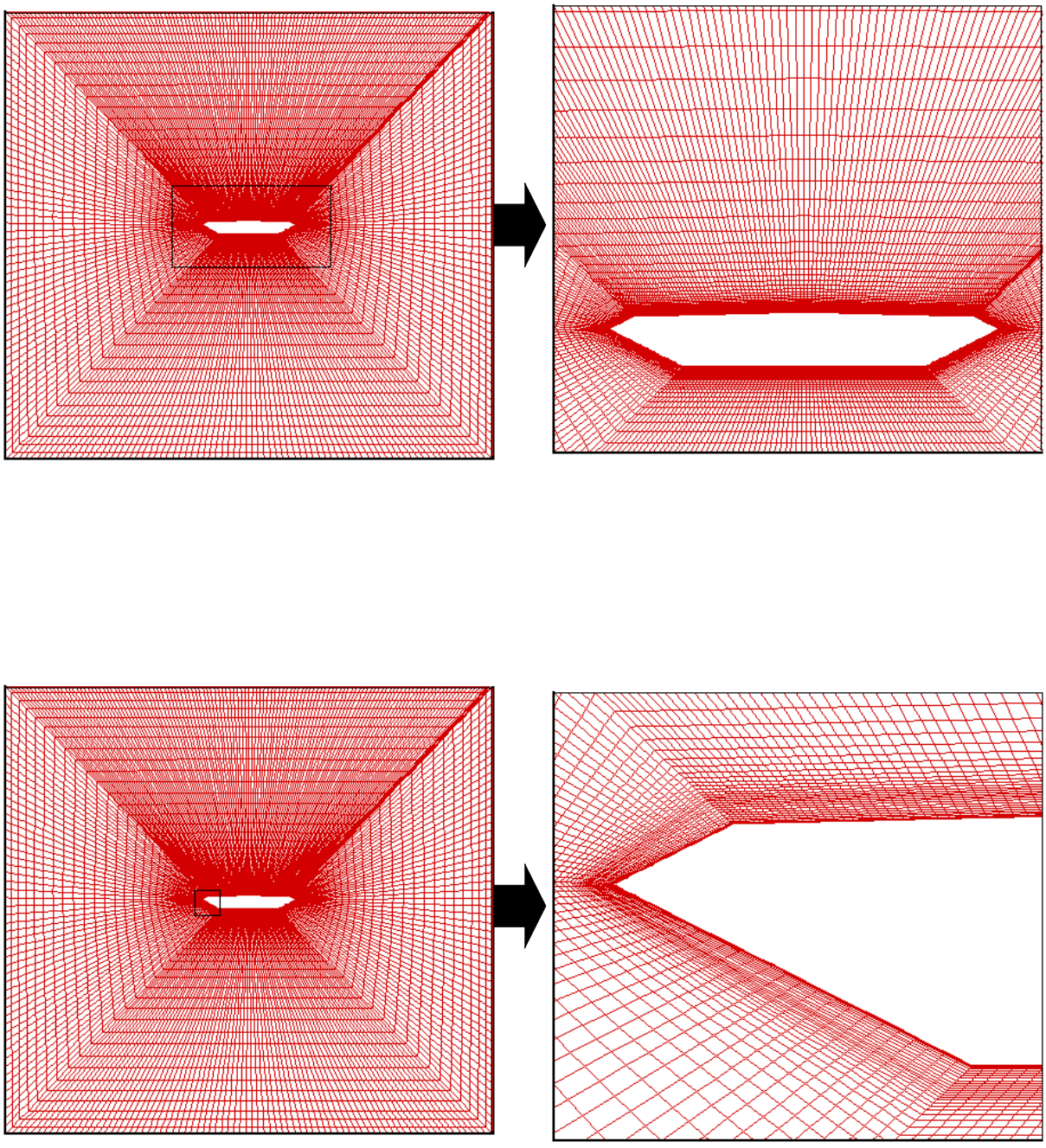

Fig 4.13 Close-up view of Grid-B

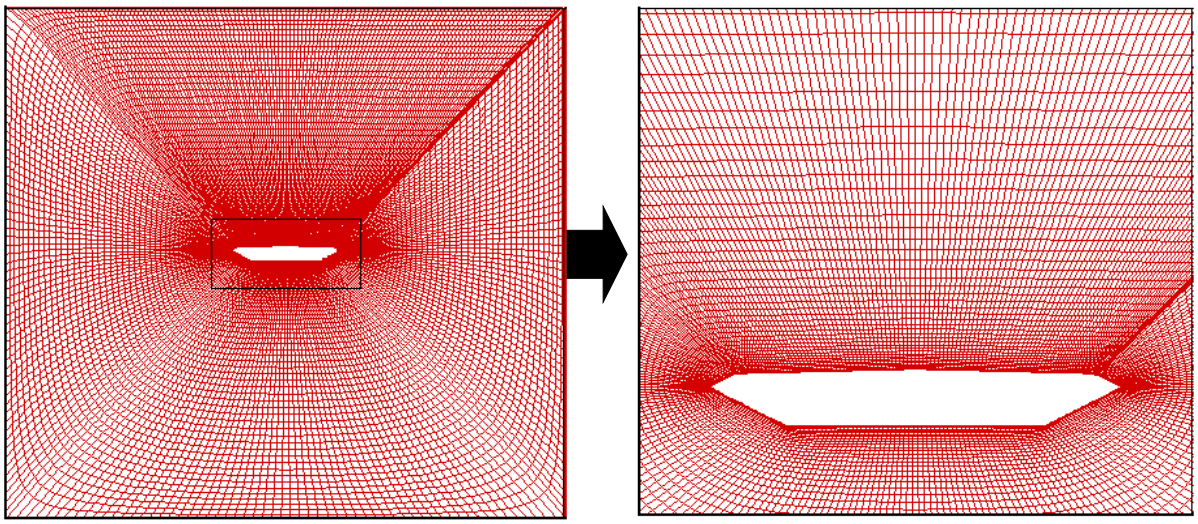

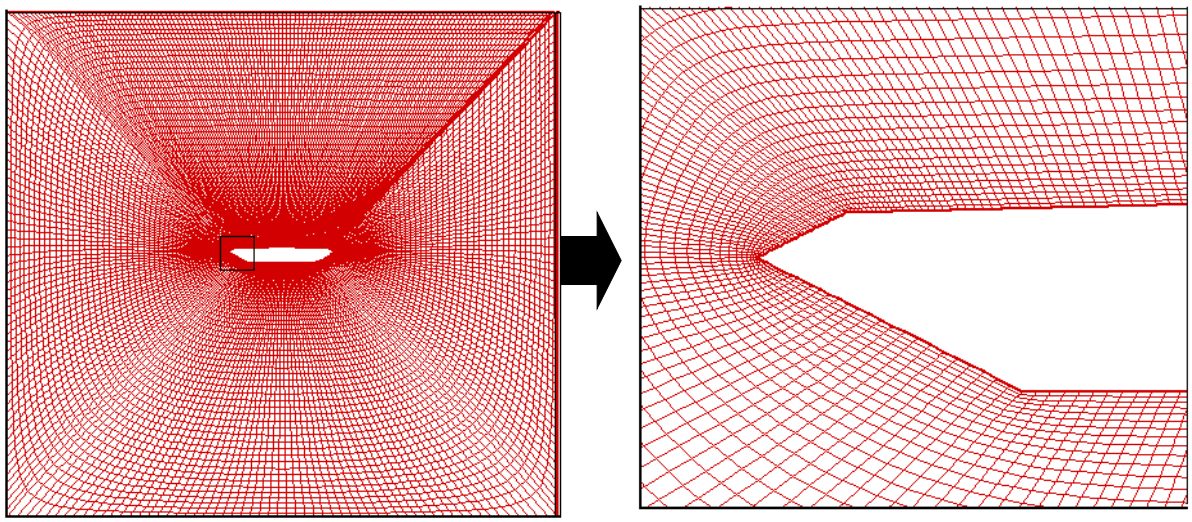

Fig 4.14 Close-up view of Grid-C

CHAPTER 5

GRID GENERATION

5.1 Introduction

The process of grid generation is the first and foremost step and is also the most vital part in the world of finite element/finite difference analysis. To solve a physical problem numerically the computational domain needs to be discretized into a collection of points or elemental volumes. This network of discrete points or volumes is called the grid. The governing partial differential equations are solved numerically upon these grid points to yield a solution over the domain. The most economical distribution of grid points requires that the grid be influenced by both the geometric configuration and by the physical solution being done thereon. The grid generation becomes a key issue because it is at the grid points in the mesh wherein, the desired parameters like pressure, stress, strain, or velocity based on the nature of the problem are calculated. So the disposition of the grid points in the model to a necessary and sufficient extent dictates the validity of the results in the computations.

Since resources are limited in any numerical solution, it is the function of the numerical grid generation to make the best use of the number of points that are available, and thus to make the grid points an active part of the numerical solution. In this chapter, the types of grid and the important issues in the grid generation will be discussed.

5.2 Types of Grid

There are basically two types of grids depending upon the method of generation. They are Structured Grid and Unstructured Grid.

5.2.1 Structured Grid

In a structured mesh, each interior nodal point is surrounded by exactly equal number of adjacent elements. We can identify two directions within the mesh by associating a coordinate system called ξ,η system or IJ (IJK incase of 3D) system with the mesh lines. The grid lines are the lines of constant ξ or lines of constant η. The node point (ξ,η) is formed with the intersection of grid lines ξ and η. If we number the nodes consecutively along lines of constant η, and so that the numbers increase as ξ increases, we can immediately identify the nearest neighbors of any node say, J on the mesh as shown in Fig 5.1. Typically quadrilateral or hexahedral elements are common in the structured type of meshes.

5.2.2 Unstructured Grid

The notable feature of an unstructured mesh is that the number of cells surrounding a typical interior node of the mesh is not necessarily constant. Thus the unstructured mesh generation relaxes the node valence requirement and allows any number of elements to meet at a single node unlike the structured mesh. Connections from point to point are listed, instead of using the IJK arrays, which structured grids use. The nodes and the elements are numbered and the number of nodes which belong to each element are stored (Fig 5.5). Triangle and tetrahedral meshes are most common when

referring to unstructured meshing, although quadrilateral and hexahedral meshes can also be unstructured.

5.3 Advantages and Disadvantages

A structured grid approach offers advantages in solution algorithm efficiency and implementation. This is particularly true in CFD, where a considerable technology base has been developed using solution algorithms for structured grids as reported by Peraire, Morgan, and Peiro (1990). These authors say that the structured grid offers choice of an appropriate solution method from among the large number of algorithms, which are available. The principal advantage of the unstructured approach is that it provides a powerful tool for discretizing domains of complex shape. But the disadvantages they mention are the limited availability of solution algorithms and the demand on the computer memory and CPU.

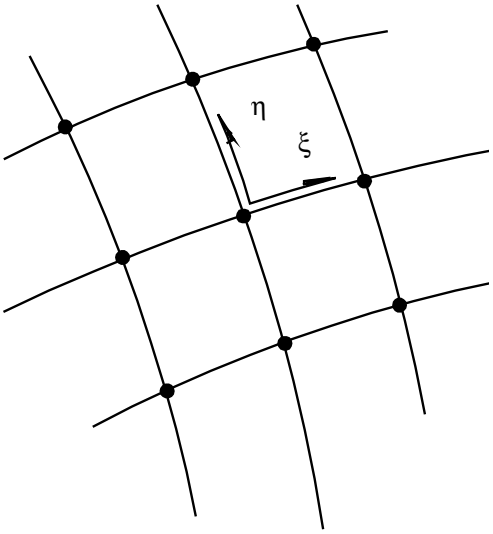

Fig 5.1 Structured mesh discretization

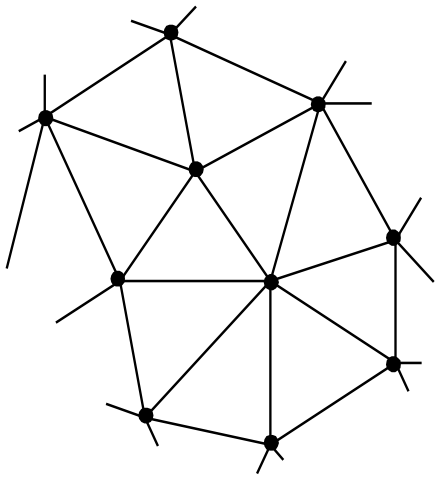

Fig 5.2 Unstructured mesh discretization

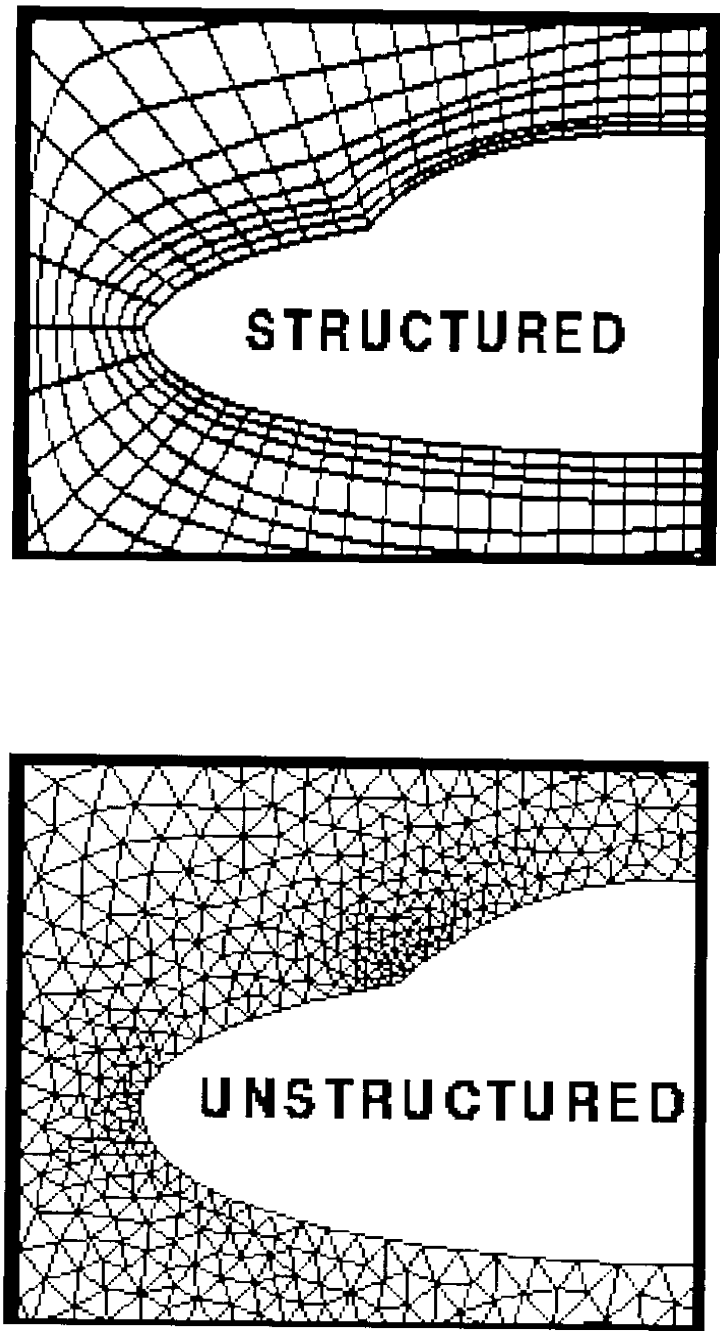

Fig 5.3 A picture from NASA research center showing the structured and unstructured grid around the nose of an aircraft.

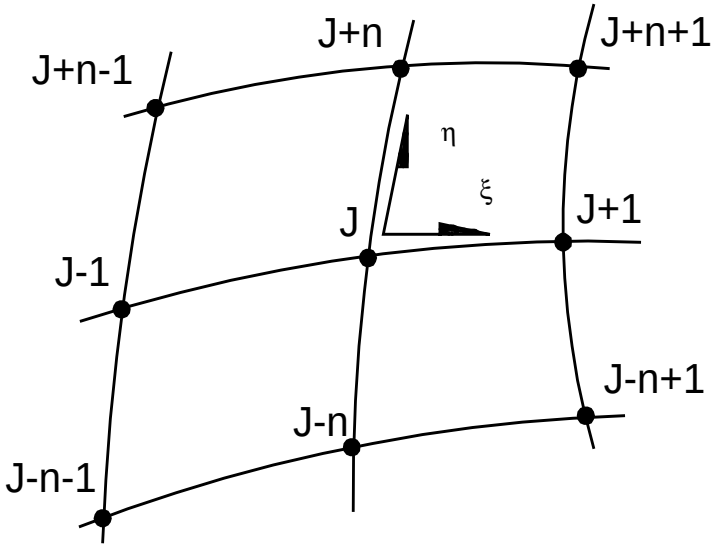

Fig 5.4 Organization of nodes in a structured mesh of n by m points in the ξ,η directions.

Element	Nodes		
1	5	8	9
2	9	8	12
3	8	7	12
4	6	7	8
5	5	6	8
6	5	9	10
7	11	5	10
8	3	5	11
9	3	4	5
10	1	4	3
11	4	6	5
12	1	6	4
13	1	2	6
14	2	7	6

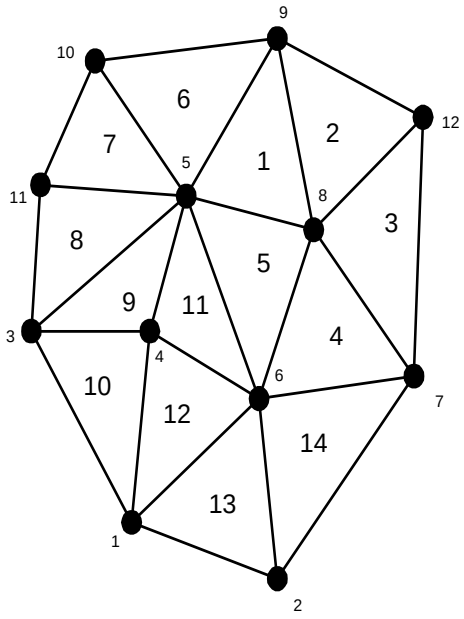

Fig 5.5 Connectivity array for an unstructured triangular mesh.

5.4 Issues in the grid generation process

The grid is a discrete representation of the continuous field phenomenon that is modeled and the accuracy and the numerical stability of the simulations depend on the choice of grid. In other words the density and distribution of the grid lines determines the accuracy with which the model represents the actual physical phenomena. That is why the grid generation has been a major challenge. There are certain issues that are to be borne in mind in the context of grid generation. They are listed below.

5.4.1 Number of grid points

The total number of grid points in the grid should be kept to the minimum needed to obtain solutions of the desired accuracy. This condition should be met for both structured and unstructured grids and is very significant for computational efficiency. This can be achieved by clustering grid points in the region of interest where they are most needed and reducing the concentration elsewhere. Where large gradients are expected, as in shear layers or mixing zones, the grid should be fine enough to minimize the change in the flow variables from node to node. If the grid points are not clustered in the regions where needed, solutions obtained may not have meaningful physics due to a low accuracy. The classical example is a boundary layer computation. If not enough grid points are used where a boundary layer is expected to occur, the boundary layer sometimes cannot be even seen. Currently, in the field of computational fluid dynamics, the grid points are often clustered near solid wall boundaries. If too many grid points are used overall, even currently well-advanced computers may not able to handle the computation at all due to a huge memory requirement. Thus, this condition is very

important. Hence several computational runs are made in this work by varying the number of grid cells and its associated parameters to find an optimum grid configuration for good results.

5.4.2 Body conformance

The grid should be boundary or body conforming. That is, one set of grid lines should always coincide with the physical boundary of the spatial domain regardless of the geometric complexity as reported by Choi (1997). He states that this rule is often met, although it is very difficult to generate a boundary conforming grid for a highly curved surface. The results vary enormously even when there is a slight variation in the proximity of the grid line with the wall of the bridge girder in this problem. As the wind flows, the nose of the bridge section separates the flow and shears it sharply, thereby letting the wind pass by, over its boundaries. Since the wind- flow process is very rapid and dynamic, especially in the close vicinity of the boundary, the manner of distribution of grid points, on and closer to the boundaries of the bridge section makes a significant difference on the resulting pattern of vortices and the coefficients. Therefore a highly dense and coherent grid is warranted over those important regions in order to capture the dynamic variation of lift and suction forces better, when compared to far off regions. The effect of the spacing parameter is discussed and the results are compared in chapter six.

5.4.3 Orthogonality of the grid cells

Grid lines that intersect a boundary should intersect that boundary perpendicularly so that derivative boundary conditions can be implemented more easily

and accurately. In some problems the temperature or velocity gradient normal to the wall surface is equal to zero. These boundary conditions can be easily implemented with a low error if the grid lines intersect a boundary orthogonally. At the interior of the spatial domain, the angle of intersection between grid lines only needs to be nearly orthogonal, but must be somewhere between 45 and 135 degrees as mentioned in the FLUENT software manual.

5.4.4 Grid spacing variation

In order to minimize a very large number of grid cells and at the same time, maintain a sufficient degree of accuracy in the solution, a non-uniform grid is used. In a non-uniform grid, the grid spacing is reduced in regions where high gradients are expected and increased in regions where the flow is relatively uniform. The spacing between grid points should change slowly from a region where grid points are concentrated to a region where grid points are sparsely distributed. That is, the rate of change of grid spacing should be minimized. Normally, the spacing between adjacent grid lines should not change by more than 20% or 30% from one grid line to the next as reported in FLUENT manual. This is an accuracy consideration, primarily impacting the accuracy of the diffusion terms in the governing fluid flow transport equations. This condition is important because otherwise, the numerical solution procedures in the computations may not be stable and robust and the solutions may start to diverge and blow off. Also the Fourier components, which make up the solution reflect and refract at interfaces where grid spacing changes as mentioned by Choi, 1997.

5.4.5 Cell Aspect Ratios

The aspect ratio of the computational cells is an additional issue that arises during the setup of the computational grid. While large aspect ratios may be acceptable in some problems, a general rule of thumb might be to avoid aspect ratios in excess of 5:1 (FLUENT manual). This limit can be acceptably exceeded when the gradients in one direction are very small relative to those in the second direction. Excessive aspect ratios can lead to stability problems, convergence difficulties, and/or the propagation of numerical errors and significantly increase the computational effort. Selvam (1994) evaluates the performance of various solution procedures in terms of the CPU (central processing unit, a measure of the computational time) and number of iterations for various aspect ratios of 1,10,60 and 160. From the paper it is found that as the aspect ratio increases there is a significant rise in the CPU time and number of iterations.

5.4.6 Grid Alignment

One set of grid lines should align with the flow direction (Choi, 1997). This condition is important for convection-dominated flows when the aspect ratio of the control volume about each grid point is very high and/or when the Navier-Stokes equations are used to study such flows. Here, the grid lines are aligned in the direction of the wind flow over the bridge girder.

5.4.7 Shape and size of the grid elements

The shape and size of the grid is very critical in light of the computations run using the finite element code. The grid element should be far as possible, have a reasonable aspect ratio closer to one. When the shape of the quadrilateral element is very

skew and slender and if the area of the grid cells (of the order of 10^{-7}) becomes very small, the Jacobian computations in the finite element formulation become very difficult. Also, at such skew elements, it necessitates very small time step, in the order of 0.0001seconds or so, for the integration of the fluid flow equations. This thereby increases the computational effort as the number of runs to be computed per second increases with lesser time step size. The size of the time step has an inverse relation with the computational effort. The lesser the time step size, the more the number of runs per second and hence more computational effort and CPU time and vice-versa. Therefore this aspect also becomes critical to be taken care of.

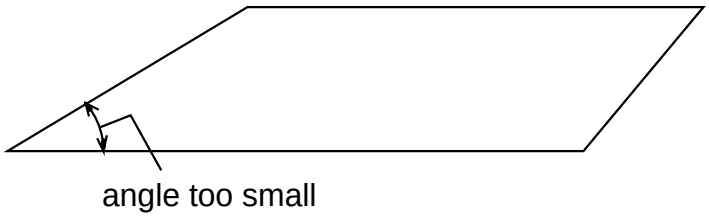

(a)

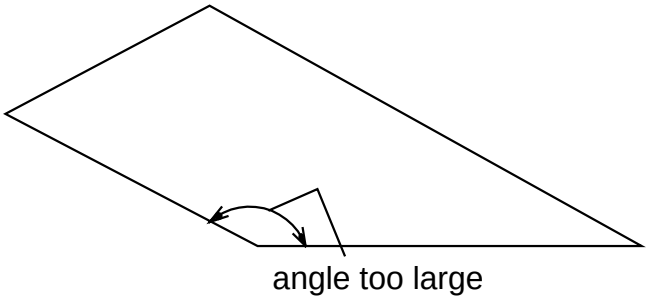

(b)

Fig 5.6 Undesirable Skew Elements in body fitted grid cells.

5.4.8 Numerical diffusion

A dominant source of errors in multi-dimensional situations is the so-called false diffusion or numerical diffusion. The term false diffusion is used because its effect is

analogous to that of increasing the real diffusion coefficient. False diffusion coefficient is noticeable only when the real diffusion is small, that is, when the situation is convection-dominated. The phenomenon of false diffusion arises due to one-dimensional interpolation practices being employed in a multi-dimensional situation. Therefore this source of error occurs when the flow is oblique to the grid lines and when there is a nonzero gradient of the dependent variable in the direction normal to the flow direction (FLUENT).

It is almost impossible to generate one single grid that would satisfy all of the conditions listed above at every part of the spatial domain. Therefore, one would need to generate several different single grids, each of which satisfies all of the above conditions at a different part of the spatial domain. According to the nature of the problem to be solved, the same grid is retained throughout the domain or these different individual grids are patched together to form a composite grid. Adaptive techniques are resorted to, wherever grid refinement is required locally. This is called adaptive meshing.

The configurations of grid used for the GBEB suspension span and the method of the generation is reported in chapter four.

CHAPTER 6

RESULTS

6.1 General Remarks

The analysis is performed for the bridge cross-section in two broad categories, fixed and moving. Different grids varying in terms of the number of elements, spacing and density are used in the computations. The effect of grid in the accuracy of the prediction of vortex-induced response and critical velocity computation is studied by running the models for different grids. Since the flow is very complicated and highly non-linear, the mathematical integration techniques and solution strategies used to solve the equations of structure and fluid are sensitive to errors. Even if a very small error is induced in the solution process, over several iterations of computation, the error gets carried over and grows in magnitude during each step in the time marching solution procedure and finally blows up to enormous magnitudes. The artificial viscosity or numerical diffusion when added to the fluid flow helps to have a better control of the numerical stability. But when it is more, the flow becomes diffusive and the results don't represent the actual behavior of the fluid. Hence several trials were made to find the lowest value of diffusion coefficient θ, as explained in section 5.4 that yields stable results. The coefficient of diffusion θ, is varied from 0.1 to 0.5 in the computations, with value of θ being similar to the first order upwind procedure in finite difference method.

All the computations were performed in Sun Microsystems Enterprise 4500 computer, with 8- 400MHz/4Mb external cache CPU modules and 4Gb-memory

expansion. The results of both the fixed and moving grid cases are tabulated and analyzed separately and compared with wind tunnel experimental results and also with other researchers. The pressure contours, vorticity and vector diagrams are plotted for the computational runs and compared. The plots of coefficients of drag, lift and moment against time are reported.

6.2 Fixed Grid

The bridge cross-section is assumed to be rigidly fixed and is restrained against any rotational or translational displacements. The model is run for different grid configurations and the results are reported in Table 6.1. The grid distribution 216 x 57 means, 216 points are located along the perimeter of the bridge cross-section and 57 points in the radial direction towards the boundary of the domain. The spacing is the distance between the closest grid line and the boundary wall of the girder cross-section. This spacing distance is non-dimensionalized with respect to the width (B=1) of the cross-section. Various initial spacing of 0.002B, 0.001B, 0.0033B, 0.00065B are used in different grid configurations.

The input for the fixed grid program is comprised of the number of nodes and elements, boundary conditions for elements along the boundary of the bridge cross-section and the wall of the domain, duration of time and the grid data. The duration of time is the amount of time during which the flow is simulated and it dictates the number of time steps to be executed. Based on the grid size, the time step size is calculated automatically using a Courant-Fredrick-Lewis (CFL) number less than one. For each time step, the output is written onto a data file with the values for the coefficient of drag (C_d)

and lift (C_l). These coefficients are plotted against time using the post processing software Tecplot. The C_d value is averaged out once the flow stabilizes after the initial disturbance. The Strouhal number is calculated from the plot of C_l against time using the following relation as explained in section 4.3 of chapter four.

$$S_t = \frac{H}{TV},$$

where T ⟶ period of oscillation of the lift forces

V ⟶ reference velocity,

H ⟶ height in the z direction of the bridge

Case	**Grid**	**Points**	**Nodes**	**Elements**	**Spacing**	**Cd**	**St**	θ
1	A	216 x 57	13515	13280	0.002	0.0590	0.191	0.3
2	A	,,	,,	,,	,,	0.0577	0.177	0.1
3	B	216 x 63	14805	14570	0.001	0.0618	0.167	0.3
4	B	,,	,,	,,	,,	0.0620	0.140	0.1
5	B	,,	,,	,,	,,	0.0485	-	0.5
6	C	302 x 65	20745	20424	0.0033	0.0524	0.193	0.3
7	D	312 x 57	18807	18476	0.00065	0.0586	0.209	0.3

Table 6.1 Summary of the runs in relation to various grid configurations.

Model by	Cd	St
This work (case- 4)	0.062	0.140
Larsen et. al.(1997)	0.061	0.100-0.168
Taylor et. al.(1999)	0.050	0.16-0.18
Wind Tunnel Tests	0.077	0.109-0.158

Table 6.2 Comparison of drag coefficient and Strouhal number obtained from numerical simulations and wind tunnel tests (Fixed case).

From the pressure contour diagrams shown in Fig 6.1 through 6.7, we can see the distribution of the pressure around the bridge girder section in the domain. The pressure contours vary according to the change in the density of the grid and the value of the diffusion coefficient. We can easily observe that the concentration of pressure at the nose of the bridge section at the front is much higher than any other place. Whereas the nose of the bridge at the wake is subjected to a suction or negative pressure. When the diffusion is more, the pressure contours along the body of the bridge is more uniformly distributed. This can be seen by the pressure contour diagrams with θ=0.3 being more uniform than with θ=0.1. Around the nose of the bridge, the pressure is more pronounced when θ= 0.3 than when θ=0.1. But when the diffusion θ is 0.5, the flow becomes diffusive and the pressure distribution is constant around the bridge as shown in Figure 6.5.

The build up of vortices above and below the deck and their transmission in the wake region is clearly seen in figures 6.11 and 6.14. From the vorticity diagrams it can be easily seen that when the diffusion coefficient θ=0.3, the vortices are more pronounced in the wake region as compared to when θ=0.1.

For the sake of experimentation, the grid B model was run with a diffusion coefficient of 0.5. From the result it was found that the flow was too diffusive and the pressure distribution was uniform all around the section but for the bridge. Also because of too much of diffusion there is no vortex formation though the grid is sufficiently dense and tight around the corners. Even the plot of drag and lift coefficients against time shows no variation and is constant throughout the simulation time. Hence the Strouhal number calculation was also not possible. Thus we can see the dominating influence of the diffusion coefficient over the flow characteristics.

It is observed that, when the grid is dense, i.e., spaced tightly close to the bridge deck, the vortex-shedding phenomenon is prominent. This is enunciated from grid B where the spacing is much close (0.001) as compared to grid A (0.002). Since the shear of wind occurs starting from the nose and along the wall of the bridge, a tight and dense grid is required to capture the details. But at the same time when the spacing is made very close it results in a heavy increase of elements resulting in increased computational effort. From the grids C and D, it is observed that though the spacing is much less as compared to grids A and B, there is not much improvement in the drag coefficient value. Hence grid B was chosen for further computations in fixed case and all of moving grid cases.

Frandsen and McRobie (1999) predicted a St of 0.11 – 0.28 for different mesh configurations ranging from 3438 elements to 16526 for a Reynolds number of 2.3×10^6. They report that the successful simulation of vortex shedding predictions was generally inaccurate and the models proved difficult at this time. Further studies by them are underway.

In this work, the computed results are in good comparison with wind tunnel results.

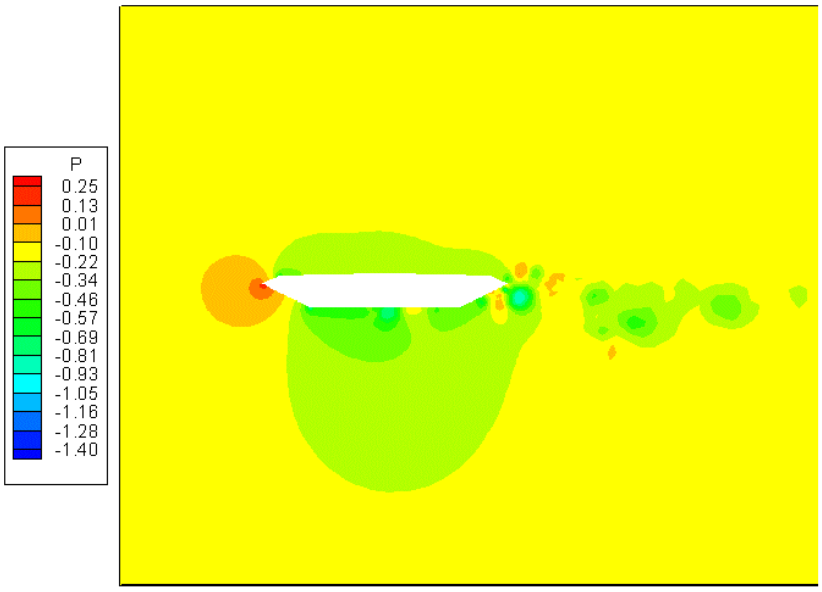

Figure 6.1 Pressure Contour for grid A with θ = 0.3 (Fixed Case)

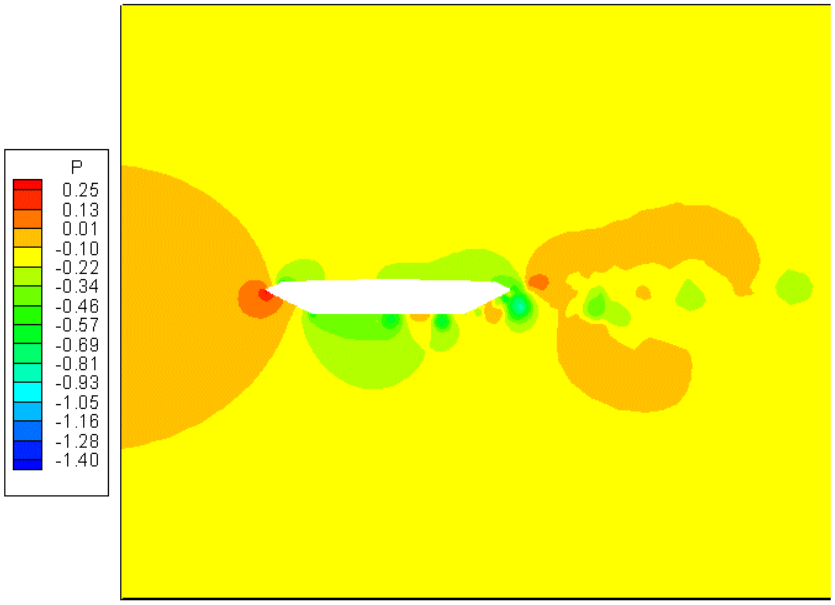

Figure 6.2 Pressure Contour for grid A with θ = 0.1 (Fixed Case)

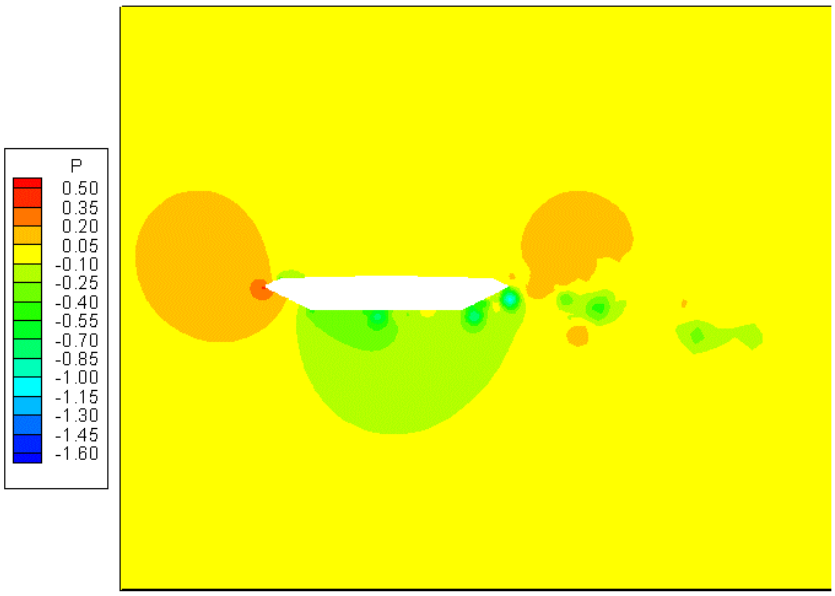

Figure 6.3 Pressure Contour for grid B with θ = 0.3 (Fixed Case)

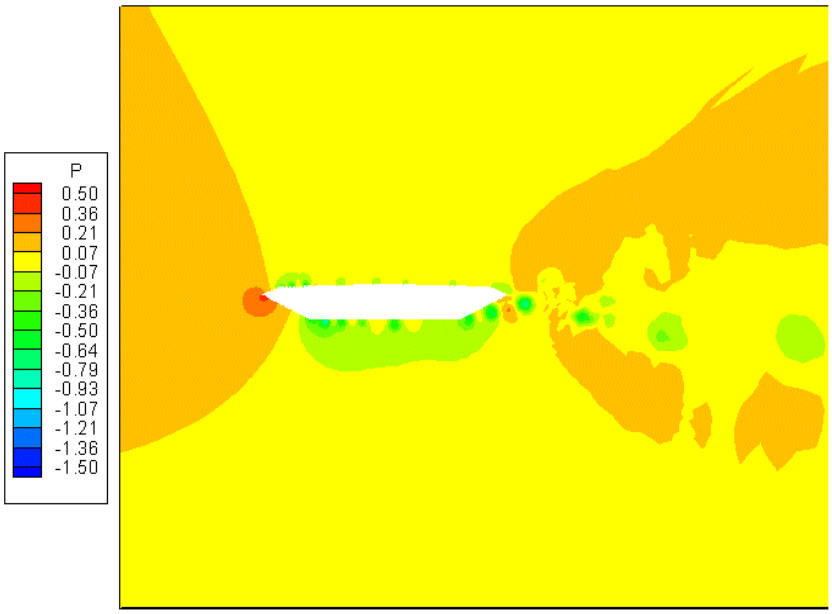

Figure 6.4 Pressure Contour for grid B with θ = 0.1 (Fixed Case)

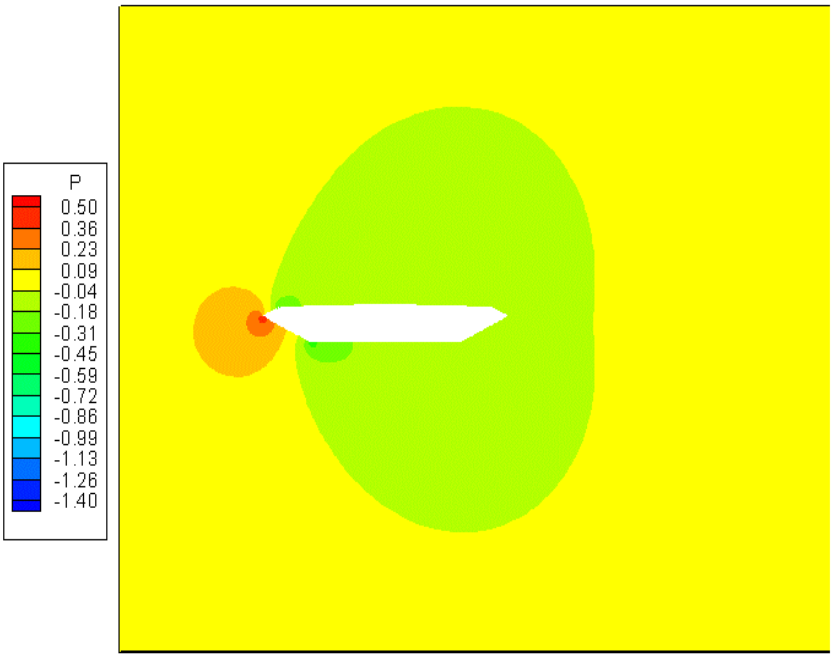

Figure 6.5 Pressure Contour for grid B with θ = 0.5 (Fixed Case)

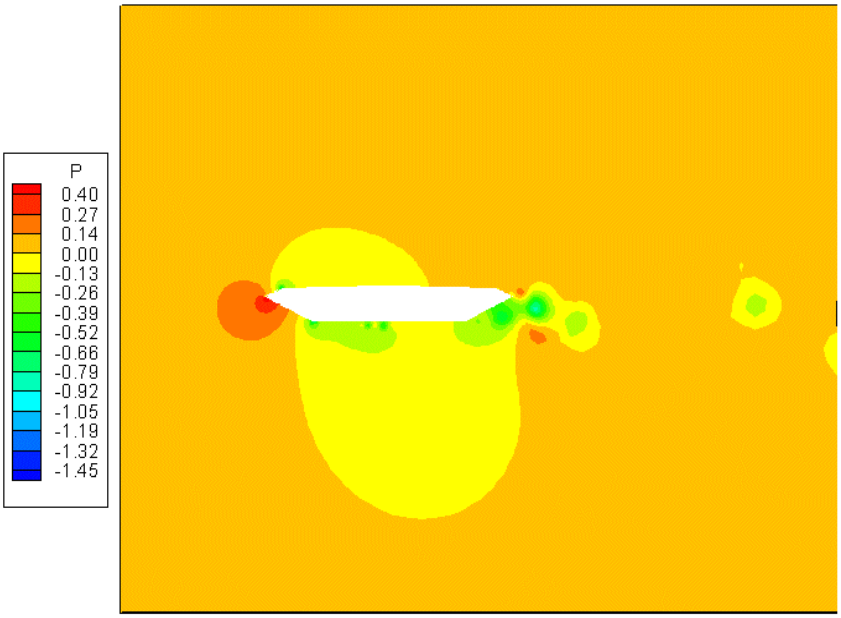

Figure 6.6 Pressure Contour for grid C with θ = 0.3 (Fixed Case)

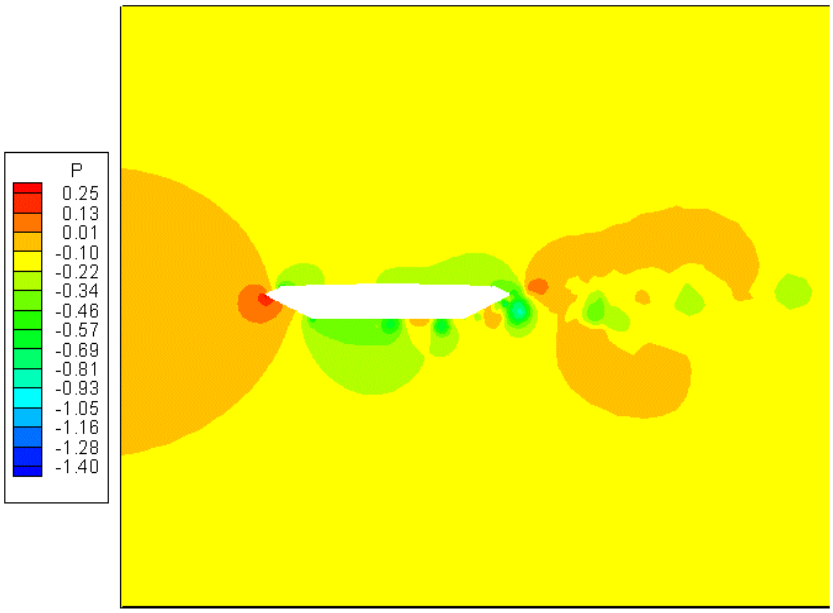

Figure 6.7 Pressure Contour for grid D with θ = 0.3 (Fixed Case)

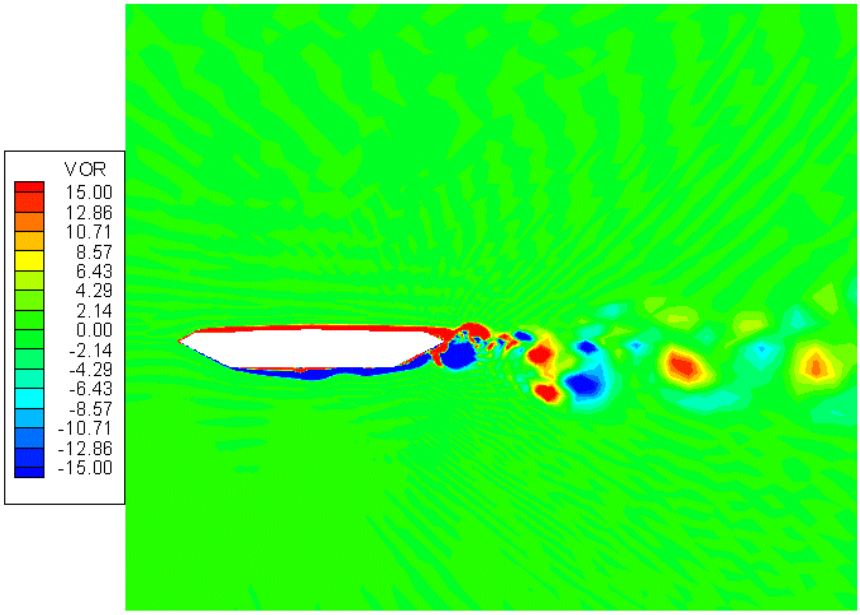

Figure 6.8 Vorticity Plot for grid A with θ = 0.3 (Fixed Case)

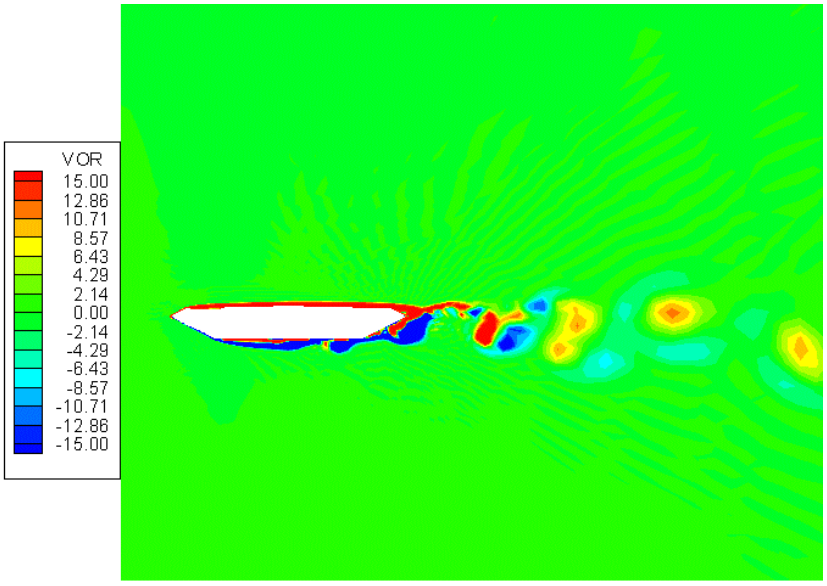

Figure 6.9 Vorticity Plot for grid A with θ = 0.1 (Fixed Case)

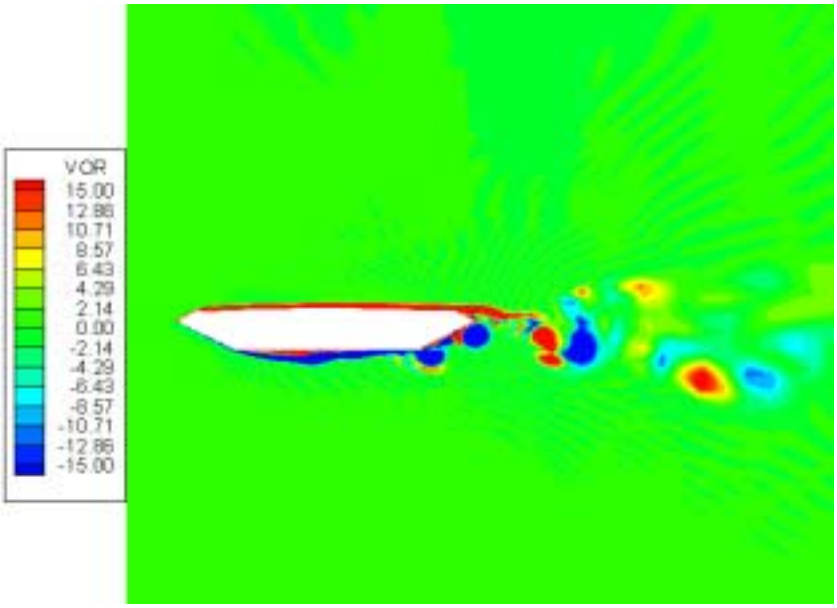

Figure 6.10 Vorticity Plot for grid B with θ = 0.3 (Fixed Case)

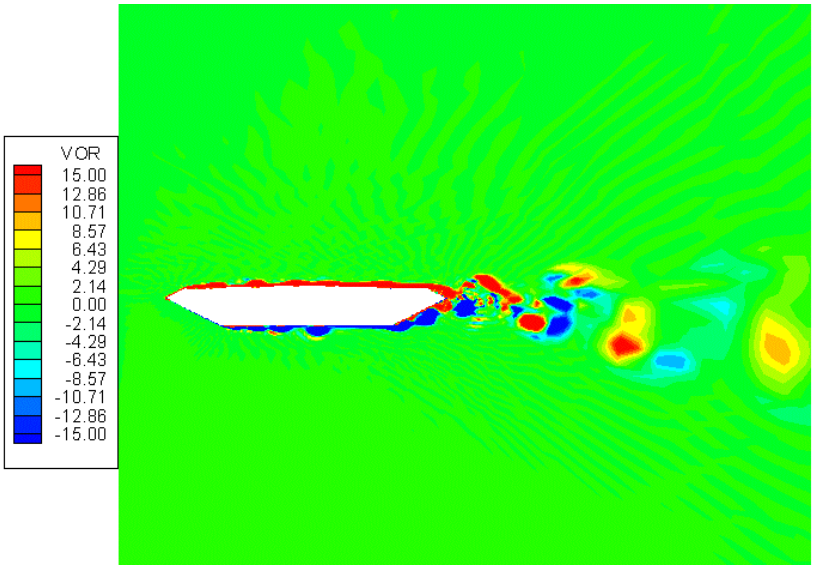

Figure 6.11 Vorticity Plot for grid B with θ = 0.1 (Fixed Case)

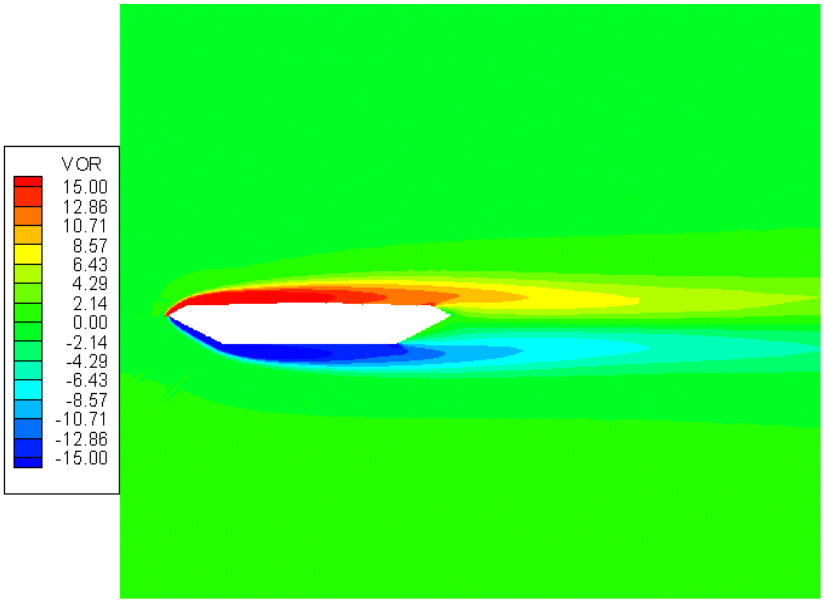

Figure 6.12 Vorticity Plot for grid B with θ = 0.5 (Fixed Case)

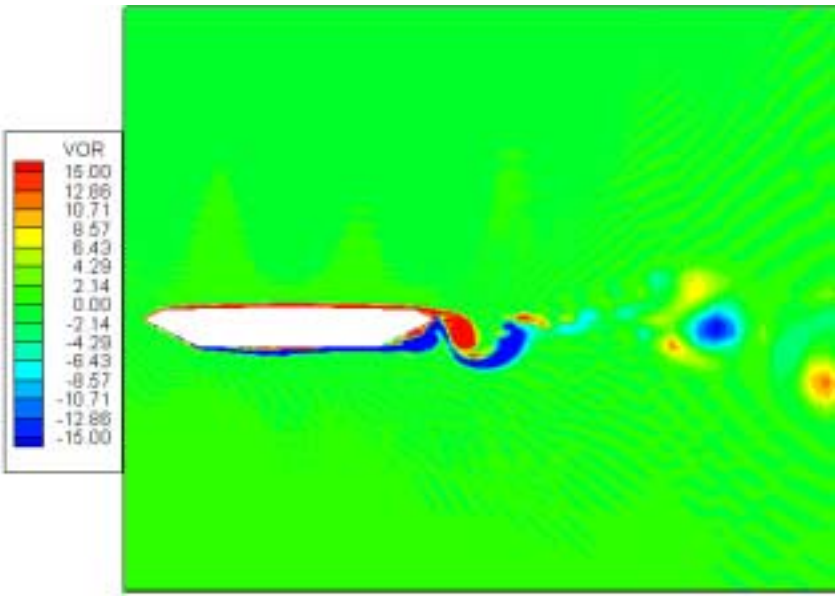

Figure 6.13 Vorticity Plot for grid C with θ = 0.3 (Fixed Case)

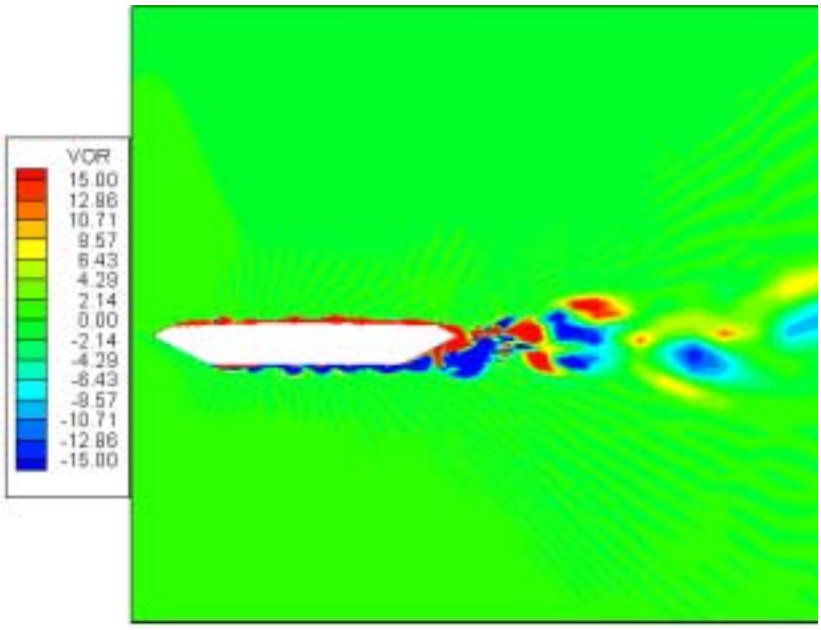

Figure 6.14 Vorticity Plot for grid D with θ = 0.3 (Fixed Case)

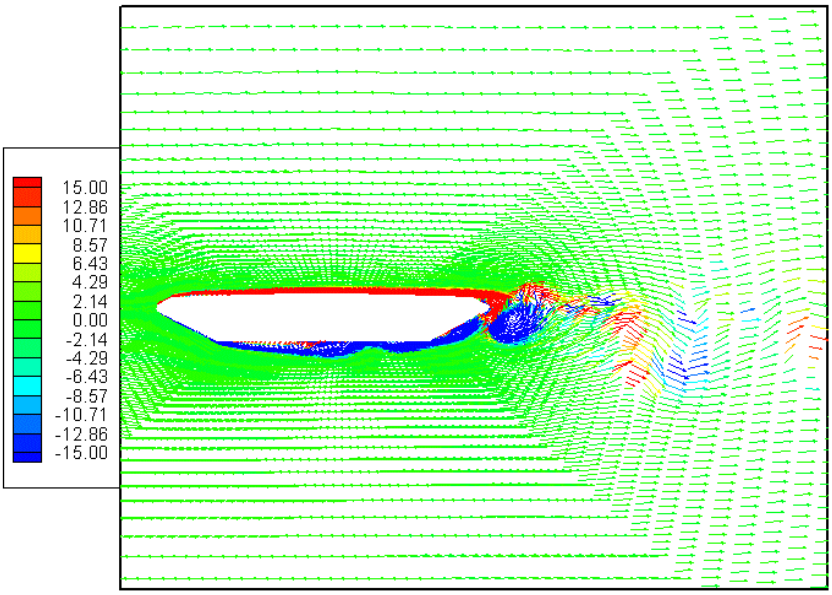

Figure 6.15 Vector Plot for grid A with $\theta = 0.3$ (Fixed Case)

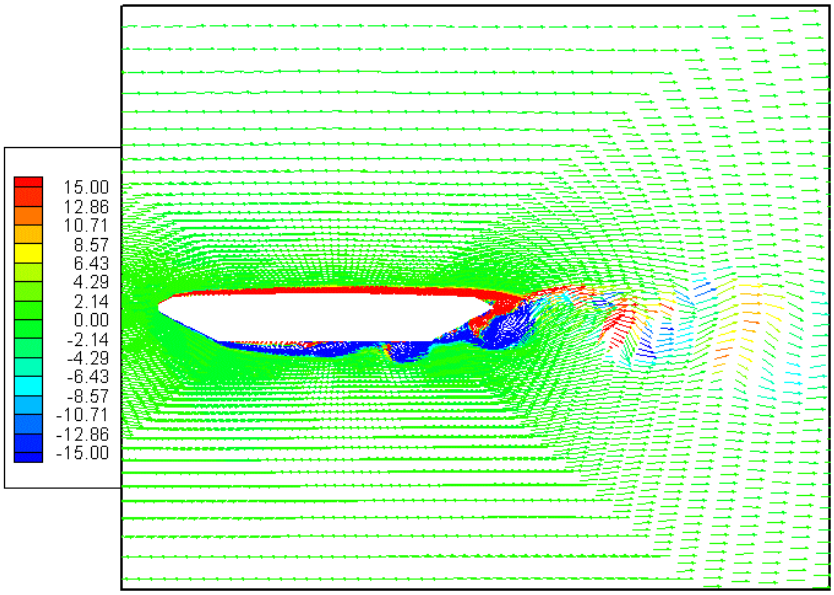

Figure 6.16 Vector Plot for grid A with $\theta = 0.1$ (Fixed Case)

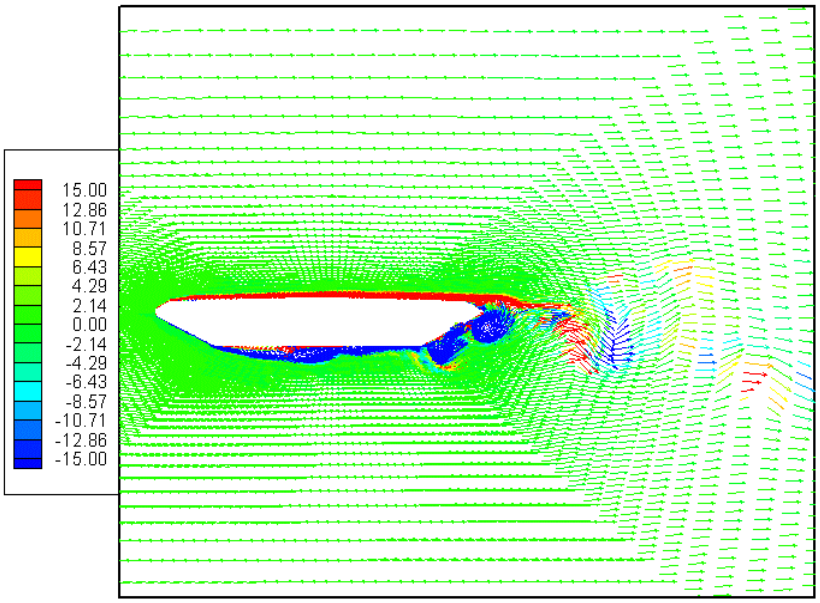

Figure 6.17 Vector Plot for grid B with $\theta = 0.3$ (Fixed Case)

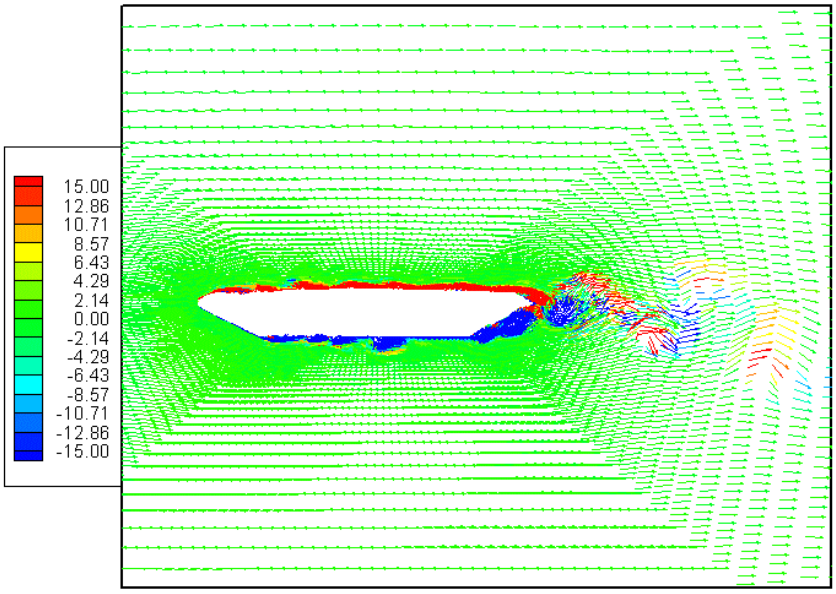

Figure 6.18 Vector Plot for grid B with $\theta = 0.1$ (Fixed Case)

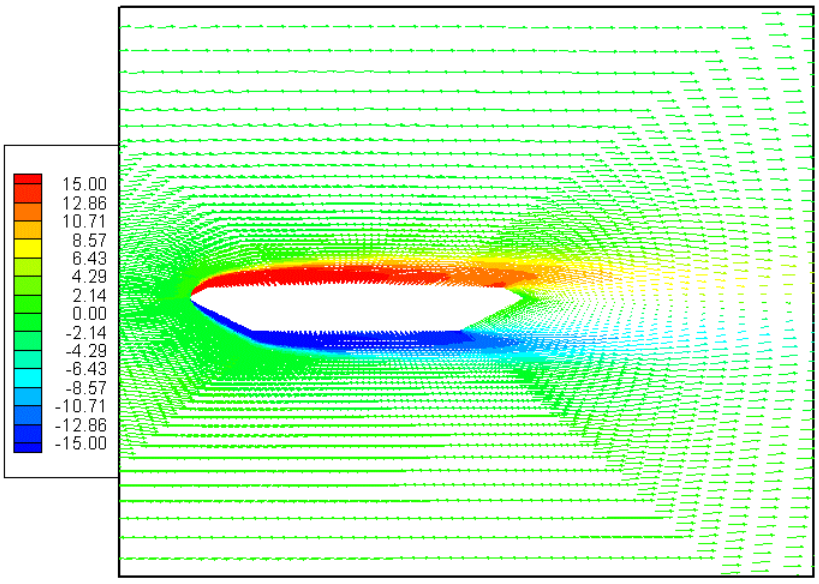

Figure 6.19 Vector Plot for grid B with θ = 0.5 (Fixed Case)

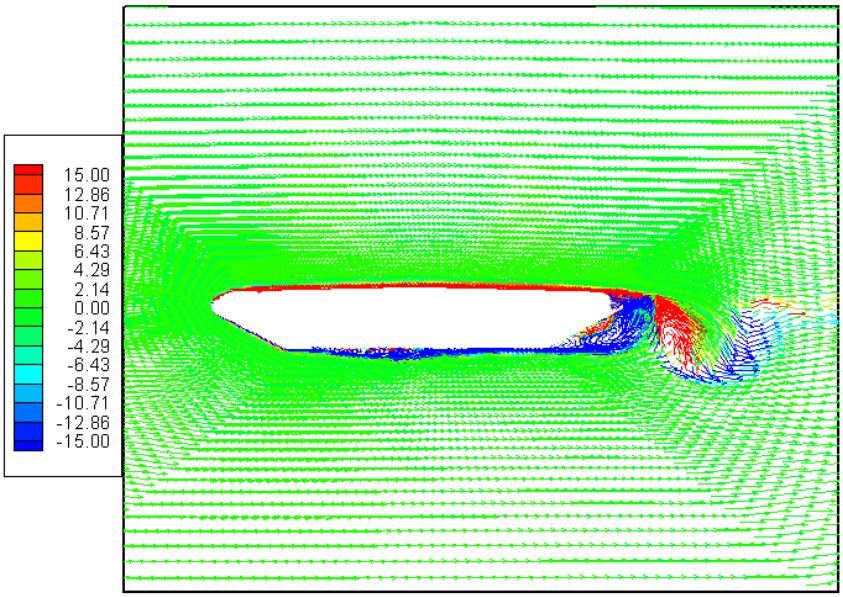

Figure 6.20 Vector Plot for grid C with θ = 0.3 (Fixed Case)

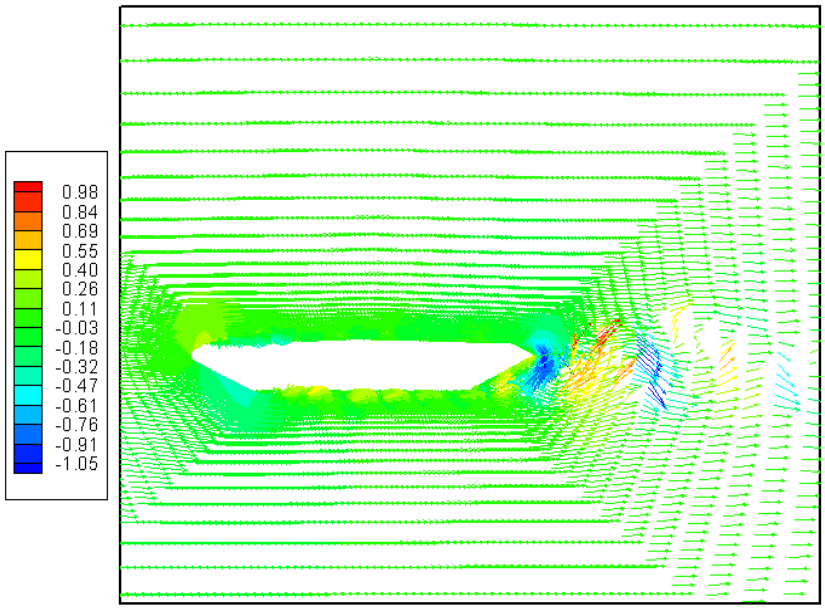

Figure 6.21 Vector Plot for grid D with θ = 0.3 (Fixed Case)

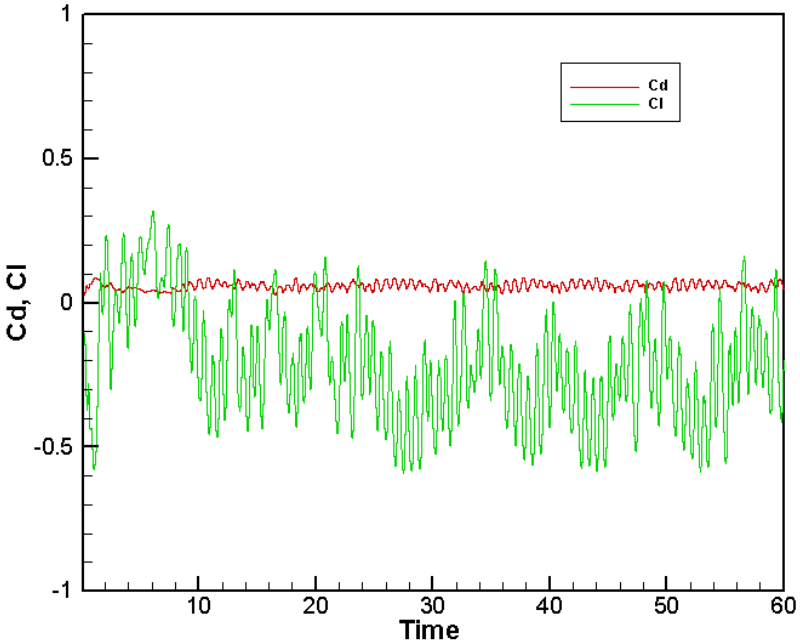

Figure 6.22 Drag and Lift coefficients Vs Time for grid A with θ =0.3 (Fixed Case)

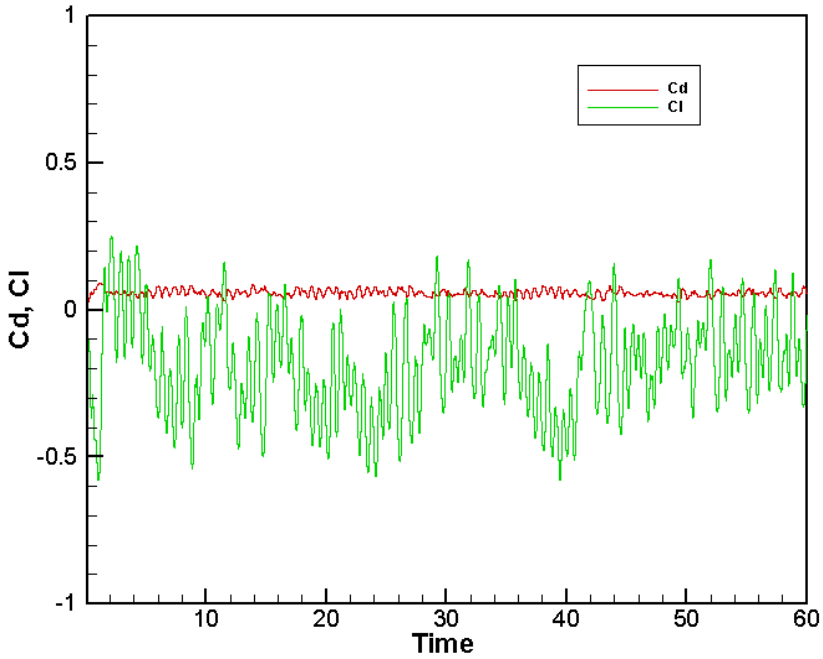

Figure 6.23 Drag and Lift coefficients Vs Time for grid A with θ = 0.1 (Fixed Case)

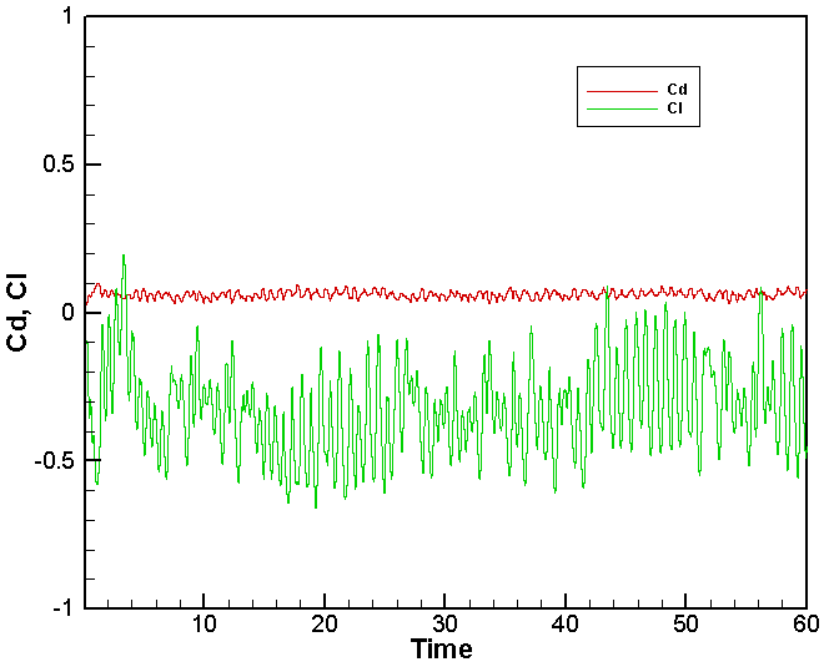

Figure 6.24 Drag and Lift coefficients Vs Time for grid B with θ = 0.3 (Fixed Case)

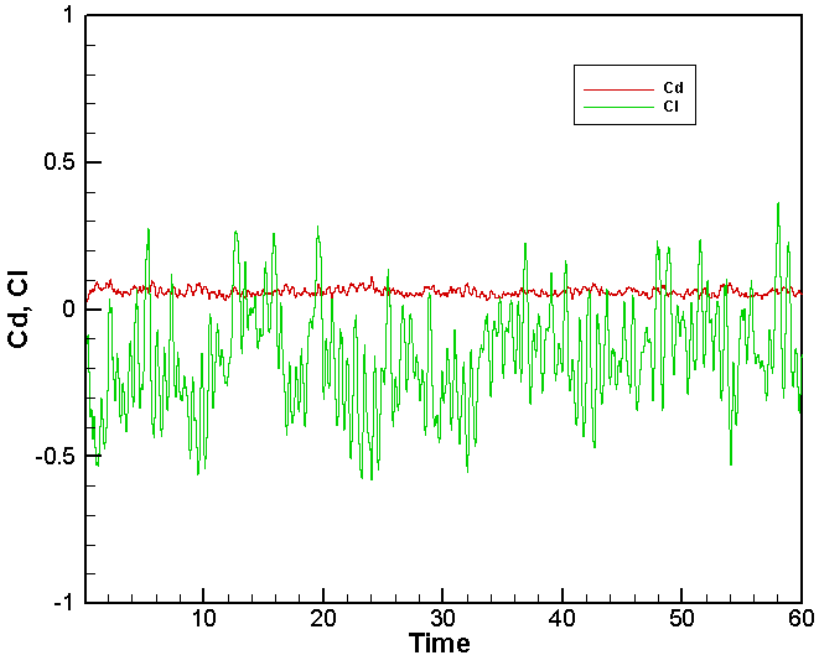

Figure 6.25 Drag and Lift coefficients Vs Time for grid B with θ = 0.1 (Fixed Case)

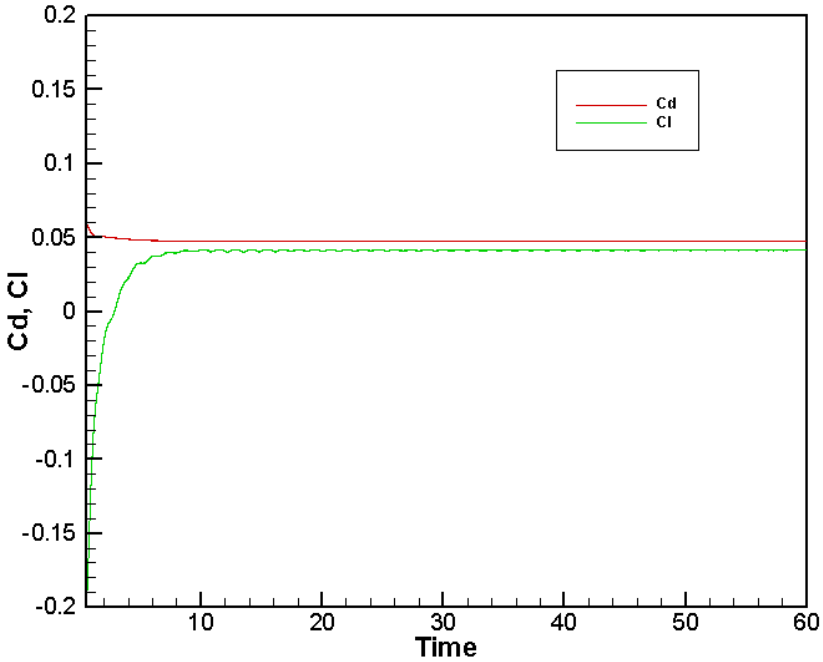

Figure 6.26 Drag and Lift coefficients Vs Time for grid B with θ = 0.5 (Fixed Case)

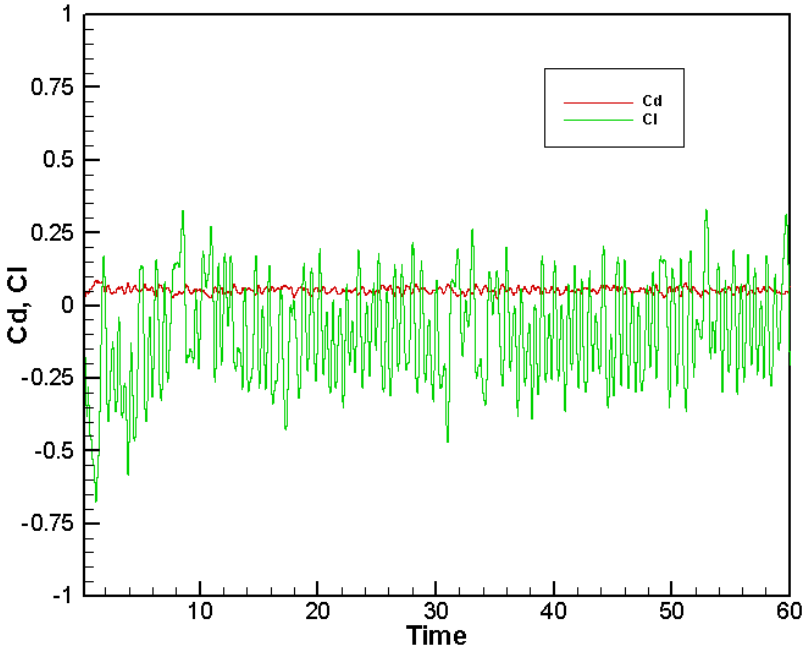

Figure 6.27 Drag and Lift coefficients Vs Time for grid C with θ = 0.3 (Fixed Case)

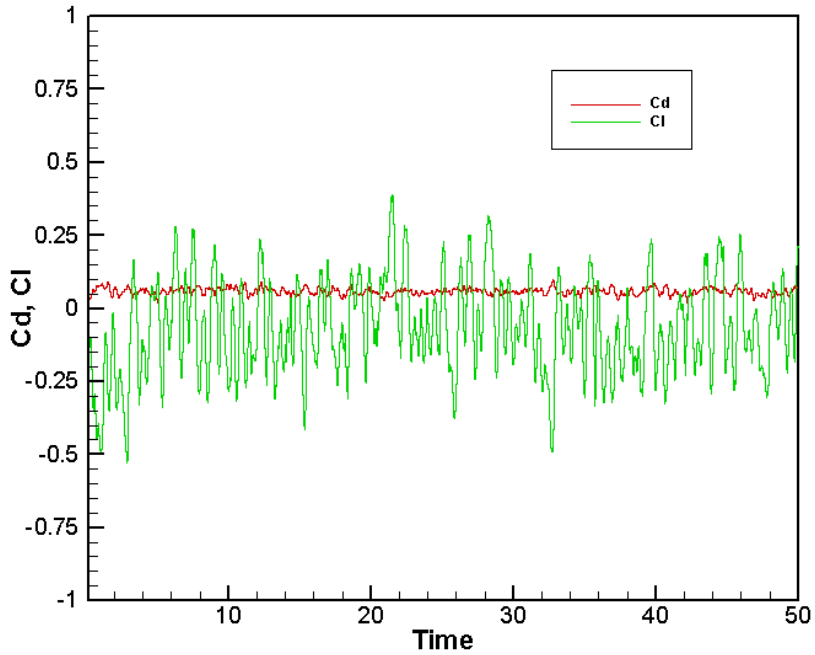

Figure 6.28 Drag and Lift coefficients Vs Time for grid D with θ = 0.3 (Fixed Case)

6.3 Moving grid

In this part of the analysis, the bridge section is moved according to the interaction between the fluid flow and the structure. The bridge section is allowed to rotate about the shear center and this motion is known as pitching. The vertical motion referred to as the translational or heaving motion occurs along the center of gravity. Both these motions occur in an uncoupled fashion due to the symmetrical location of the axis of shear and center of gravity.

The input for the moving grid program comprises additional parameters apart from the fixed program which includes R_I, R_m, U , whp and dt. These terms are defined in section 4.5 of chapter 4. Here $R_I = \frac{I_\alpha}{\rho B^4}$=2.178, $R_m = \frac{M}{\rho D^2}$=19.236 and $whp = \frac{\omega_h}{\omega_\alpha}$=0.364 for all the cases involving the moving grids. The reduced velocity value U is varied from 0.4 to 1.4 to examine the conditions of flutter and no flutter. The time step size dt is determined from the time step size of the last time step of the fixed program rounded up to the nearest 1000^{th}. In the moving grid computations the time step is kept as 0.001, which means 1000 iterations are performed for a single unit of time. This explains the intensive computational effort involved in the calculations. The velocity profile of the grid system from the fixed program is fed as an additional input file for the moving program. This helps in reducing the time taken for the bridge to react to the flow and stabilize. The program is run for a duration of 100 seconds and the initial perturbation is monitored to check for a rise or fall to assess the flutter condition. All the

computations are carried out for the moving program using the grid B, since it is found to be the optimum grid in terms of computational time, stability and grid size.

The output parameters of the moving bridge program are the same as those for the fixed program except for the addition of pitch and heave displacements. At each time step, the values are written onto an output file. The values of C_d, C_l, C_m, heave and pitch are plotted against time. The critical velocity for the onset of flutter is determined from the plot of the pitch angle versus time. This plot gives a clear idea of whether the deflection is decreasing or increasing in magnitude. When the velocity is below the critical velocity for flutter, the initial perturbation gradually dies down. Once the velocity exceeds the critical flutter velocity, the deflection increases constantly until failure. This growing up or dying down of deflection is easily observed in Figures 6.34 through 6.39. The nature of deflection with increasing and decreasing levels as seen in Figures 6.36 and 6.38 is just as observed in wind tunnel tests with section models when the wind velocity is well below the critical flutter wind velocity. It is observed that the mean displacement and angular rotation as well as the vibration amplitudes increase with wind velocity. It is found that the torsional mode is more important than the vertical heave mode because the instability induced by the former causes high stress levels resulting in failure much earlier than the latter.

The aerodynamic damping is positive as long as the pitch angle decreases in time and vice-versa. The plot of the angle versus time is analyzed to study the extent of growth or decay. The rate of growth and decay is found by averaging the change in amplitude values of the last two periods of the pitch angle vs. time plot. These rates are plotted for each U value as shown in figure 6.29 and the point where the plot crosses the zero

decay/growth line (x-axis) is found. This point represents the critical value of U for the onset of flutter. Figures 6.30 through 6.35 shows the examples of negative and positive aerodynamic damping for different cases of θ.

The results of the moving grid case are given below and the conditions of flutter and no flutter are reported as follows.

The velocity for critical flutter from the graph is reported as follows for the following cases.

U =1.22 for θ=0.3

U =1.27 for θ=0.1

U =1.30 for $\theta = dt$

It is noted that the critical flutter velocity seems to increase when the θ becomes lesser from 0.3 to dt. This is an interesting inference. This means, the lesser the diffusion coefficient from 0.3 to dt, it implies that the Reynolds number is apparently greater, thereby making the flow smoother and thus increasing the stability. We can see that the flutter starts occurring at U =1.22 in the case of θ=0.3, whereas it only starts fluttering at U =1.30 for $\theta = dt$. Thus the bridge sustains itself much longer and the critical limit for flutter is higher for lower θ.

The correct choice of the diffusion coefficient also determines the accuracy of the prediction of the critical flutter velocity apart from the numerical issues. The range of 65-72 m/s for critical flutter velocity is based upon the diffusion coefficient range of 0.1 – 0.3 including the time step value of dt.

To study the influence of the grid over the critical flutter velocity, the moving bridge model was run on a coarse grid of size 2100 elements. It was found that the flutter

didn't reach until U =1.35. This maybe attributed to the lack of refinement and lower density of the grid cells around the bridge section.

From the non-dimensional velocity U, the actual velocity is calculated as follows.

$$V_{\infty} = U\omega_{\alpha}B$$

For U =1.22

V_{∞} =(1.30) [(2π)(0.272)rad/s] (31m)

=64.6 m/s ~ 65 m/s

For U =1.35

V_{∞} =(1.35) [(2π)(0.272)rad/s] (31m)

=71.5 m/s ~ 72 m/s

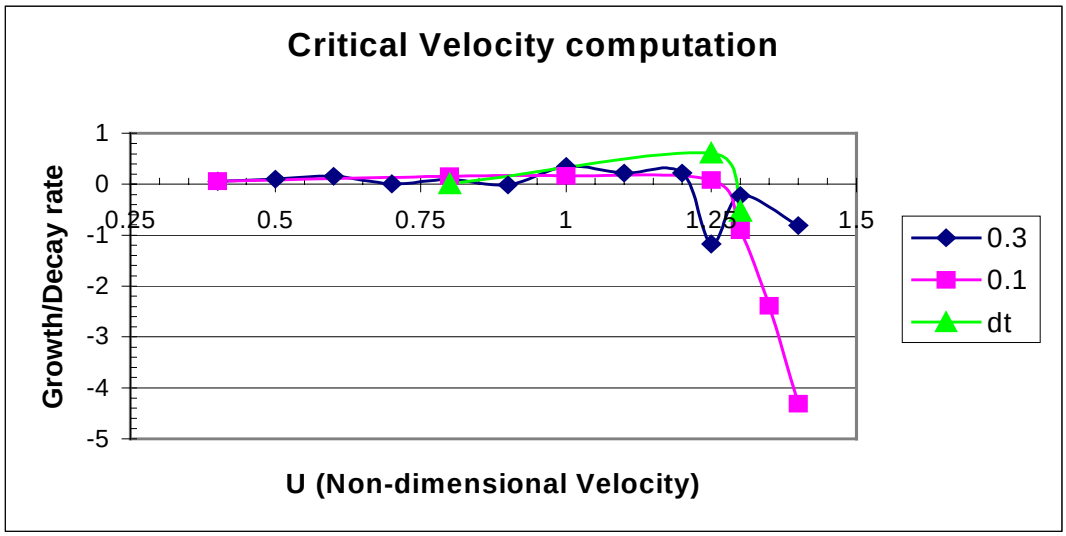

Figure 6.29. Plot of U Vs. Growth/Decay rate showing the critical velocity computation.

Once the flutter is initiated, the bridge undergoes enormous deflections until it finally fails as shown in the Figures 6.30 through 6.33. The deflections shown in Figures 6.32 and 6.33 are more than 40 and 90, which cannot exist in reality, because the deflections are so enormous that it actually fails much before than that. But since this is a computer model we can visualize such enormous deflections.

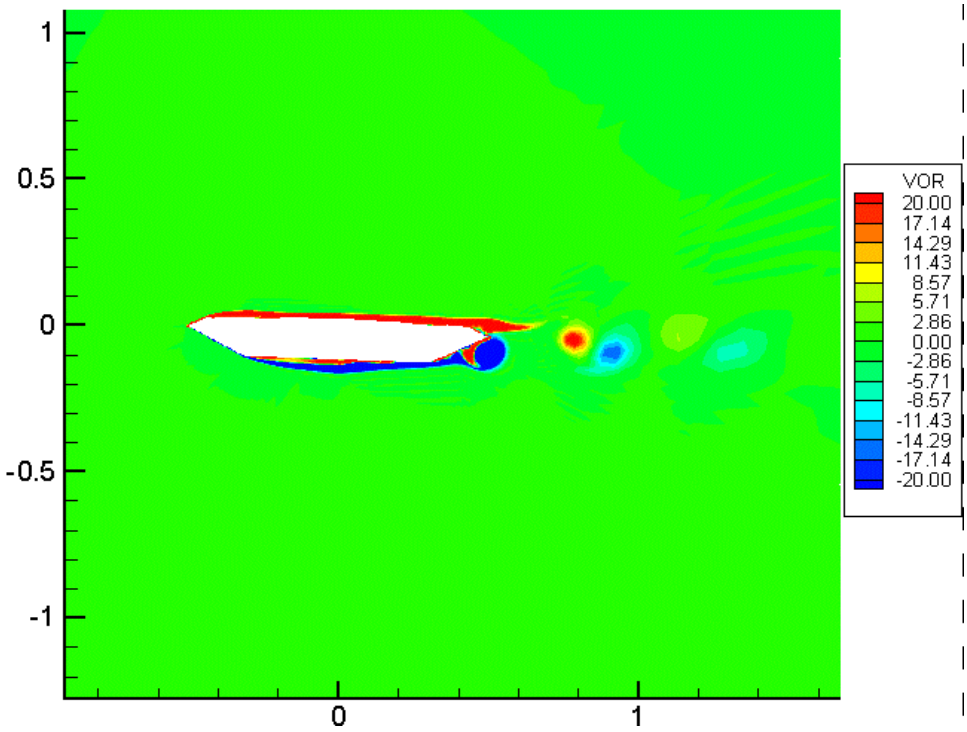

Figure 6.30 U =1.2 (Moving case)

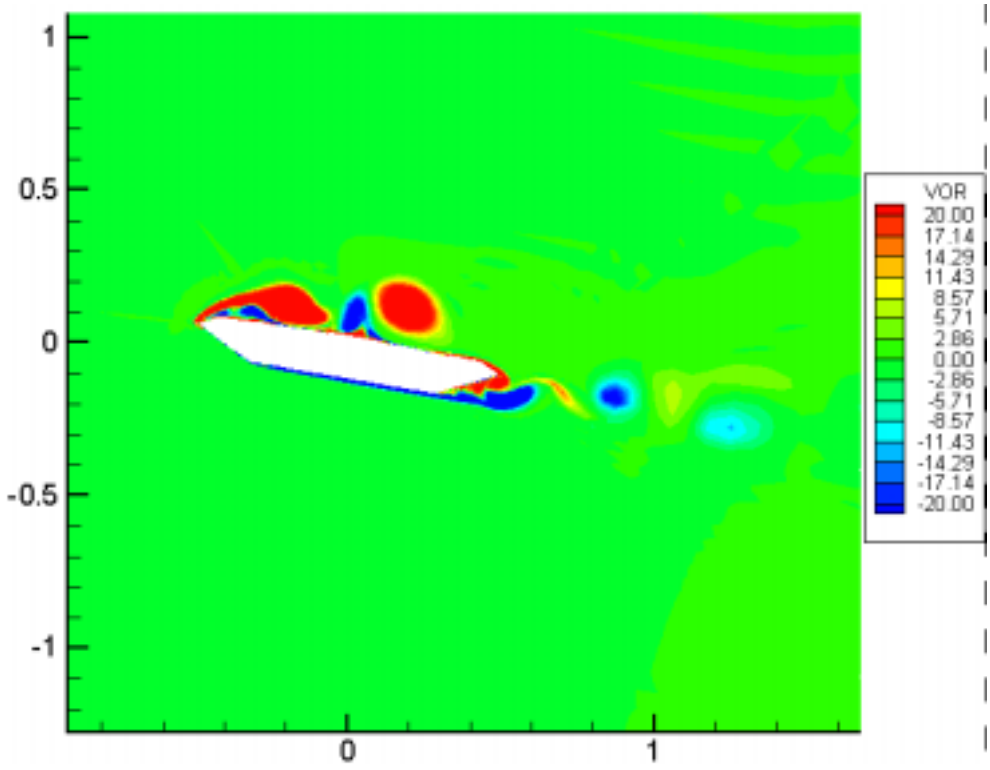

Figure 6.31 U =1.25 (Moving case)

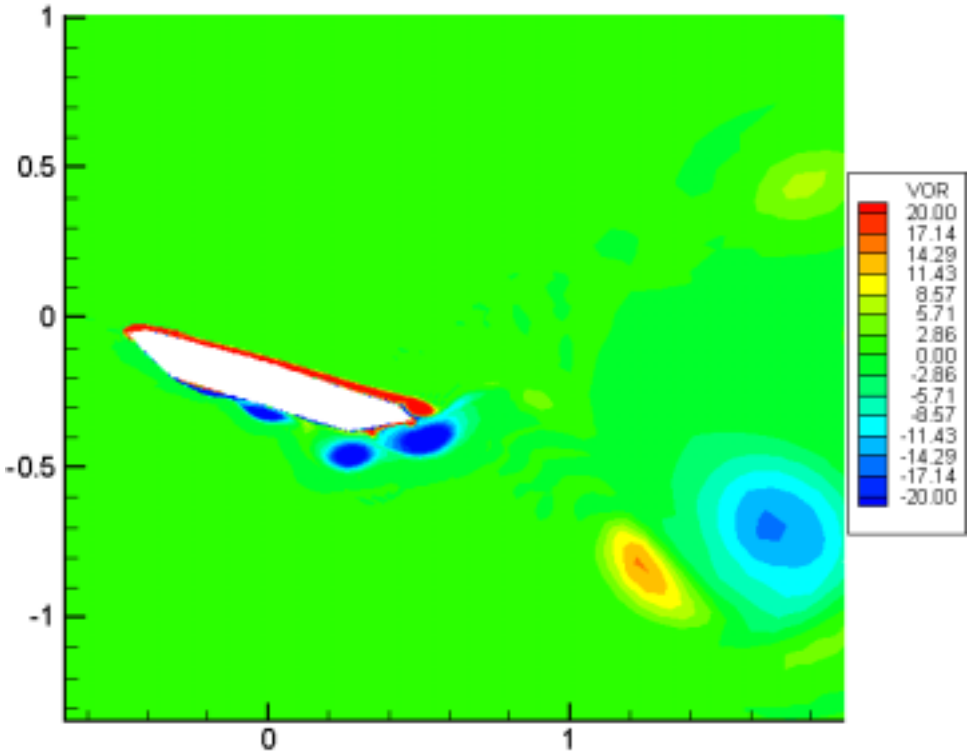

Figure 6.32 U =1.3 (Moving case)

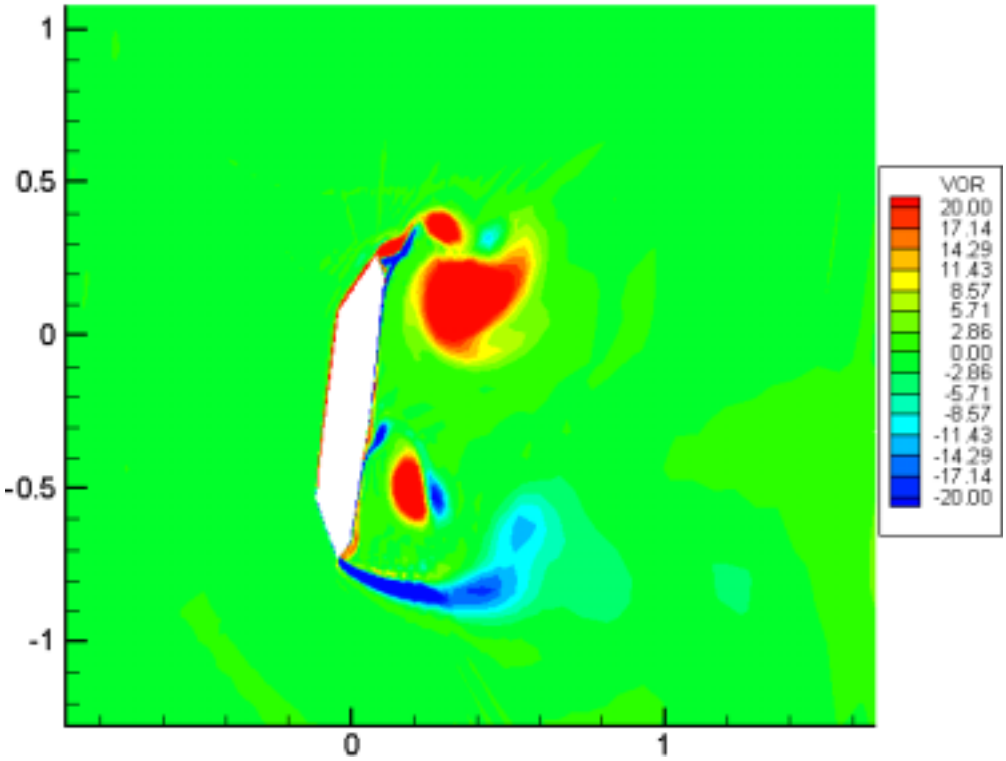

Figure 6.33 U =1.4 (Moving case)

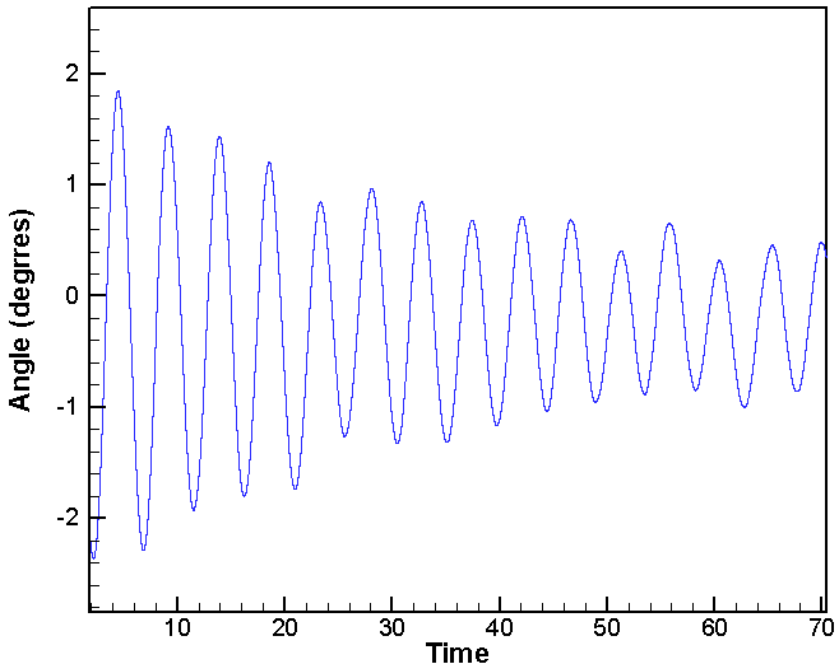

Figure 6.34 Condition for No Flutter: $\theta = 0.3$, $U = 0.7$

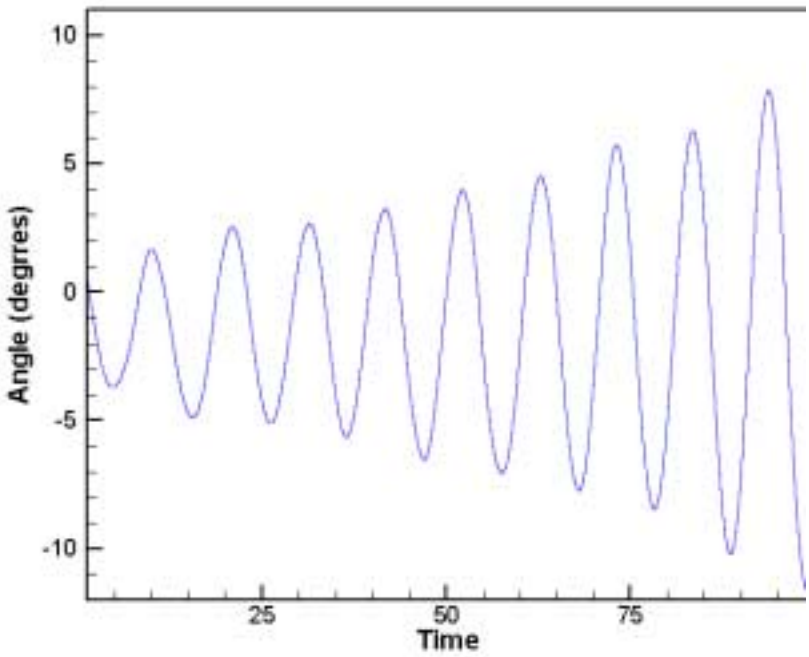

Figure 6.35 Condition for flutter: $\theta = 0.3$, $U = 1.25$

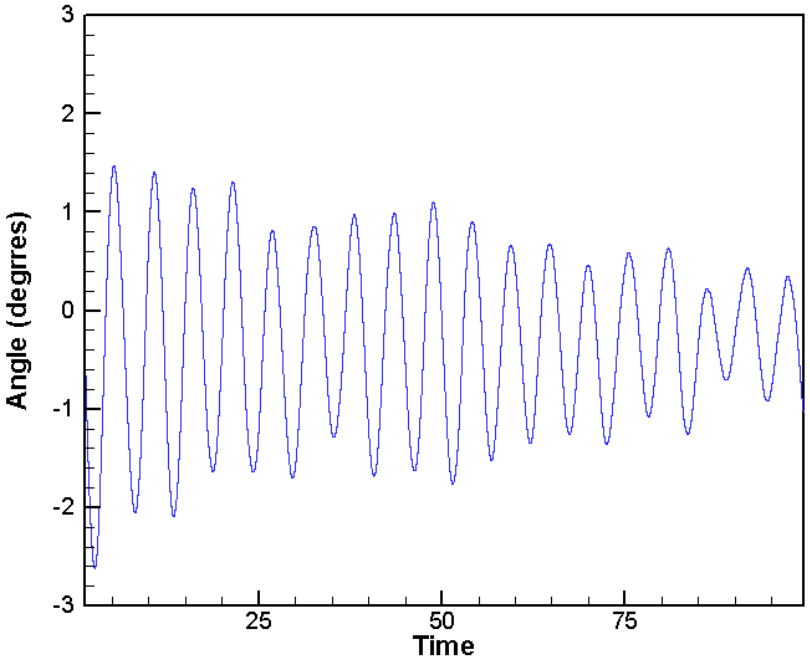

Figure 6.36 Condition for No Flutter: $\theta = 0.1,\ U = 0.8$

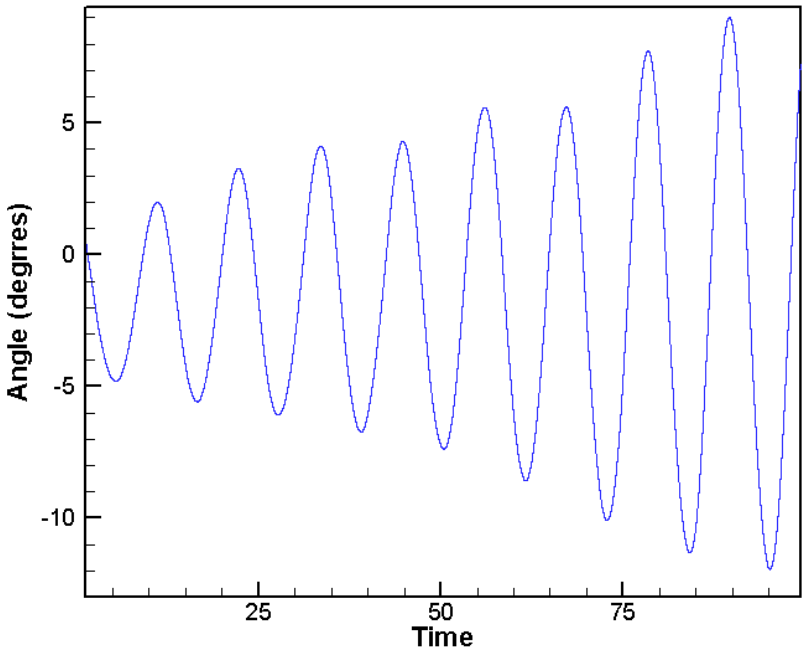

Figure 6.37 Condition for flutter: $\theta = 0.1,\ U = 1.3$

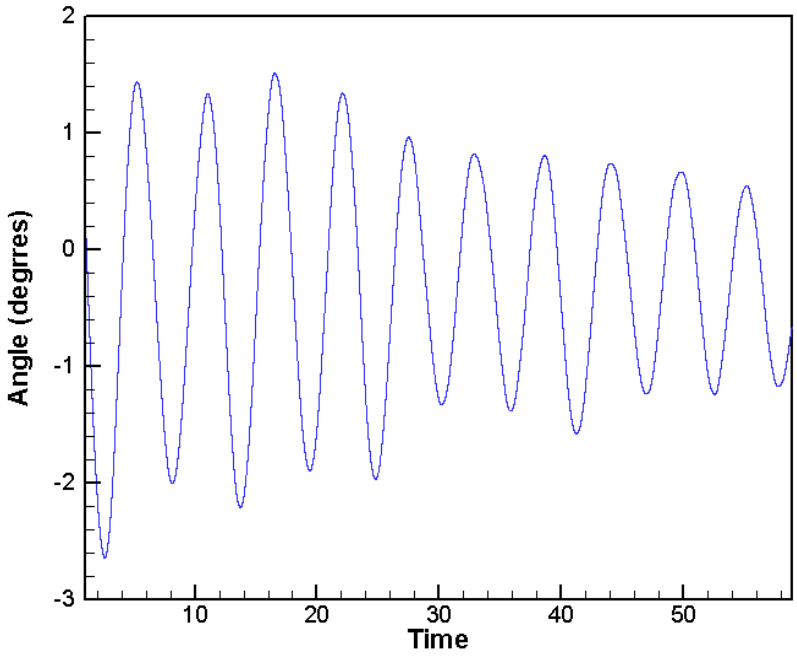

Figure 6.38 Condition for No Flutter: $\theta = dt$, $U = 0.8$

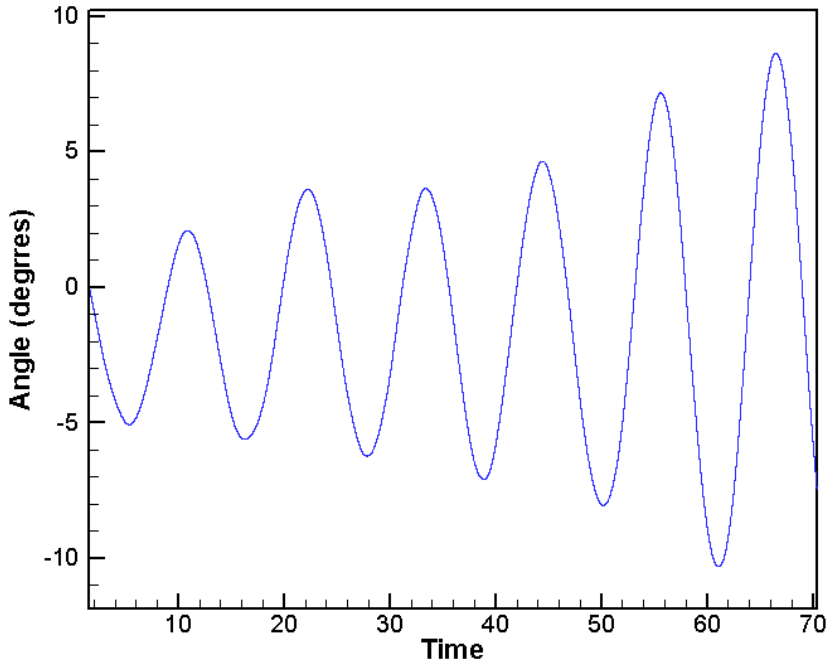

Figure 6.39 Condition for flutter: $\theta = dt$, $U = 1.3$

6.4 Comparison of results

The results of the work done by other researchers for the same GBEB suspension span are summarized here. The critical flutter velocity predicted in this model is in good agreement with the wind tunnel results. Frandsen et. al. reported that at this time, they were not able to predict the flutter velocity accurately and their model needs improvement.

Model by	**U (m/s)**
This work	65-72
Larsen et. al.(1997)	74
Enevoldsen et. al.(1999)	70-80
Frandsen et. al.(1998)	50
Wind Tunnel Tests	73

Table 6.3 Summary of results for moving bridge computations for GBEB suspension span.

CHAPTER 7

CONCLUSIONS

7.1 Summary

Computational work done by various researchers and the type of numerical methods used by them are reviewed. The FEM, FDM and the DVM methods are reviewed and analyzed and their advantages and disadvantages are discussed. The different turbulence models in use are surveyed.

The wind flow around the GBEB bridge is simulated and successfully modeled for both the fixed and moving conditions. In the fixed case, the bridge is held fixed during the computations over time. In the moving case, the bridge is allowed to oscillate about the shear center in accordance with the fluid structure interaction. The Finite Element model was used and the turbulence was modeled using the Large Eddy Simulation (LES) technique. The flow is solved using the Navier-Stokes equations for an incompressible flow. The Euler-backward difference time integration scheme was used to solve the Navier-Stokes equations. The moving case of the bridge was solved using a central difference time integration method. The rigid body grid movement technique was used for updating the grid for each time step during motion of the bridge under wind.

7.2 Conclusions

The model was able to predict the shedding of vortices above and below the deck surfaces and in the wake region as well, during the flow separation caused by the bridge. The LES/FEM model was able to capture the vortex shedding reasonably well. The

Strouhal number is in good agreement with wind tunnel measurements and other numerical modeling results. The drag coefficient is bit lesser than that predicted by wind tunnel tests. All the computations are carried out for a Reynolds number of 1×10^5. In the moving case, the critical velocity for the onset of flutter was predicted successfully and is in good agreement with the wind tunnel results and work done by others. The obtained critical flutter velocity of 65-72 m/s agrees well with 73 m/s from the wind tunnel measurements. The time step size to be input in the moving grid program was of concern in light of the stability of the computational runs. The time step for moving grid was chosen to be smaller than the one calculated for the same case on a fixed grid.

7.3 Recommendations for future work

In this work semi-implicit procedure was used which is based upon the time step, lower than the CFL number one. Better procedure to solve the Fluid structure interaction (FSI) problem can be investigated. If implicit procedures are used then one can use larger time step (Selvam et. al., 1998). The usage of larger time step saves a lot of computational time.

At this time the running of the moving grid model with 14805 grid points for about 100 seconds takes 4 days of Sun Microsystems Enterprise 4500 computer, with 8-400MHz/4Mb external cache CPU modules and 4Gb-memory expansion. To reduce the computing time and improve the performance parallel-computing techniques can be used. Then one can solve the same problem in a matter of few hours.

Incorporation of the GBEB cross-section with the railings in the computer model is also a possible scope for future work.

REFERENCES

Anderson, J.D., 1995, "**Computational Fluid Dynamics: The basics with applications"**, McGraw Hill, New York

Arrol, W. C., and Chatterjee, S., 1981, "Implications of the rules on bridge design-past and future", **Proceedings of conference at Institution of Civil Engineers,** London, March 25-26

Barker, R. M., and Puckett, J. A., 1997, "**Design of Highway bridges"**, John Wiley and Sons, New York

Bowers, N. A., 1940, "Tacoma Narrows bridge wrecked by wind", **Engineering News Record,** Vol. 125, pp. 647

Bruno, L., Khris S., and Marcillat, J., 2000, "Numerical Simulation of the effect of section details on the vortex-shedding flow past a long-span bridge deck", **Proceedings of the 3rd International symposium on Computational Wind Engineering**, Birmingham, UK, September 4-7.

Choi, T.J., 1997, "**Generating Optimal Computational Grids: Overview and Review"**, Dept of Mechanical Engineering, Carnegie Mellon University.

De Sampaio, P.A.B., Lyra, P.R.M., Morgan, K. and Weatherill, N.P., 1993, "Petrov-Galerkin solutions of the incompressible Navier-Stokes equations in primitive variables with adaptive remeshing", **Computer Methods in Applied Mechanics and Engineering**, Vol. 106, pp.143-178.

Dowell, E. H., Curtiss, H. C., Scanlan, R. H. and F.Sisto, R. H., 1978, "**A modern course in aeroelasticity",** Sijith & Noordhoff, Netherlands.

Dowell, E. H., 1975, "**Aeroelasticity of plates and shells"**, Noordhoff International publishing, Netherlands.

Dyrbye, C. and Hansen, S.O., 1996, "**Wind loads on Structures"**, John Wiley & Sons

Enevoldsen, I., Hansen, S.O., Kvamsdal, T., Pedersen, C., Thorbek, L.t., 1999, "Computational wind simulations for cable-supported bridges", in Larsen, A., Larose, G.L. and Livesey, F.M. (eds), **Wind Engineering into the 21st Century**, A.A. Balkema, Rotterdam, Vol. 2, 1265-1270.

Ferziger, J.L., and Peric, M., 1999, "**Computational methods for fluid dynamics"**, Springer, Berlin

Frandsen, J.B. and McRobie, F.A., 1998, "Comparison of numerical and physical models for bridge deck aeroelasticity", **IABSE symposium**, Kobe, Japan.

Frandsen, J.B. and McRobie, F.A., 1999, "Computational aeroelastic modeling to guide long-span bridge cross-section design", in Larsen, A., Larose, G.L. and Livesey, F.M. (eds), **Wind Engineering into the 21st Century,** A.A. Balkema, Rotterdam, Vol. 2, 1277-1284.

Hansen, S.O., Enevoldsen, I., Pederson, C., and Thorbek, L.T., 1999, "Practical design perspectives in FSI-Simulations of wind load on large bridges", **Proceedings of the International Symposium on Computational Method for Fluid-Structure Interaction,** Feb. 15-17, Trondheim, Norway, pp.239-260.

Hughes, T. J. R., and Jansen, J., 1993, "Finite Element Methods in Wind Engineering", **Journal of Wind Engineering and Industrial Aerodynamics,** Vol. 46&47, pp.297-313.

Larsen, A., 1995, "Predictions of aeroelastic stability of suspension during erection", **Proceedings of the 9th International Conference on Wind Engineering,** India.

Larsen, A., and Walther, J. H., 1996, "A new Computational Method for assessment of the Aeroelastic stability of long span bridges", **IABSE**, Copenhagen.

Larsen, A., and Walther, J. H., 1996a, "Aeroelastic analysis of bridge girder sections based on Discrete Vortex Simulations", **Journal of Wind Engineering and Industrial Aerodynamics,** Vol. 67 & 68, pp. 235-265.

Liu, 1991, "**Wind Engineering: A Handbook for structural Engineers"**, Prentice Hall, New Jersey.

Mendes, P.A. and Branco, F.A. 1995, "Evaluation by CFD of the flutter derivatives for a rectangular section", in **Wind Engineering Retrospect and Prospect,** 9th ICWE, Wiley Eastern Ltd., New Delhi, India, Vol. II, pp.562-571.

Murakami, S. and Mochida, A., 1995, "On turbulent vortex shedding flow past 2D square cylinder predicted by CFD", **Journal of Wind Engineering and Industrial Aerodynamics**, Vol. 54/55, pp.191-211.

Nomura, T. and Hughes, T.J.R., 1992, "An arbitrary Lagrangian-Eulerian finite element method for interaction of fluid and a rigid body", **Computational Methods and Applied Mechanics. & Engineering,** Vol.95, pp.115-138.

Peraire, J., Morgan, K., and Peiro, J., "**Unstructured Mesh Methods for CFD",** I.C. report 90-04 June 1990, Dept of Aeronautics, Material College of Science and Technology and Medicine, London.

Sachs, P., 1978, "**Wind Forces in Engineering",** Second edition, Pergamon Press, Oxford.

Selvam, R. P., 1990, Computer Simulation of Wind Load on a House, **Journal of wind Engineering and Industrial Aerodynamics**, Vol. 36, pp. 1029-1036.

Selvam, R. P., 1992a, "Turbulent Flow Simulation", Chapter 3 of **The State of the Art Report on Computational Wind Engineering,** prepared for ASCE task committee on CFD in Wind Engineering, Also available from: Bell 4190, University of Arkansas, Fayetteville, AR 72701.

Selvam, R.P., 1994, A Report on "Implementation of preconditioned conjugate gradient solution procedure for large structural or finite element problems". Available from: Bell 4190, University of Arkansas, Fayetteville, AR 72701.

Selvam, R. P., 1995, "Numerical Methodologies and Turbulent Flow Simulation in Computational Wind Engineering", **Restructuring: America and Beyond,** Vol. 2, pp. 1269-1272.

Selvam, R. P., 1997, Computation of Pressures on Texas Tech. Building Using Large Eddy Simulation, **J. Wind Engineering and Industrial Aerodynamics**, Vol. 67&68, pp. 647-657.

Selvam, R.P., 1998, "Computational Procedures in Grid Based Computational Bridge Aerodynamics", in Larsen, A., and Esdahl, S. (eds), **Bridge Aerodynamics,** A.A Balkema, Rotterdam, pp. 327-336.

Selvam, R. P., Tarini, M. J., Larsen, A., 1998, "Computer modeling of flow around bridges using LES and FEM", **Journal of Wind Engineering and Industrial Aerodynamics,** 77-78.

Selvam, R. P., Bosch, H., 1999, "Finite Element modeling of flow around bridges", in A. Larsen, A., Larose, G.L. and Livesey, F.M. (eds), **Wind Engineering into the 21st Century,** A.A Balkema, Rotterdam, Vol. 2, pp. 1321-1327.

Selvam, R. P., Visbal, M.R., and Morton, S.A., 1998, "Computation of nonlinear viscous panel flutter using a fully implicit aeroelastic solver", **AIAA-98-1844.**

Selvam, R. P., and Govindaswamy, S., 2000, "Aeroelastic analysis of bridges using FEM and Moving grids", **Proceedings of the 3rd International Symposium on Computational Wind Engineering**, Birmingham, UK, September 4-7.

Simiu, E., and Scanlan, R.H., 1996, "**Wind effects on Structures",** Third edition, Wiley Interscience, New York

Smith, D., 1974, "**A Case Study and Analysis of the Tacoma Narrows Bridge Failure"**, 99.497 Engineering Project, Department of Mechanical Engineering, Carleton University, Ottawa, Canada, March 29.

Tamura, T., Itoh, Y., Wada, A. and Kuwahara, K. 1995, "Numerical study of pressure fluctuations on a rectangular cylinder in aerodynamic oscillation", **Journal of Wind Engineering and Industrial Aerodynamics,** Vol. 54/55**,** pp.239-250.

Tarini, M. J., 1997, "Computer modeling of wind flow around a 3D circular cylinder and a bridge using LES and FEM", **Masters Thesis, University of Arkansas,** Fayetteville, Arkansas, August.

Thomas, P.D., Lombard, C.K. (1979), "Geometric conservation law and its application to flow computations on moving grids", **AIAA**, 17, 1030-1037.

Walther, J. H., 1994, "Discrete vortex method for 2D flow past bodies of arbitrary shape undergoing prescribed rotary and translational motion", **Ph.D. Thesis**, **Department of fluid mechanics, Technical University of Denmark**, Denmark.

Von Karman, T., "Aerodynamic stability of suspension bridges", **Engineering News Record,** Vol.125, Page-670.

Zienkiewicz, O.C., 1979, "**The Finite element method"**, third edition, Tata McGraw hill Publishing, New Delhi.

APPENDIX

Configuration of the GBEB section.

Co-ordinate file of the GBEB- approach span with the domain definition

0.71774	3.7702e-2	3.0	2.0
0.93548	3.2258e-2	3.0	1.0
1.0	0.0	3.0	0.5
0.80645	-9.6774e-2	3.0	-1.0
0.60215	-9.6774e-2	3.0	-2.2
0.39785	-9.6774e-2	-2.0	-2.2
0.19355	-9.6774e-2	-2.0	-1.0
0.0	0.0	-2.0	0.5
6.4516e-2	3.2258e-2	-2.0	1.0
0.28226	3.7702e-2	-2.0	2.0
0.5	4.3145e-2	0.5	2.0
0.71774	3.7702e-2	3.0	2.0

Co-ordinate file of the GBEB –suspension with the domain definition

0.75	3.876e-2	3.0	2.0
0.9864	3.876e-2	3.0	1.0
1.0	0.0	3.0	0.2
0.7132	-0.2209	3.0	-1.2
0.6	-0.2209	3.0	-2.2
0.4	-0.2209	-2.0	-2.2
0.2868	-0.2209	-2.0	-1.2
0.0	0.0	-2.0	0.2
1.357e-2	3.876e-2	-2.0	1.0
0.2	3.876e-2	-2.0	2.0
0.5	5.039e-2	0.5	2.0
0.75	3.876e-2	3.0	2.0

Here, the first two columns in this data files represents the x and y co-ordinate of the points that define the cross-section and located along the perimeter of the bridge. The third and fourth columns represents the x and y co-ordinates of the points that define the domain